



TECHNISCHE
UNIVERSITÄT
WIEN
Vienna University of Technology

DIPLOMARBEIT

Measurement of J/ψ Polarization with the CMS Experiment in Proton-Proton Collisions at $\sqrt{s} = 7$ TeV

AUSGEFÜHRT AM

Institut für Hochenergiephysik (HEPHY)
der Österreichischen Akademie der Wissenschaften (ÖAW)

UNTER DER ANLEITUNG VON

Univ. Prof. DI Dr. Christian Fabjan und Dr. Josef Strauss

DURCH

Valentin Knünz
Kürnberggasse 1/5, 1150 Wien

Contents

1	Introduction	1
1.1	Introduction and Motivation	1
1.2	Outline	2
2	The LHC: Machine and Physics	3
2.1	The Machine	3
2.2	Physics at the LHC	6
2.2.1	Search for the Higgs Boson	6
2.2.2	Search for Supersymmetric Particles	8
2.2.3	Search for New Massive Vector Bosons	8
2.2.4	Search for Extra Dimensions	9
2.2.5	Standard Model Physics	9
2.2.6	Heavy-Ion Physics	9
3	The CMS Detector	11
3.1	Experimental Challenges	11
3.2	Coordinate Conventions	12
3.3	Detector Overview	12
3.4	Detector Components	13
3.4.1	Superconducting Solenoid	13
3.4.2	Muon System	15
3.4.3	Inner Tracking System	16
3.5	The CMS Trigger System	18
3.5.1	Level 1 Trigger	19
3.5.2	High Level Trigger	20
3.5.3	Collected Data and Luminosity	20

4	Quarkonium Physics	23
4.1	Introduction to Quarkonium Physics	23
4.2	The Quarkonium Spectrum	26
4.3	Quarkonium as Probe in QCD	28
4.4	Quarkonium Production	28
4.4.1	A Short Introduction to QCD	29
4.4.2	The Non-Relativistic QCD Factorization Approach	31
4.4.3	Color Octet Model	32
4.4.4	Color Singlet Model	33
4.4.5	Color Evaporation Model	34
4.4.6	Model Predictions and Experimental Results	35
4.5	Quarkonium Production - Summary and Outlook	38
5	Quarkonium Polarization	41
5.1	General Concepts	41
5.2	The Polarization Reference Frame	42
5.2.1	Definition of the Reference Frame	42
5.2.2	Conventions	44
5.3	Dilepton Decay Angular Distribution	45
5.4	Measurement Dependence on the Reference Frame	48
5.4.1	Transformation of Polarization Parameters into Different Frames	48
5.4.2	Kinematic Dependence of the Polarization Parameters	49
5.4.3	Positivity Constraints	50
5.5	A Frame-Invariant Approach	51
5.6	Influence of Feed-Down Contributions	53
5.7	Summary	54
6	Experimental Situation of J/ψ Polarization	57
6.1	Survey of Existing J/ψ Polarization Measurements	57
6.1.1	Fixed Target Experiments	57
6.1.2	Collider Experiments	58
6.2	J/ψ Polarization Scenarios from the Tevatron to the LHC	61
6.2.1	Possible Interpretations of Tevatron Results	62
6.2.2	Predictions for J/ψ Polarization at LHCb	65
6.2.3	Predictions for J/ψ Polarization at CMS	65
6.3	Summary	68

7	J/ψ Polarization Analysis	71
7.1	Analysis Strategy	72
7.2	The Data Sample	73
7.2.1	Muon Reconstruction in CMS	73
7.2.2	The High Level Trigger	74
7.2.3	Data Processing	76
7.2.4	Monte Carlo Samples	76
7.2.5	Geometrical Acceptance and Fiducial Cuts	77
7.2.6	Event Yields	80
7.3	Efficiency Determination with MC Simulation	80
7.4	Fitting Technique and Minimization	83
7.4.1	The Likelihood Method	83
7.4.2	Minimization Algorithms	85
7.5	The Fitting Procedure	86
7.5.1	Dimuon Mass Model	87
7.5.2	Decay Length Model	89
7.5.3	Decay Angular Distribution Model	92
7.5.4	The Two-Step Fitting Procedure	93
7.6	Summary of the Baseline Analysis Strategy	98
8	Validation of the Framework	99
8.1	Tests with Simplified Monte Carlo Simulations	99
8.1.1	The Toy-MC Method	99
8.1.2	Application to Polarization Analysis	100
8.1.3	Results of the Toy-MC Tests	102
8.2	Monte Carlo Consistency Test	104
8.3	Evaluation of Systematic Effects	108
8.4	Summary	111
9	The Optimized Approach	113
9.1	Overview and Motivation	113
9.2	Data Driven Efficiency Determination	114
9.2.1	The <i>Tag and Probe</i> Method	115
9.2.2	The ρ -Factor	116
9.3	Fiducial Cuts	117
9.4	The Likelihood of the Optimized Method	118
9.5	Summary of the Optimized Analysis Strategy	120

10 Conclusions	121
10.1 Summary	121
10.2 Outlook	122
A Acknowledgements	125
B Abstract	127
C Summary of Author's Contributions	129
D Curriculum Vitae	133
E List of Abbreviations	135
F List of Figures	139
G List of Tables	145
H Bibliography	147

Chapter 1

Introduction

1.1 Introduction and Motivation

Quarkonium physics has been an active field of fundamental research in high energy physics since 1974, after the discovery of the J/ψ meson and the first experimental evidence of the existence of the charm quark. Quarkonia are bound states of a heavy quark and its respective antiquark ($c\bar{c}$, $b\bar{b}$). Various experiments and theorists have gathered information to gain more understanding of the spectral distribution, production and decay mechanisms of the quarkonium meson family.

Several theoretical models have been developed to understand the mechanisms of quarkonium production. However, differential cross section measurements of quarkonia and various spin alignment (polarization) measurements of quarkonia cannot be reproduced by these model calculations simultaneously. Furthermore, contradictory experimental polarization measurements have led to additional confusion in this field.

The *Large Hadron Collider* (LHC), located at CERN, the European Organization for Nuclear Research, provides very good conditions to study quarkonium production. The LHC has provided data for physics since early 2010, producing collisions of two proton beams at a center of mass energy of 7 TeV. The *Compact Muon Solenoid* (CMS) detector, collecting data at one of the collision points of the LHC, is very well suited to study various properties of the quarkonia that are produced. Data analysis at the LHC experiments is hoped to contribute in a significant way to the understanding of underlying quarkonium production mechanisms.

1.2 Outline

This thesis reports the analysis strategy of the first measurement of J/ψ polarization at $\sqrt{s} = 7$ TeV, based on data collected by CMS.

This document will first give a short description of the LHC accelerator chain, followed by a brief overview of some of the physics topics that will be covered at the LHC experiments (Chap. 2). The requirements for and the design of the CMS detector will be explained in Chap. 3, with emphasis on the subdetector systems relevant for the analysis reported in this thesis. An introduction to quarkonium physics will be given, and several quarkonium production models will be discussed in Chap. 4, also covering an overview of current experimental knowledge of quarkonium differential cross sections. Chapter 5 will give an introduction to general concepts of the polarization of vector quarkonia such as the J/ψ .

The experimental situation of J/ψ polarization will be discussed in Chap. 6, covering several possible interpretations of Tevatron results, leading to predictions for a J/ψ polarization measurement at CMS, providing tools with discriminating power. The baseline analysis strategy for the extraction of the J/ψ polarization at CMS will be discussed in more detail in Chap. 7. Methods of validation of this framework as well as the evaluation of systematic effects are discussed in Chap. 8, and further developments of the analysis framework are summarized in Chap. 9.

After a summary of the main aspects of this thesis, an outlook at future measurements at CMS, necessary to further clarify the understanding of quarkonium production, will be given (Chap. 10).

The author significantly contributed to the analysis by the evaluation of possible interpretations of the CDF J/ψ polarization measurement, the development and construction of the analysis strategy, the separation of prompt and non-prompt J/ψ contributions, by various cross checks and the evaluation of systematic effects. A detailed summary of the author's contributions will be given in Appendix C.

Chapter 2

The LHC: Machine and Physics

2.1 The Machine

The Large Hadron Collider is a superconducting two-ring synchrotron accelerator and collider that brings two proton beams to collision at a nominal center of mass energy of 14 TeV. It currently operates at $\sqrt{s} = 7$ TeV, which is planned to be increased to the design value after a long shutdown period in 2013. It further accelerates and collides heavy-ion beams (lead-lead) with a design center of mass energy of 2.76 TeV/nucleon [1].

As one challenge was to minimize the costs of the project, the LHC was designed for the existing Large Electron Positron Collider (LEP) tunnel, which was built from 1984 to 1989. The tunnel has a circumference of 27 km and is in between 45 m and 170 m below ground under both swiss and french territories, located near Geneva [1].

The protons are pre-accelerated by the already existing accelerator complex at CERN (Fig. 2.1). The LINAC2, a linear accelerator, accelerates proton bunches to 50 MeV, the following Proton Synchrotron Booster (PSB) to 1.4 GeV, and the Proton Synchrotron (PS) to 25 GeV. The Super Proton Synchrotron (SPS), accelerating protons to 450 GeV, is the last step before injection into the LHC. The total injection time for the LHC is approximately 4 minutes [1].

The beam is accelerated by a 400 MHz superconducting cavity system. A total of 1232 superconducting dipole magnets along the ring keep the particle beams on their circular path, and 392 quadrupole magnets ensure the focusing of the beams. The dipole magnets are cooled to 2 K with superfluid helium and can operate at fields up to above 8 T. As the existing 3.8 m diameter LEP tunnel does not allow to have two separate beam-pipes because of space limitations, a *two-in-one* design has been adapted for most of the LHC magnets.

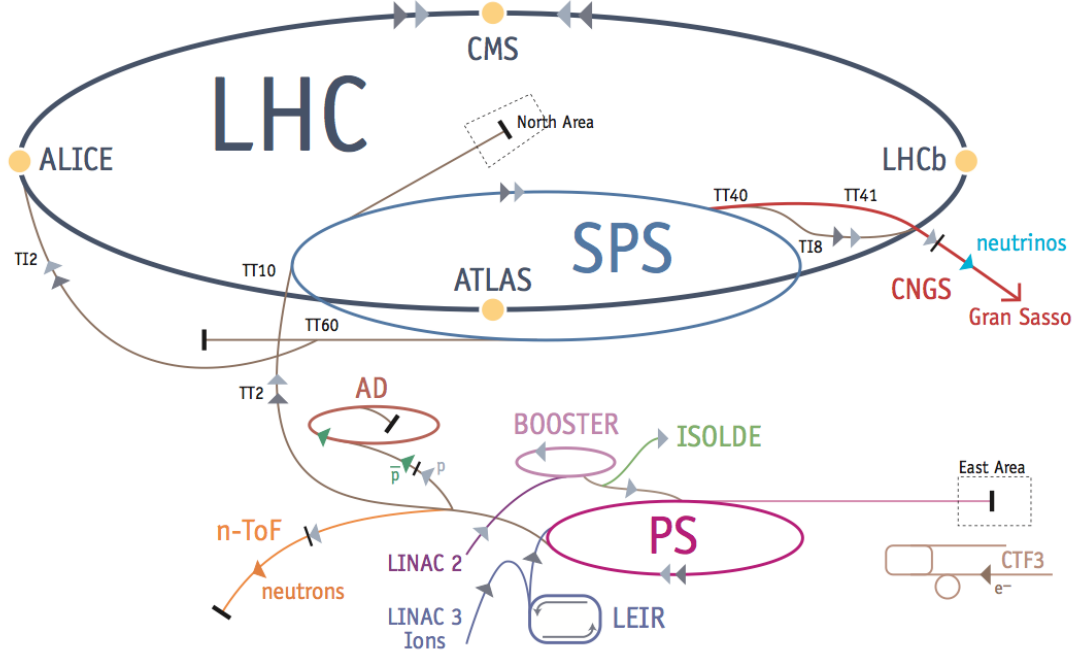


Figure 2.1: The CERN accelerator complex [2].

The LHC is designed to contain 2808 bunches of approximately 10^{11} protons/bunch. The nominal LHC design allows a minimal separation of the individual bunches of 25 ns, currently the LHC operates with 75 ns spacing. In order to fulfill these requirements, the PS has been equipped with bunch splitting schemes. These considerations correspond to the LHC nominal design value of the *instantaneous luminosity* of $10^{34} \text{ cm}^{-2}\text{s}^{-1}$, which is given by

$$L = \frac{N_b^2 n_b f_{rev} \gamma_r}{4\pi \epsilon_n \beta^*} F \quad (2.1)$$

for gaussian beam distributions, with N_b the number of particles per bunch, n_b the number of bunches per beam, f_{rev} the revolution frequency, γ_r the relativistic gamma factor, ϵ_n the normalized transverse beam emittance, β^* the betatron function at the collision point, and F the geometric luminosity reduction factor due to the crossing angle. The number of particles produced in a certain process per second is then given by

$$N_{process} = L \cdot \sigma_{process}, \quad (2.2)$$

with $\sigma_{process}$ the production cross section for the process under study [1]. As the

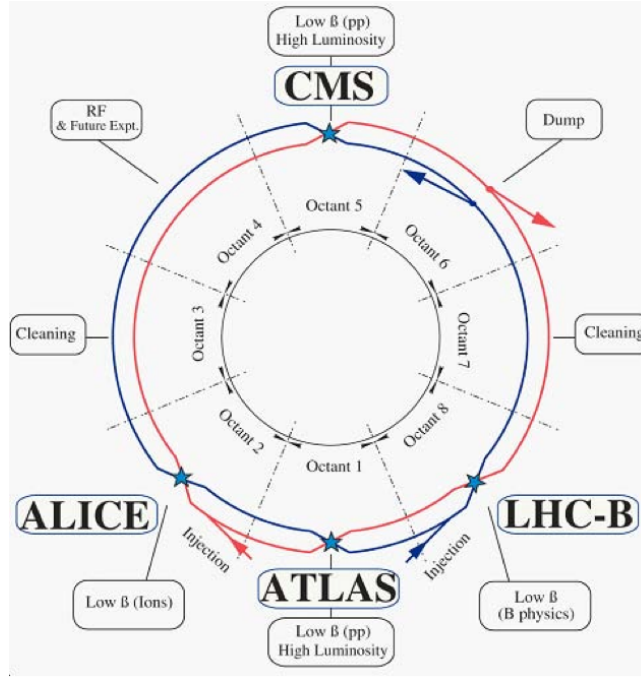


Figure 2.2: Schematic layout of the LHC [1].

luminosity can change over time, the value of the luminosity, integrated over time t ,

$$\hat{L}(\Delta t) = \int_{t_1}^{t_2} L(t) dt, \quad (2.3)$$

is a suitable parameter characterizing the amount of data collected by the LHC experiments in the time period $\Delta t = t_2 - t_1$. In high energy physics, *events per picobarn*, or simply *inverse picobarn* (pb^{-1}) is a very common unit used to quantify $\hat{L}(\Delta t)$. The total proton-proton cross section at LHC is ~ 100 mb. Hence, at instantaneous design luminosity, 1 pb^{-1} corresponds to $\sim 10^{11}$ proton-proton interactions.

The LHC has two high luminosity experiments, ATLAS (*A Toroidal LHC Apparatus*) and CMS (*Compact Muon Solenoid*), both aiming at a peak luminosity of $L = 10^{34} \text{ cm}^{-2}\text{s}^{-1}$ for proton operation. The LHCb (*LHC beauty*) experiment, designed for studying B-physics, is a low luminosity experiment aiming at a peak luminosity of $L = 10^{32} \text{ cm}^{-2}\text{s}^{-1}$. However, recent considerations have shown that LHCb can operate with higher luminosities than the nominal design value. The LHC has one dedicated ion experiment, ALICE (*A Large Ion Collider Experiment*), aiming at a peak luminosity of $L = 10^{27} \text{ cm}^{-2}\text{s}^{-1}$ for nominal lead-lead ion operation. Figure 2.2 shows a schematic layout of the 4 main collision points of LHC, and the respective detectors [1].

Beam Commissioning started in March 2010. The number of bunches was steadily increased during 2010 and 2011 which resulted in a new luminosity record with a luminosity peak of $L = 3.16 \cdot 10^{33} \text{ cm}^{-2}\text{s}^{-1}$, as of September 22nd 2011.

2.2 Physics at the LHC

This section is based on Chap. 1.3 in Ref. [3] and on Ref. [4]. It provides an overview of the physics program of the LHC experiments.

The main motivation of the LHC is to clarify the nature of electroweak symmetry breaking, for which the Higgs mechanism is presumed to be responsible. However, there are alternatives that require higher symmetries, such as supersymmetric models, but unknown mechanisms are also possible. Furthermore, the LHC physics community has strong hopes that there will be discoveries that ease the way towards a unified theory. Candidates of such discoveries are for example supersymmetric particles and extra dimensions, which would require modification of the gravity at the TeV scale. LHC parameters, such as the center of mass energy and the instantaneous luminosity have been carefully chosen to provide the most suitable conditions for the individual detectors to explore the physics topics that are now discussed in more detail.

At this point it should be mentioned that this thesis uses the convention of natural units, $c = \hbar = 1$. Hence, energy, mass and momentum quantities are given in units of eV.

2.2.1 Search for the Higgs Boson

The Higgs boson is the only particle needed in the SM which has not been discovered by particle physics experiments so far. It is an integral part of the SM which allows the electroweak gauge bosons W and Z as well as the fermions to acquire mass due to spontaneous symmetry breaking through interaction with the Higgs field. In the SM, one weak isospin Higgs doublet is introduced and leads to the existence of one elementary Higgs particle after electroweak symmetry breaking. The Higgs couplings to the electroweak gauge bosons and all fermions are proportional to their masses. The only unknown parameter of the Higgs boson itself is the value of its mass m_H . Once this is known, all production and decay properties of the SM Higgs boson will be fixed. The search for the Higgs boson is a crucial endeavor for establishing the standard formulation of the electroweak theory [4].

The current lower limit on the mass of the Higgs boson obtained at LEP is 114.4 GeV [3]. Experiments at the Fermilab Tevatron have excluded the mass region 158-173 GeV [5]. Furthermore, recent CMS analyses [6] have shown that the SM Higgs

boson can be excluded in the mass ranges 145-216 GeV, 226-288 GeV and 310-400 GeV. These exclusions are at 95% confidence level.

Figure 2.3 shows dominant production mechanism diagrams at leading order and the production cross section of the various mechanisms, predicted for the LHC, in units of picobarn (pb). Figure 2.4 shows the decay modes relevant for the mass region that is accessible with LHC experiments (a) and the respective total decay width (b).

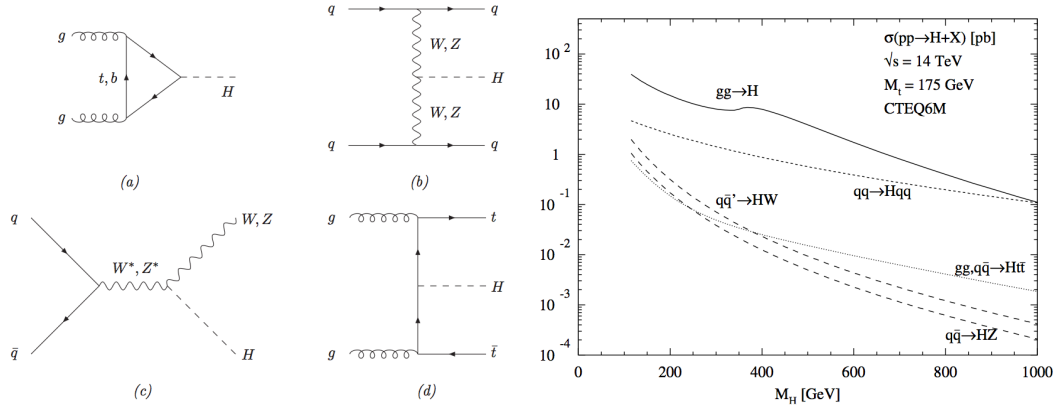


Figure 2.3: (left) Typical diagrams for the most relevant Higgs boson production mechanisms at leading order: (a) gluon fusion, (b) vector boson fusion, (c) Higgs-strahlung, (d) Higgs bremsstrahlung off top quarks. (right) Higgs production cross sections at the LHC for the various production mechanisms as a function of the Higgs mass [4].

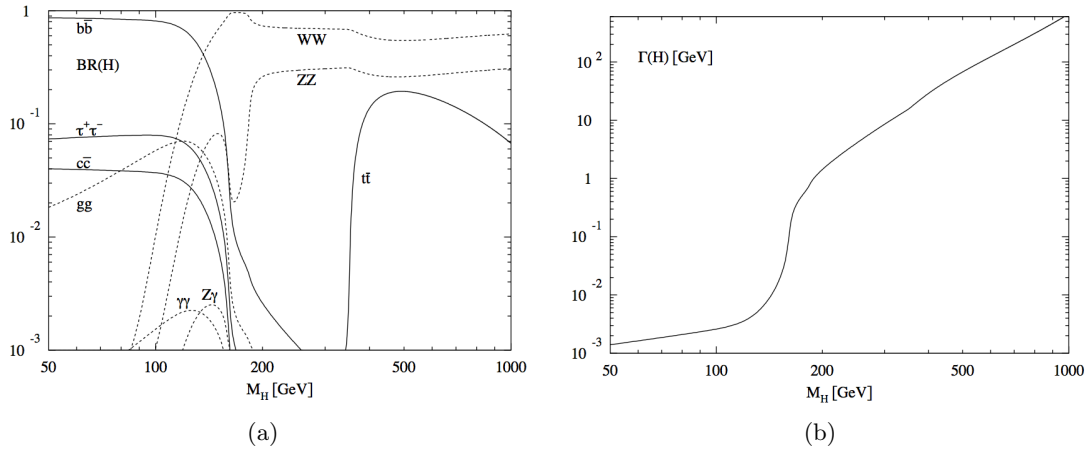


Figure 2.4: Branching ratios of the dominant decay modes of the SM Higgs particle (a) and total decay width (in GeV) of the SM Higgs boson as a function of its mass (b) [7].

In the mass region $m_H < 135$ GeV the main decay mode under study will be $H \rightarrow b\bar{b}$. In this mass region also $H \rightarrow \gamma\gamma$ can yield a significant signal. For higher Higgs masses, the $H \rightarrow ZZ \rightarrow 4\mu$ (*the golden channel*) is the dominant decay mode under study, which is the cleanest channel to study Higgs decays [3].

2.2.2 Search for Supersymmetric Particles

Supersymmetry (SUSY) is motivated by possible solutions to several problems of theoretical physics. For instance, SUSY allows unification of the experimentally measured strengths of the electroweak, electromagnetic and strong interactions at a very high energy scale, resulting in a unified interaction with only one coupling constant. Furthermore, if one assumes conservation of R parity, the lightest SUSY particle (LSP) is stable, and therefore a possible dark matter candidate.

SUSY postulates *superpartners* for all particles of the SM. While bosons have fermionic partners, all fermions of the SM correspond to bosonic superpartners.

One unpleasant feature of SUSY is the number of free parameters. The Minimal Supersymmetric Model (MSSM) alone, which contains the minimal extension of the SM particle content, introduces 105 free parameters due to the unknown mechanism for supersymmetry breaking. Therefore, several more constrained models have appeared in the literature, for instance the minimum super gravity model (mSUGRA), in which the number of parameters is reduced to 5 parameters [4].

The decays of supersymmetric particles, such as squarks and gluinos, involve cascades that, if R-parity is conserved, always contain the LSP. The latter is expected to interact very weakly, thus leading to large missing transverse energy E_T in the final state. This is a signature that all searches for R-parity conserving SUSY in the LHC experiments have in common. The rest of the cascade results in a number of scenarios with leptons and jets, which is studied in various analysis groups at CMS and ATLAS [3].

2.2.3 Search for New Massive Vector Bosons

Additional heavy neutral and charged gauge bosons (Z' , W') are predicted in many superstring-inspired and grand unified theories (GUT), as well as in dynamical symmetry breaking and *little Higgs* models. There are no theoretical predictions, however, of the Z' and W' mass scale [4]. Possible detectable decay channels would include e.g. $Z' \rightarrow e^+e^-$ or $Z' \rightarrow \mu^+\mu^-$. If discovered, measurements of the natural width and of the forward-backward asymmetry could possibly discriminate between the various models predicting additional heavy gauge bosons [3].

2.2.4 Search for Extra Dimensions

Extra-dimension models such as the Kaluza-Klein theory or ADD (Arkani-Hamed, Dimopoulos and Dvali) models assume n spatial compactified dimensions of macroscopic size [4]. The individual models differ by the size and the geometry of the extra dimensions, and the definition of the particles that are allowed to propagate in the additional dimensions.

The existence of extra dimensions can lead to a characteristic energy scale of quantum gravity, M_D , which is the analogue of the Planck mass ($M_{Planck} \sim 10^{19}$ GeV) in a D -dimensional theory, and which could lie just beyond the electroweak scale [3]. These assumptions would create the spectacular possibility of creating mini black holes at the LHC, if the collision energy exceeds M_D . Production of black holes at the LHC would result in decay chains containing leptons, photons, neutrinos, W, Z, and jets. Determination of the Hawking temperature, mass of the black holes and even the number of extra dimensions would be possible [3].

2.2.5 Standard Model Physics

Besides *Beyond the SM* (BSM) physics searches, the LHC experiments will conduct various precision measurements of SM parameters in an unprecedented energy regime. Extensive tests of QCD, electroweak and flavor physics will be done. Due to the possibility of measuring transverse energies of jets and photons up to the TeV scale, cross sections will be measured in a p_T range where they fall by more than 10 orders of magnitude. Top quarks will be produced at rates never measured before [3].

In this corner of LHC physics, various B-physics measurements are conducted. LHCb was designed for precision measurements of CP violation, which is crucial to understand the matter/antimatter asymmetry in our universe. These CP violation tests will include the measurement of the CP violating phase in the $B_s \rightarrow J/\psi \Phi$ decay. The analysis presented in this document has been performed within the B-Physics group at CMS. SM precision studies can give indications for BSM physics, as these studies provide complementary information with respect to the direct searches mentioned above.

2.2.6 Heavy-Ion Physics

Recent results from RHIC experiments indicate that heavy-ion collisions such as lead-lead collisions lead to a new state of matter, the quark gluon plasma (QGP) if the energy density in the collisions is sufficiently high. QGP is a state of extremely high energy density, where quarks and gluons exist freely due to the QCD phenomenon of asymptotic freedom (Sect. 4.4.1).

The most readily accessible experimental signatures include suppression of very high p_T particles, also known as *jet quenching* [3], and suppression of quarkonium states such as the J/ψ meson. The LHC will also allow presently inaccessible hard probes such as the Υ meson or the Z boson to be studied, due to increased production cross sections.

Chapter 3

The CMS Detector

3.1 Experimental Challenges

The CMS detector is a multipurpose experiment, specifically designed to explore the physics topics mentioned in Sect. 2.2 by clean detection of the decay signatures. A principal goal of CMS is the discovery of the Higgs boson, covering the mass range of 114 GeV up to 1 TeV. The specific detector requirements for CMS, to accomplish the goals of the LHC physics program can be summarized as follows [3]:

- Muon system: A good muon identification and momentum resolution is required, for a wide range of transverse momentum p_T , with a good dimuon mass resolution of at least 1% at 100 GeV.
- Inner tracking system: A good momentum resolution of charged particles and a reasonable reconstruction efficiency is required in the inner tracker, as well as good identification of b-jets, requiring silicon pixel detectors very close to the collision point, to identify secondary vertices with a good spatial resolution.
- Electromagnetic calorimeter (ECAL): A good diphoton and dielectron energy resolution of at least 1% at 100 GeV is required, as well as a large geometrical coverage of $|\eta| < 2.5$. The pseudo-rapidity η is defined as $\eta = -\ln \tan(\vartheta/2)$, with ϑ the polar angle from the beam axis. Furthermore, localization of the primary vertex and good measurement of the direction of the photons is required.
- Hadron calorimeter (HCAL): In order to have a good estimate of the missing transverse energy E_T^{miss} , good geometrical coverage of $|\eta| < 5$ and fine lateral resolution of at least 0.1 in $\Delta\eta$ and in the azimuthal angle $\Delta\varphi$ is required.

At the design luminosity of $10^{34} \text{ cm}^{-2}\text{s}^{-1}$, the design energy of $\sqrt{s} = 14 \text{ TeV}$, with the total proton-proton cross section of approximately 100 mb , 10^9 collisions are expected per second. One such collision is referred to as *event*. The proton bunches collide in a 25 ns collision scheme, corresponding to 40 MHz . In one bunch crossing, 20 collisions are expected on average (*pile-up*). This leads to a number of experimental challenges and requires very sophisticated trigger systems to select the *interesting* events. The trigger system has to reduce the number of events to approximately 100 Hz , which will be stored and further processed for physics analysis. The rate of 100 Hz is the nominal design value, currently 300 Hz are stored. In order to separate the individual events high granularity of the detectors and good time resolution are required, resulting in a large number of electronic readout channels of CMS, which have to be synchronized [3].

Section 3.2 defines the CMS coordinate system, necessary for the following considerations. Section 3.3 gives an overview of the overall CMS detector layout. The individual subcomponents of CMS, which are relevant for the analysis presented in this thesis, will be described in Sect. 3.4, described in more detail in Ref. [3]. The CMS trigger system will then be described in Sect. 3.5.

3.2 Coordinate Conventions

The global coordinate system of CMS is centered at the nominal collision point. The z axis points along the direction of the beam, pointing westwards. The x axis is horizontal, pointing inwards to the center of the LHC ring. The y axis is vertical, pointing upwards. The polar angle ϑ is measured with respect to the z axis, the azimuthal angle φ is measured in the x - y plane [3].

The values of transverse momentum p_T and transverse energy E_T are measured from the values of the respective x and y components [3].

3.3 Detector Overview

The main features of the CMS detector are the 3.8 T superconducting solenoid, the fully silicon based inner tracking system, the crystal based ECAL, the HCAL and the outer muon systems. The total dimensions of CMS are a length of 21.6 m , a diameter of 14.6 m and a total weight of 12500 tons , mostly due to the heavy iron return yoke [3]. Figure 3.1 shows an overview of the detector layout.

In the core of the detector is the 5.8 m long, 2.6 m diameter inner tracking system, consisting of 3 layers of silicon pixel detectors and 10 layers of silicon micro strip detectors. The tracking system is surrounded by the ECAL, using lead tungstate

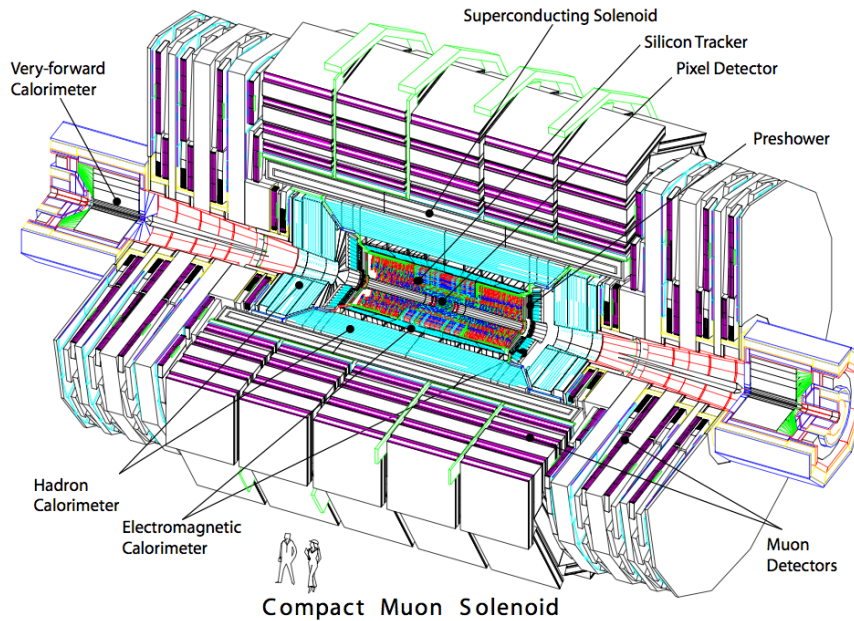


Figure 3.1: A cut-away view of the CMS detector [3].

(PbWO_4) to produce scintillating light from photons and electrons. The light is detected by photodiodes. The HCAL, surrounding the ECAL, is a brass/scintillator sampling calorimeter. The heart of CMS is the 3.8 T superconducting solenoid, 12.9 m long and with 5.9 m inner diameter. The return field saturates the 1.5 m thick iron return yoke. The muon systems are integrated in the return yoke as *muon stations*, consisting of several layers of aluminum drift tubes (DT), cathode strip chambers (CSC) and resistive plate chambers (RPC) [3].

Figure 3.2 shows a schematic view of particles passing through the various subsystems of CMS, and the respective subdetectors, by which they are detected and where they are stopped.

3.4 Detector Components

3.4.1 Superconducting Solenoid

The performance of the muon system is largely dependent on the bending power of the superconducting solenoid. In order to unambiguously determine the charge of the muon, especially at high p_T , a momentum resolution $\frac{\Delta p}{p}$ of approximately 10% at 1 TeV is required [3].

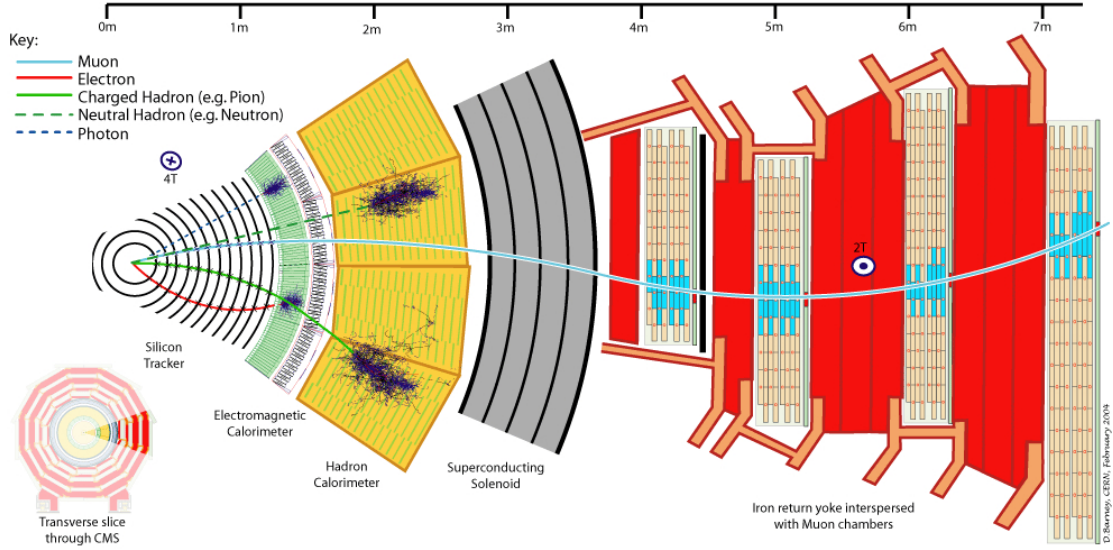


Figure 3.2: Schematic view of CMS, particles passing through subsystems of CMS [8].

A large high-field solenoid was chosen, to ensure enough bending power to fulfill the requirements. The main parameters of the solenoid are summarized in Tab. 3.1.

A high-purity aluminum stabilized conductor and indirect cooling are the main features of the solenoid. The superconducting coil is placed around the calorimeter systems, and consists of niobium-titanium filaments embedded in a copper matrix. The coil is surrounded by a 10000 ton iron return yoke, in order to close the field lines. As the total weight of the magnet system is approximately 12000 tons, it is the main contribution to the weight of the CMS detector [3].

Magnetic flux density	3.8 T
Inner bore	5.9 m
Length	12.9 m
Number of turns	2168
Current	19.5 kA
Stored energy	2.7 GJ

Table 3.1: Main parameters of the CMS solenoid [3].

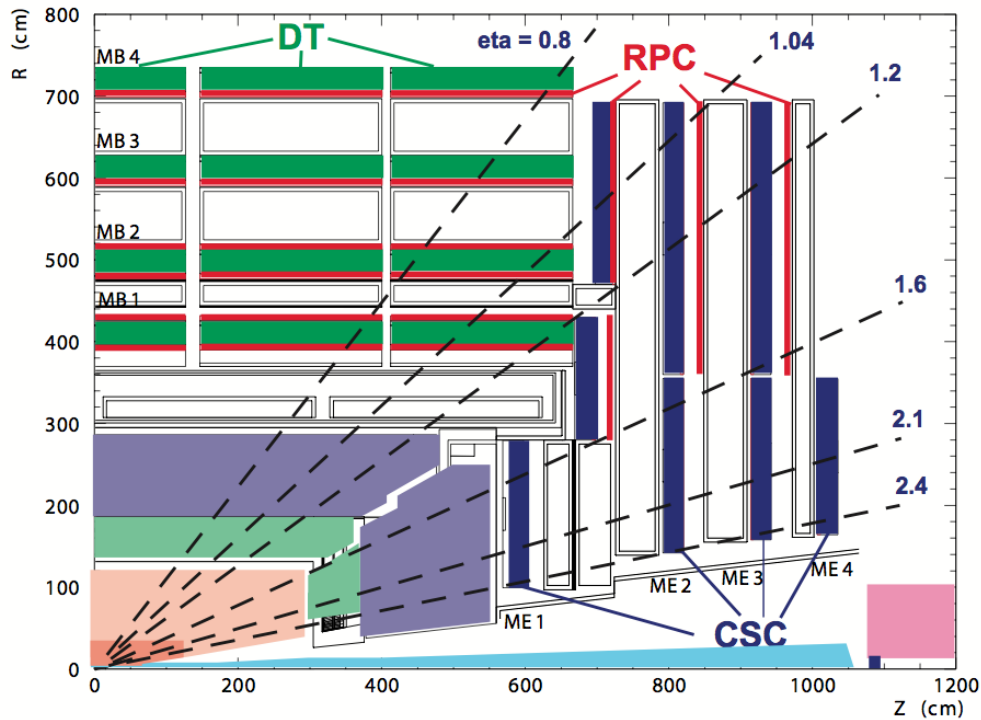


Figure 3.3: Layout of one quarter of the CMS muon system as of 2011 [3].

3.4.2 Muon System

Muons are an essential part of almost all signatures of physics signals studied at the CMS experiment (Sect. 2.2). Therefore it is important to identify muons unambiguously and to measure the muon momentum with high precision. Furthermore, the muon system is an integral part of the trigger system (Sect. 3.5). The only particles that can reach the outer muon system are muons and very weakly interacting particles such as neutrinos.

The muon momentum is measured three times: In the inner tracker, after the coil and in the return flux. While for high p_T muons the measurements of the muon system and the measurement of the inner tracker are combined to improve the momentum resolution, low p_T muons are measured with best precision exclusively with information from the silicon tracker [3].

There are three types of gaseous detectors used in the muon systems. In the barrel region drift tube chambers are installed. In the endcaps, cathode strip chambers are used. In addition to these detectors, in both regions also resistive plate chambers are deployed. Figure 3.3 shows one quarter of the CMS detector in transverse view, highlighting the layout of the muon systems. In the barrel region, there are 4 *muon stations* (MB1-MB4

in Fig. 3.3), consisting of both DT chambers and RPCs, installed separately for all five wheels of the return yoke. The endcaps consist of four disks, perpendicular to the beam pipe, with several concentric rings. In total, the muon systems cover more than 25000 m² of active detection planes [3].

Drift Tube Chambers

The drift tube system consists of 250 chambers, organized in four layers. It is installed in the barrel region, inside the return yoke. As the residual magnetic field is low in the saturated yoke, it is feasible to make use of a gas-based drift approach to detect the muons. Muons entering the chamber ionize gas molecules in the detector, the electrons and the ions drift to the respective electrodes. Given a starting time t_0 , from the known drift-velocity of the gas and the drift-time one can then calculate the coordinates of the muon with a resolution of approximately 100 μm in position and approximately 1 mrad in direction. If a high p_T muon enters the muon system, the muon can produce up to 44 signals in the DT system, from which a candidate track can be reconstructed [3].

Cathode Strip Chambers

468 CSCs are installed exclusively in the endcaps. CSCs are multi-wire proportional chambers. There are six gas gaps in each CSC, with a plane of radial cathode strips, and a plane of anode wires, perpendicular to the cathode strips. A charged particle such as the muon, entering a CSC ionizes the gas, and induces a very fast signal in the anode wire, which is used for triggering. For the determination of the coordinates of the muon, the cathode strip signal is used. While it is not as fast as the anode signal it allows better spatial resolution. The position resolution is approximately 200 μm , the angular resolution is only approximately 10 mrad [3].

Resistive Plate Chambers

RPCs have a much faster response than DT chambers and CSCs, of the order of 1 ns, if operated in avalanche mode. Therefore RPCs can unambiguously identify the correct bunch crossing. Nevertheless, the spatial resolution is poor with respect to the other muon detectors used [3]. The signal of the RPCs is used to define the time the particle enters the DT chambers.

3.4.3 Inner Tracking System

The CMS tracking system is the innermost subdetector. Its challenge is the precise measurement of the trajectories of charged particles as well as the identification of

secondary vertices with high precision. As the 3.8 T magnetic field is almost homogeneous over the full volume of the inner tracking system, the momentum can be obtained directly from the curvature of the tracks, coming from charged particles moving through the tracker, bent by the Lorentz force induced by the magnetic field, the particle momentum and charge [9].

The total tracker system has a length of 5.8 m and a diameter of 2.5 m. At the design luminosity of $10^{34} \text{ cm}^{-2}\text{s}^{-1}$, there will be approximately 20 collisions every 25 ns, which corresponds to approximately 1000 particles entering the tracker per bunch crossing. This, of course, requires high granularity of the detector, and a fast response. To meet these requirements, closest to the interaction vertex a pixel detector was installed, surrounded by silicon strip detectors. In total, the CMS tracker system consists of 66 million pixels and 9.6 million silicon strips, which represent an area of 1 m^2 and 200 m^2 , respectively [9].

Pixel Tracker

Closest to the interaction vertex, at radii of 4.4 cm, 7.3 cm and 10.2 cm, three barrel pixel detector layers are installed. The individual pixel cells have a size of $100 \times 150 \text{ } \mu\text{m}^2$

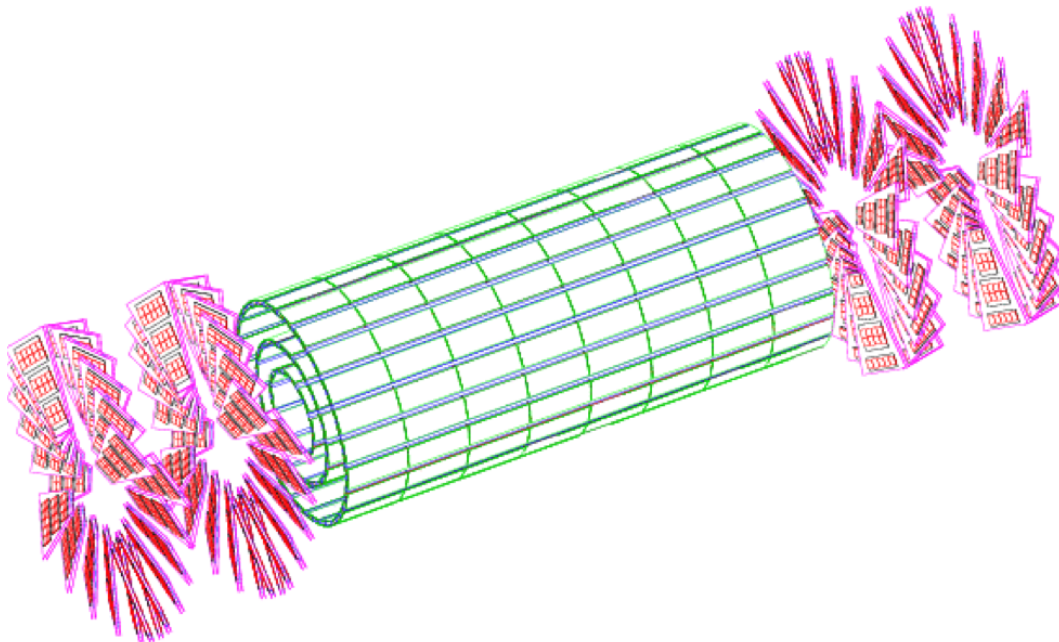


Figure 3.4: Layout of the pixel detectors in the CMS tracker [3].

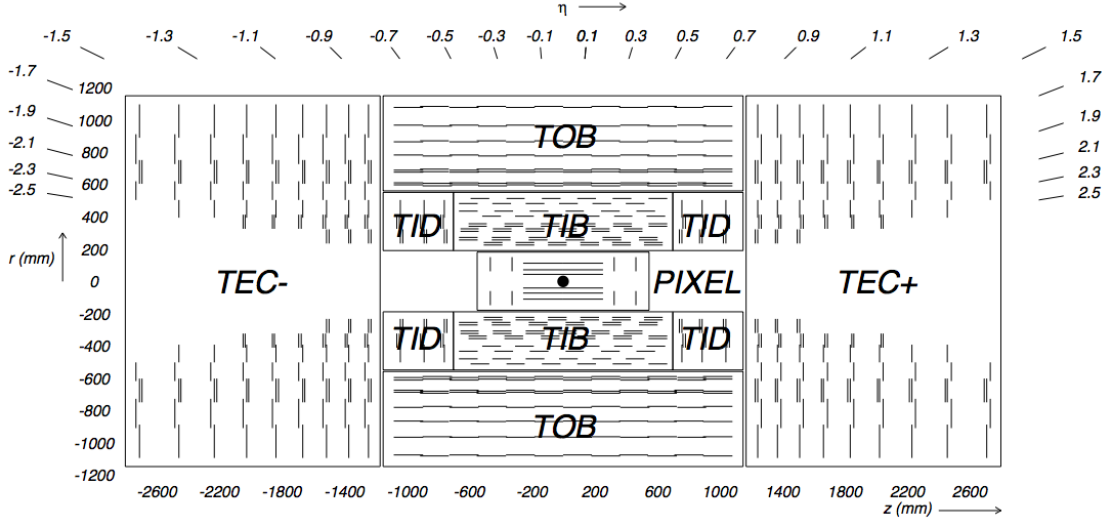


Figure 3.5: Layout of the inner tracking system [9].

and are grouped on pixel detector modules. The barrel pixel tracker is completed by two endcap pixel layer discs. The barrel tracker has a length of 53 cm, the endcap pixel layer discs are installed at $|z|$ of 34.5 cm and 46.5 cm. Figure 3.4 shows the layout of the total pixel tracker [9].

Strip Tracker

The pixel tracker is surrounded by the silicon microstrip tracker. The barrel silicon strip tracker is divided in two regions, the tracker inner barrel (TIB) and the tracker outer barrel (TOB). In the TIB, the silicon strips have a size of approximately $10 \text{ cm} \times 80 \mu\text{m}$, whereas the size in the TOB is approximately $25 \text{ cm} \times 180 \mu\text{m}$ [3]. The endcap region consists of the tracker inner disks (TID) and the tracker endcap (TEC), covering a pseudo-rapidity range of $|\eta| < 2.4$ [3]. The overall layout of the tracker system is shown in Fig. 3.5.

3.5 The CMS Trigger System

At the LHC design luminosity of $10^{34} \text{ cm}^{-2}\text{s}^{-1}$ the bunch crossing rate will be 40 MHz. With current technology it is impossible to read out and store such an amount of data. The maximal rate that can be stored is of the order of 100 Hz, corresponding to a rejection factor of approximately 10^6 . This selection is called *triggering*.

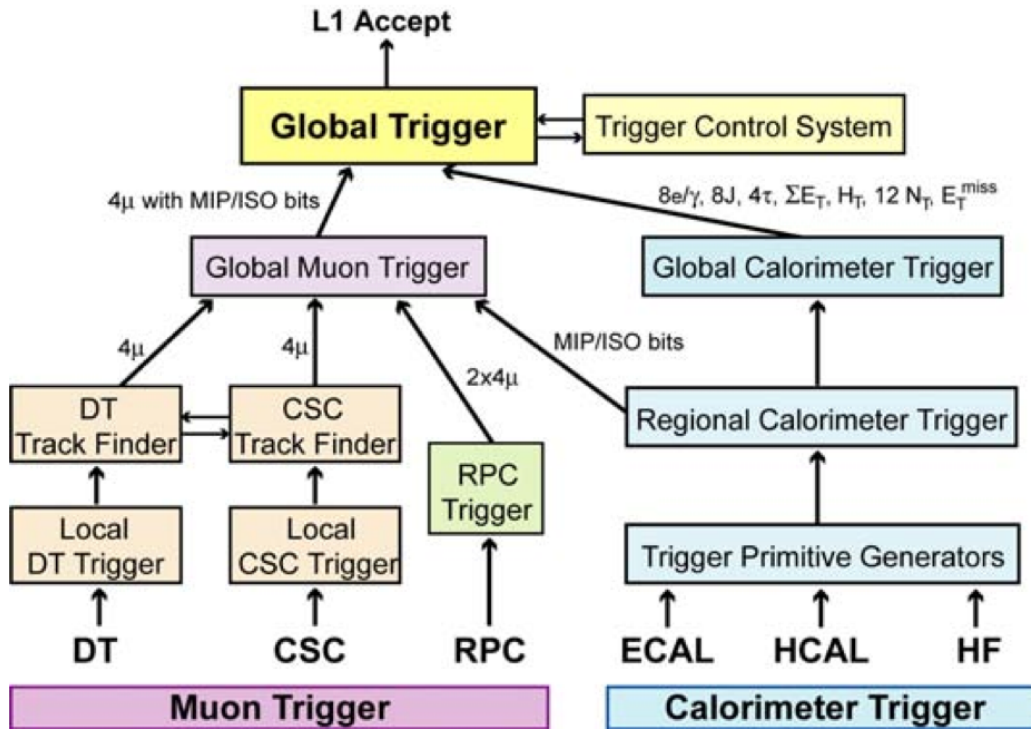


Figure 3.6: Architecture of the L1 trigger at CMS [9].

To maximize the amount of interesting events stored, a sophisticated trigger system was developed, which takes several physical observables into account, to be able to keep interesting events.

The CMS trigger system is a two-stage trigger system, subdivided in the hardware-based *Level 1* (L1) trigger and the software-based *High Level Trigger* (HLT).

3.5.1 Level 1 Trigger

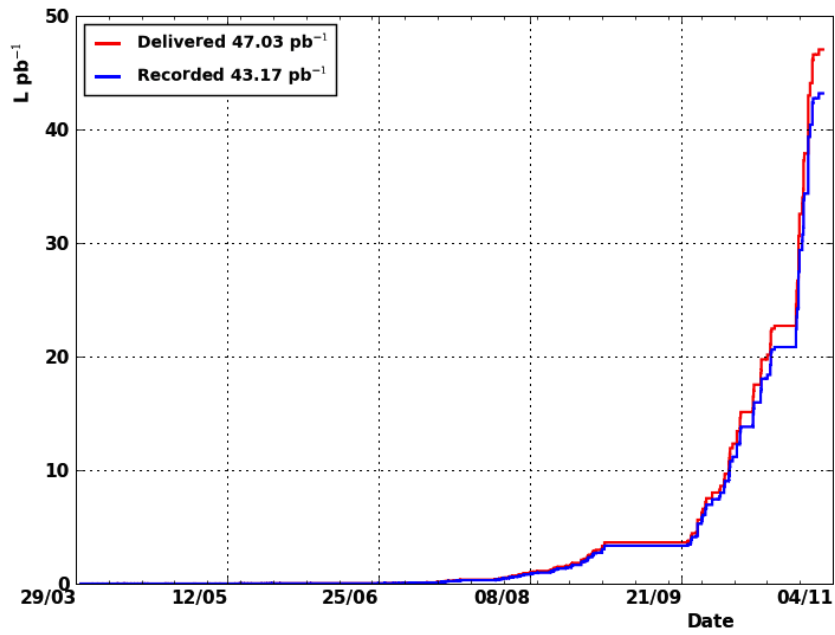
The L1 triggers use information from calorimetry and from the muon systems, as well as combined information from the two systems. It is a hardware-based trigger system, which is flexible in a certain sense, as FPGA technology was implemented. The total time for reaching the L1 front-ends and reaching the decision is approximately $3 \mu\text{s}$. During this time the event has to be stored in a buffer. After this trigger step, the initial 40 MHz have to be reduced to at most 100 kHz. Figure 3.6 shows the architecture of the L1 trigger [3].

3.5.2 High Level Trigger

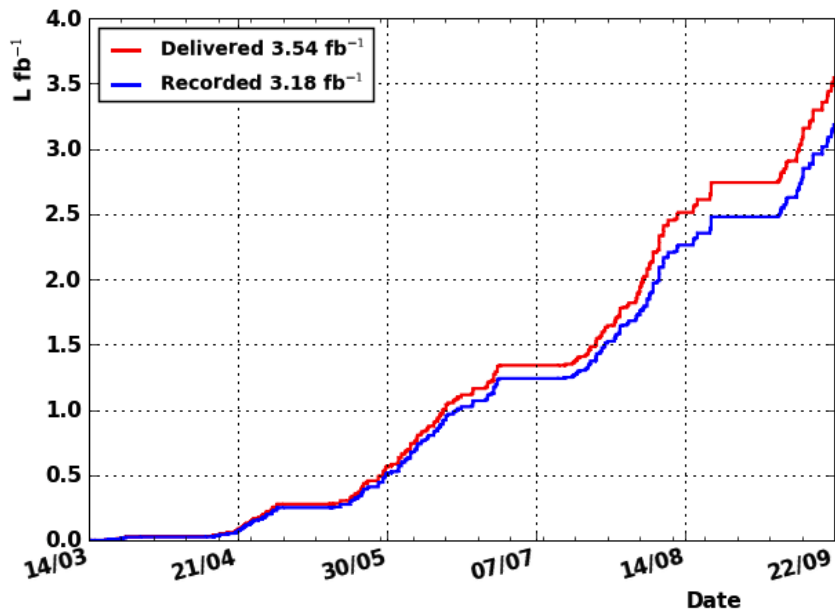
If the L1 decision is positive, the data is transferred to front-end readout buffers. The HLT decision is processed on approximately 1000 processors on a filter farm, where events are selected based on reconstructed particles, jets or quantities such as E_T^{miss} . The corresponding algorithms can be of varying complexity. The event can either be reconstructed with the information of all subsystems or, in order to reduce the amount of time needed for the HLT to gain a decision, the algorithms can only make use of the subdetector systems that are relevant for the corresponding analysis (e.g. dimuon triggers, where no information from calorimetry is needed). After the HLT step, the rate has to be reduced to around 100 Hz [3].

3.5.3 Collected Data and Luminosity

The LHC accelerator team provided excellent beam conditions, with instantaneous luminosities in excess of those expected in this early stage of LHC operation. Figure 3.7 (a) shows the delivered and collected integrated luminosity of CMS in the year 2010. The instantaneous luminosity peaked at $2.05 \cdot 10^{32} \text{ cm}^{-2}\text{s}^{-1}$. In total, $\hat{L}(2010) = 43.17 \text{ pb}^{-1}$ were recorded [10]. In 2011 the instantaneous luminosity was increased dramatically, and as of September 22nd, the highest instantaneous luminosity delivered by the LHC to the CMS collision point was $3.16 \cdot 10^{33} \text{ cm}^{-2}\text{s}^{-1}$, the integrated luminosity in 2011 amounting to $\hat{L}(2011) = 3.18 \text{ fb}^{-1}$ (Fig. 3.7 (b)) [11]. This corresponds to an increase by a factor of ~ 74 with respect to 2010 data.



(a)



(b)

Figure 3.7: Integrated luminosity, delivered by LHC and collected by CMS in 2010 [10] (a) and 2011 [11] (b).

Chapter 4

Quarkonium Physics

4.1 Introduction to Quarkonium Physics

In the late 1940's and in the 1950's a large number of hadronic particles were discovered at various high energy physics and cosmic ray experiments. This newly discovered *particle zoo* led to some confusion in the particle physics community, until in 1964 Murray Gell-Mann and Yuval Ne'eman proposed a new model formulated in the SU(3) symmetry group, known as *the eightfold way*. This approach allowed to organize the baryons and mesons in octets and decuplets, characterizing the hadrons in terms of isospin, charge and strangeness. This proposition led to the suggestion that all hadronic particles are constructed from fundamental particles, which we now know as quarks. All known hadrons at that time could be implemented in these multiplets with the help of the up, down and strange quarks.

As all searches for free quarks failed, which we now can attribute to the QCD phenomenon of confinement (Sect. 4.4.1), it was not clear whether the quark formalism only provides a set of mathematical tools to describe hadronic particles, or whether quarks have a true existence. Deep inelastic scattering experiments at the Stanford Linear Accelerator (SLAC) indicated that protons have point-like subconstituents, which supported the hypothesis of the real nature of quarks.

One important step for the understanding of hadrons was the introduction of the GIM (Glashow, Iliopoulos and Maiani) mechanism in 1970, which predicted a fourth quark, the charm quark, to explain the suppression of the electroweak decay $K^0 \rightarrow \mu^+ \mu^-$. In 1973, Makoto Kobayashi and Toshihide Maskawa published a paper that predicted a third generation of quarks, now known as the beauty quark and the top quark.

In 1974 the Brookhaven National Laboratory (BNL) [12] and SLAC [13] simultaneously reported the discovery of a new resonance, as shown in Fig. 4.1, measured

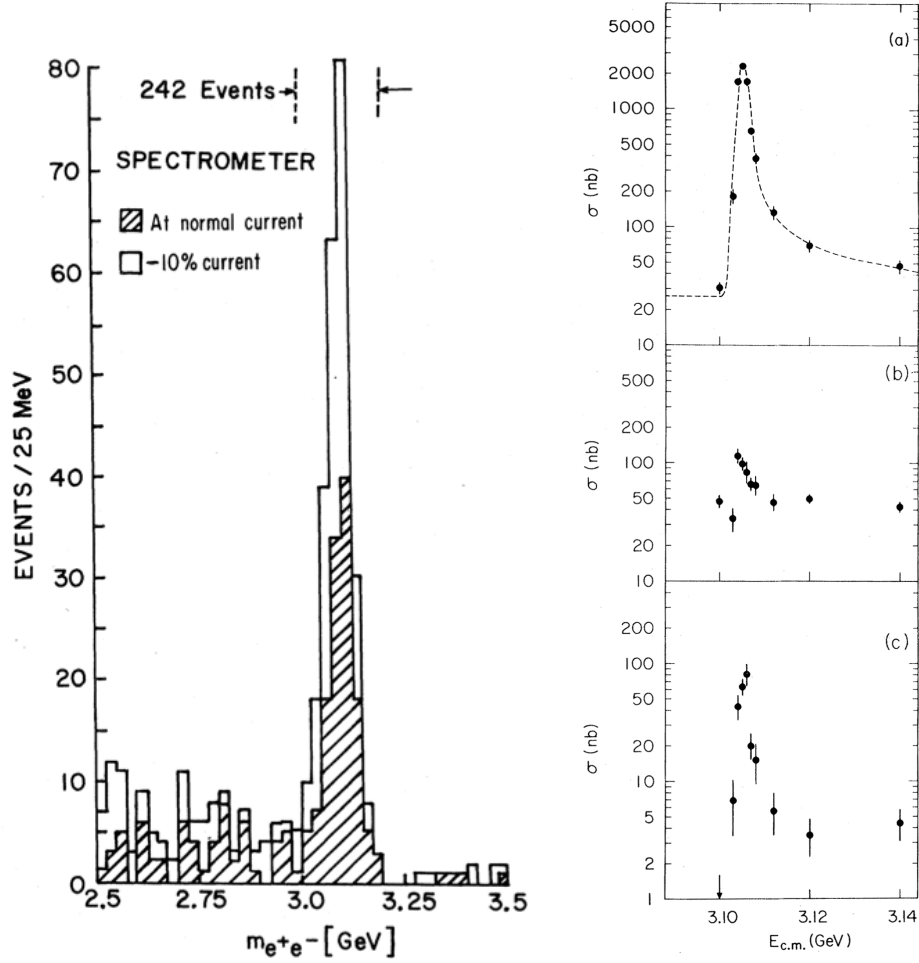


Figure 4.1: (left) First observation of the J/ψ at BNL in p+Be collisions, measured in the dielectron mass spectrum [12]. (right) e^+e^- collisions at SLAC, cross section versus center of mass energy, with J/ψ going to (a) multi-hadron final states, (b) e^+e^- final states and (c) $\mu^+\mu^-$, $\pi^+\pi^-$ and K^+K^- final states [13].

at a mass of approximately 3.1 GeV, which was given the name J/ψ . This discovery was the first clear experimental sign of the charm quark and opened a new field in particle physics - *Quarkonium Physics*.

Quarkonium particles are bound states of a heavy quark and a heavy antiquark. They are color neutral uncharged mesons, except for the charged B_c , and exist in various states. In general, all $c\bar{c}$ and $b\bar{b}$ bound states are considered quarkonia. As the lifetime of a single top or anti-top quark is smaller than the annihilation time of a $t\bar{t}$ pair, due to its large mass, it is hardly possible to hadronize into a bound quarkonium $t\bar{t}$ state.

Shortly after the discovery of the J/ψ , the $\psi(2S)$ was discovered also in the dielectron

channel - in this document, the $\psi(2S)$ meson will be referred to as ψ' . Later also the P wave states χ_{cj} were discovered, in the decay $\psi' \rightarrow \chi_{cj} \gamma$. The discoveries of the charmed quarkonia were soon followed by the discovery of the first $b\bar{b}$ state, the $\Upsilon(1S)$, and the corresponding excited states at Fermilab. After these discoveries, the properties of the quarkonium meson family were studied in much detail, which raised intriguing questions.

The leptonic decay modes have branching ratios of approximately 5.9% for both, $J/\psi \rightarrow \mu^+\mu^-$ as well as $J/\psi \rightarrow e^+e^-$. It was not expected that the leptonic decay modes can compete with hadronic decays, but luckily they can, as leptonic decays are easily detectable at detectors such as CMS. For comparison, the Φ meson ($s\bar{s}$) has a branching fraction of approximately 0.03% in the decay $\Phi \rightarrow \mu^+\mu^-$, a factor of $\sim 2 \cdot 10^2$ smaller with respect to the branching fraction of the J/ψ dimuon decay [14]. The reasons for the unexpectedly large leptonic branching fractions can be explained by a few simple considerations. A heavy quark pair can neither decay into a single gluon due to color conservation, nor can it decay in two gluons, because of CP conservation. So the lowest order hadronic decay would be a three gluon decay, e.g. $J/\psi \rightarrow \pi^+\pi^0\pi^-$ [15]. Furthermore, considering the OZI rule proposed by Okubo, Zweig, and Iizuka independently, hadronic decays are suppressed if they can only happen by annihilation of heavy quark-antiquark pairs. In other words, strong processes that can be cut into two parts by only cutting internal gluon lines are suppressed (Fig. 4.2). These considerations also apply to the ψ' and the $\Upsilon(nS)$ states. The χ_{cj} states decay faster and have approximately 10-100 times the width of the J/ψ .

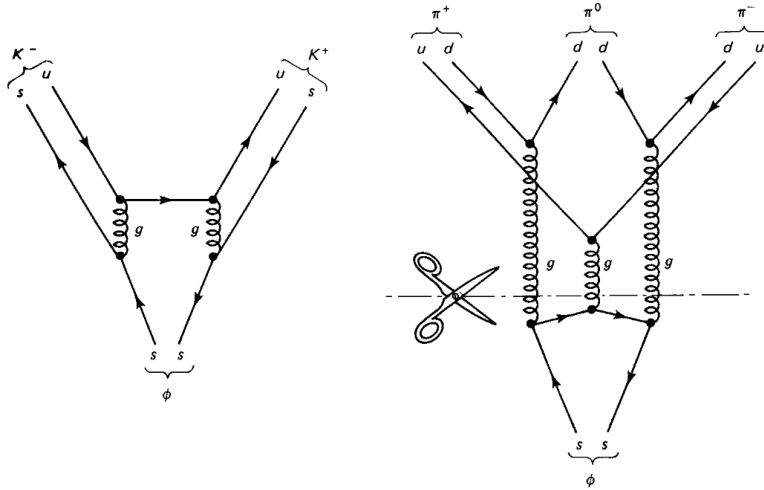


Figure 4.2: Unsuppressed decay $\Phi \rightarrow K^+K^-$ (left) and OZI-suppressed $\Phi \rightarrow 3\pi$ decay (right), analogue for the decay $J/\psi \rightarrow 3\pi$ [16].

4.2 The Quarkonium Spectrum

In this section a short overview of the properties and angular states of the quarkonium meson family is given. In the framework of non-relativistic QCD, which can be applied in the limit of high masses, quarkonia are defined by the total spin S , the angular momentum L and the total angular momentum $J = S + L$. As parity $P = -1^{(L+1)}$ and charge conjugation $C = -1^{(L+S)}$ are conserved, quarkonia are usually represented as J^{PC} . The spectroscopic notation of $n^{(2S+1)}L_J$, where n is the principal quantum number, is useful as well. Table 4.1 summarizes the angular states, the masses and full widths of the quarkonium mesons relevant in this thesis.

Meson	J^{PC}	$n^{(2S+1)}L_J$	Mass [MeV]	Full Width
J/ψ	1^{--}	1^3S_1	$3\,096.916 \pm 0.011$	92.9 ± 2.8 keV
χ_{c0}	0^{++}	1^3P_0	$3\,414.75 \pm 0.31$	10.3 ± 0.6 MeV
χ_{c1}	1^{++}	1^3P_1	$3\,510.66 \pm 0.07$	0.86 ± 0.05 MeV
χ_{c2}	2^{++}	1^3P_2	$3\,556.20 \pm 0.09$	1.97 ± 0.11 MeV
ψ'	1^{--}	2^3S_1	$3\,686.09 \pm 0.04$	304 ± 9 keV
$\Upsilon(1S)$	1^{--}	1^3S_1	$9\,460.30 \pm 0.26$	54.02 ± 1.25 keV
$\chi_{b0}(1P)$	0^{++}	1^3P_0	$9\,859.44 \pm 0.42 \pm 0.31$	-
$\chi_{b1}(1P)$	1^{++}	1^3P_1	$9\,892.78 \pm 0.26 \pm 0.31$	-
$\chi_{b2}(1P)$	2^{++}	1^3P_2	$9\,912.21 \pm 0.26 \pm 0.31$	-
$\Upsilon(2S)$	1^{--}	2^3S_1	$10\,023.26 \pm 0.31$	31.98 ± 2.63 keV
$\chi_{b0}(2P)$	0^{++}	2^3P_0	$10\,232.5 \pm 0.4 \pm 0.5$	-
$\chi_{b1}(2P)$	1^{++}	2^3P_1	$10\,255.46 \pm 0.22 \pm 0.50$	-
$\chi_{b2}(2P)$	2^{++}	2^3P_2	$10\,268.65 \pm 0.22 \pm 0.50$	-
$\Upsilon(3S)$	1^{--}	3^3S_1	$10\,355.2 \pm 0.5$	20.32 ± 1.85 keV

Table 4.1: Properties of the quarkonium meson family [14].

Bound states of $c\bar{c}$ are generally named *charmonium*, bound states of $b\bar{b}$ are referred to as *bottomonium*. The charmonium and bottomonium spectra are shown in Figs. 4.3 and 4.4. These figures also visualize the important *feed-down* contributions to the 1S states, which will be further discussed in Sect. 5.6. Feed-down generally refers to decays from heavier states to the state that is the subject of the analysis, which can be a significant contribution to the data sample under study and can cause considerable problems if not well understood.

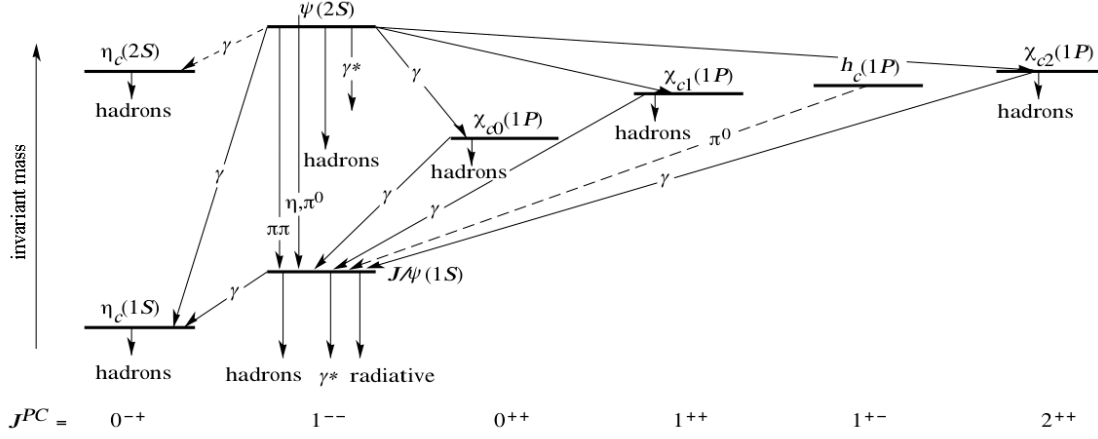


Figure 4.3: Charmonium spectrum and decays [14].

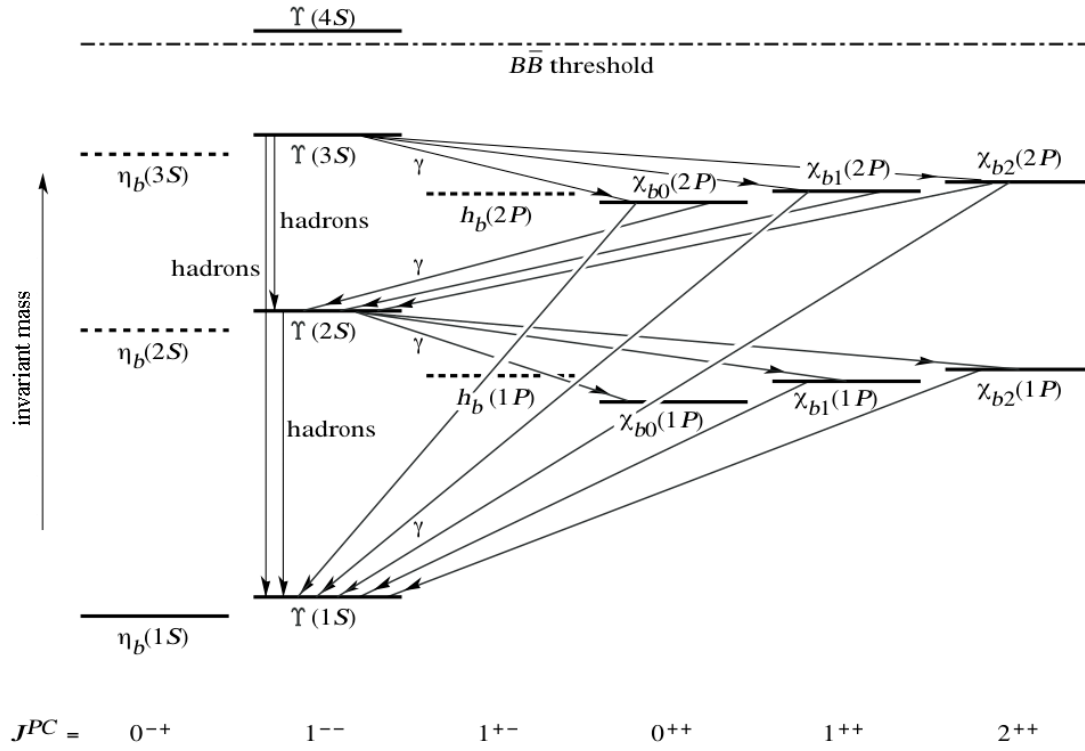


Figure 4.4: Bottomonium spectrum and decays [14].

4.3 Quarkonium as Probe in QCD

Charmonium and *bottomonium* are akin to the e^+e^- bound state positronium. As positronium and hydrogen are considered the simplest objects to study the electrostatic Coulomb force described by QED, in a way, charmonium and bottomonium are analogue objects for a detailed study of the strong interaction described by QCD. Despite the very different mass range and underlying fundamental interactions, the respective spectra show similarities to the ones of quarkonia.

Indeed, quarkonia are used to conduct precision measurements of QCD parameters such as the strong coupling α_s . In the determination of inclusive B-decays, a precise knowledge of the charm and bottom quark masses is necessary. Quarkonium studies can help to better constrain these parameters [17].

Quarkonia also play a central role in ultra-relativistic heavy-ion physics, as already pointed out in Sect. 2.2.6, which will also be probed at LHC experiments. At very high energy densities, the so called *quark gluon plasma* (QGP) is expected to be produced, a hot and dense phase of deconfined quarks and gluons. Quarkonia can survive this phase transition because of their small size. But due to color screening and other phenomena [17], quarkonia will eventually *melt* in the QGP, at a certain energy density. This phenomenon is called *quarkonium suppression*, and a precise measurement of the critical energy density (depending on the quarkonium because of differing binding energies) will lead to a better understanding of the basic properties of the QGP [17].

Summarizing the situation in quarkonium physics, one can say that the spectroscopy and the decay mechanisms of the quarkonium systems are fairly well understood. However, the mechanisms of quarkonium production are still not satisfactorily described.

4.4 Quarkonium Production

This section gives an overview of currently favored models describing quarkonium production and their success in terms of describing experimental results. The fundamental idea of all quarkonium production considerations is the factorization theorem (Eq. 4.7). It states that quarkonium production can be factorized in two independent phases:

1. The first phase is the formation of a quark-antiquark ($q\bar{q}$) pair, which can be described by perturbative QCD (described by *short distance coefficients*) and is fairly well understood.
2. The second phase is the formation of the physical bound quarkonium state, which is in the realm of non perturbative QCD (described by *long-distance matrix*

elements), and even after four decades of experimental and theoretical work in this field, this part of quarkonium production still needs clarification.

The core question that the individual models approach differently is the relation between the color, spin and angular momentum state of the initial $q\bar{q}$ pair and the final quarkonium state.

In order to present the assumptions and consequences of the individual models, a very short introduction to general phenomena of Quantum Chromodynamics will be given, as this is the starting point for all following considerations. The individual quarkonium production models will not be presented in chronological order.

The Non-Relativistic QCD (NRQCD) factorization approach will be discussed first, including the Color Octet Model (COM). The COM allows a transition of a produced $q\bar{q}$ pair from a color octet state into a physically bound color singlet state by emission of soft gluons.

Then, the Color Singlet Model (CSM) will be discussed. The CSM only allows color singlet $q\bar{q}$ pairs to form a bound quarkonium state.

The Color Evaporation Model (CEM) will also be discussed. The CEM is similar to the COM in the sense that any initial $q\bar{q}$ color, spin and angular momentum state can form the bound quarkonium state, by neutralizing the color in interactions with a collision-induced color field (*color evaporation*).

The individual quarkonium production models will be discussed considering proton-proton collisions only, although these models find application in many production channels such as $e^+ - e^-$ collisions and proton-nucleon interactions in fixed target experiments.

4.4.1 A Short Introduction to Quantum Chromodynamics

Quantum Chromodynamics describes the strong interaction and is part of the standard model of particle physics. It can be written as a Yang-Mills (YM) theory with local gauge symmetry $SU(3)$, which indicates the three color charges. QCD describes the strong interaction effective between the quarks (6 Dirac fields in the YM theory, categorized in three flavors), mediated by gluons (8 vector fields in the YM Lagrangian). The QCD Lagrangian reads

$$\mathcal{L}_{QCD} = -\frac{1}{4}F_{\mu\nu}^a F^{a\mu\nu} + \sum_{\{q\}} \bar{q}(i\gamma^\mu D_\mu - m_q)q, \quad (4.1)$$

with

$$\{q\} = u, d, s, c, b, t, \quad (4.2)$$

$$F_{\mu\nu}^a = \partial_\mu A_\nu^a - \partial_\nu A_\mu^a + g f^{abc} A_\mu^b A_\nu^c, \quad (4.3)$$

$$D_\mu = \partial_\mu - iT^a A_\mu^a, \quad (4.4)$$

with f^{abc} the SU(3) structure constants, and T^a the basis of the fundamental representation of the SU(3) algebra [17].

The main properties and phenomena of QCD can be summarized as follows [17]:

- QCD is parity, time reversal, charge conjugation invariant and invariant under U(1) transformations, which implies flavor conservation.
- Physical states have to be color neutral.
- QCD allows two quarks ($q\bar{q}$) to form a meson (boson) and three quarks to form a baryon (fermion). Other bound quark states such as *penta quarks* or *dimeson molecules* have not been experimentally confirmed, but are not yet excluded either.
- The QCD coupling constant α_s decreases with increasing momentum transfer. This implies that QCD can be treated perturbatively at high energies and therefore short distances ($\alpha_s < 1$). This fact leads to the phenomenon of *asymptotic freedom*, as quarks and gluons interact very weakly in this energy region.
- At low energy scales and long distances the coupling α_s exceeds 1. This leads to the phenomenon of *confinement* and to the fact that quarks can never exist freely. In this energy regime, QCD has to be treated with non perturbative methods. This fact causes considerable problems in the calculation of cross sections and other observables. This is conducted, for example, with lattice QCD methods.
- The parameter that determines the transition of perturbative to non perturbative QCD is the *QCD energy scale* $\Lambda_{QCD} = O(10^2 \text{ MeV})$. If the energy of the QCD process is far above Λ_{QCD} , α_s is below 1 and perturbative calculations can be applied.
- In distinction to one electrical charge in QED, QCD has three color charges. Furthermore, the intermediate gluon carries color charge itself, which leads to self interactions that have to be considered.

In analogy with the treatment of positronium and of the hydrogen atom in QED, the first approach to treat quarkonium production was to treat quarkonium as a non-relativistic system, applying the Schrödinger equation with a certain choice of potential.

There were many approaches for the choice of this potential, generally starting with a Coulomb like potential to describe the exchange of gluons between the non-relativistic quarks [15]

$$V_s^0(r) = \frac{\alpha_s(r)}{r}. \quad (4.5)$$

As this potential cannot describe the phenomenon of confinement, usually a term increasing with distance r was added

$$V_s(r) = V_s^0(r) + f(r). \quad (4.6)$$

These potential models - although they had success in describing quarkonia spectra - are limited, as they neglect relativistic and quantum effects such as spin dependencies. However, these potential models helped in the understanding of quarkonium production in an early stage and qualify as an important starting point for the models that will be discussed in the following sections.

4.4.2 The Non-Relativistic QCD (NRQCD) Factorization Approach

As the charm and bottom quark masses are much larger than Λ_{QCD} , the coupling constant is less than unity ($\alpha_s(m_c) \sim 0.25$, $\alpha_s(m_b) \sim 0.18$ [17]). Therefore, quarkonium production should, in principle, be calculable by perturbative calculations. However, non perturbative effects of the bound quarkonium state cannot be neglected, and therefore a direct use of perturbation theory is not suitable.

This problem is approached in the effective field theory of NRQCD, that treats quarkonia as a non-relativistic system. The non-relativistic quarkonium can be characterized by three typical energy scales [15], depending on v_q , the relative velocity of the bound quarks in the center of mass frame of the quarkonium:

- The scales, at which the quarkonium is treatable with perturbative QCD, determined by the quark mass m_q .
- The kinetic energy $m_q v_q^2$, identified with the energy scale Λ_{QCD} . For charmonia and bottomonia this results in $v_c^2 \sim 0.25$ and $v_b^2 \sim 0.09$, respectively. The velocity v_q is expressed in natural units, it therefore never exceeds 1.
- The typical momentum transfer $m_q v_q$, which defines the typical size of a quarkonium state.

In order to use perturbative calculations, one has to carefully factorize the short-distance coefficients, characterized by high momentum transfer, from the long-distance matrix

elements, characterized by low momentum transfer. With this factorization approach, one can calculate the cross sections of directly produced quarkonia \mathcal{Q} in hadronic collisions by a sum over the product of long-distance (NRQCD) matrix elements and short-distance coefficients (the *NRQCD factorization theorem*) [17] [15]

$$\sigma(\mathcal{Q}) = \sum_n \sigma[q\bar{q}(n)] \langle \mathcal{O}^{\mathcal{Q}}(n) \rangle. \quad (4.7)$$

The summation is done over all possible $q\bar{q}$ states n , which are characterized by the set of color, spin and angular momentum quantum numbers in the notation $^{2S+1}L_J^{(color\ multiplicity)}$. The short-distance coefficients $\sigma[q\bar{q}(n)]$ are essentially the cross sections of the individual partonic processes to produce a $q\bar{q}$ pair in state n , convoluted with the parton density functions of the proton, and therefore process dependent. The long-distance matrix elements $\langle \mathcal{O}^{\mathcal{Q}}(n) \rangle$ contain all non perturbative physics in the process of quarkonium production and define the probability of a $q\bar{q}$ state n to form a bound quarkonium state \mathcal{Q} . These elements are analogue to parton fragmentation functions. As the NRQCD matrix elements are process independent and therefore universal, the NRQCD factorization approach has great predictive power [17].

One should mention that the NRQCD factorization approach described by Eq. 4.7 is not a model, but a direct consequence of full QCD (in the limit of $m_q \rightarrow \infty$) [17].

4.4.3 Color Octet Model (COM)

NRQCD does not allow one to calculate the long-distance matrix elements accurately. However, due to *velocity scaling rules* one can determine the relative importance of each term. Therefore one can expand the sum in Eq. 4.7 up to a certain power of v_q , and then truncate the series. The COM uses a simple truncation and includes four terms in the sum, up to the order of v_q^4 , to calculate the J/ψ cross section. It includes the possibility of producing the $c\bar{c}$ pair in a color octet state, which is color neutralized by emission of soft gluons in the hadronization process [17].

The four independent matrix elements, in this case, consist of one color singlet matrix element and three color octet matrix elements, and can be identified as

$$\langle \mathcal{O}^{J/\psi}(^3S_1^{(1)}) \rangle, \langle \mathcal{O}^{J/\psi}(^1S_0^{(8)}) \rangle, \langle \mathcal{O}^{J/\psi}(^3S_1^{(8)}) \rangle, \langle \mathcal{O}^{J/\psi}(^3P_0^{(8)}) \rangle. \quad (4.8)$$

Due to the velocity scaling rules, the color octet matrix elements are suppressed with respect to the color singlet matrix elements by a factor of v_q^2 . Of course, also the relative sizes of the short-distance coefficients $\sigma[q\bar{q}(n)]$ are important in the determination of the significance of the individual contributions. They show a strong dependence on the

coupling α_s and on various kinematic factors. It is, therefore, not a priori clear that color singlet contributions dominate the full phase space [17].

Moreover, the COM predicts color octet contributions to dominate quarkonium production in certain regions in phase space, such as in hadronic collisions at high p_T .

The four matrix elements allow one to calculate the cross sections of all three possible J/ψ spin states, and therefore allow an unambiguous calculation of the polarization of the J/ψ . This strongly enhances the prediction power of this model, as the polarization is a very important observable in the discrimination of the individual models.

On the other hand, the four matrix elements cannot be calculated by theory, but must be determined by fits to experimental data. Therefore, this model cannot give absolute predictions of quarkonia cross sections.

4.4.4 Color Singlet Model (CSM)

The CSM assumes that the initially produced $q\bar{q}$ pair has the same spin and color state as the final quarkonium state. The produced quarkonium is therefore completely determined by the original quantum numbers of the initial state. As a physical object has to be color neutral and therefore a color singlet state, the CSM only allows color singlet $q\bar{q}$ pairs to contribute to quarkonium production. This is the origin of the name of the model. Figure 4.5 (a) shows a leading order diagram for CSM production.

The CSM is a special case of the NRQCD factorization approach and one obtains the formulation of the CSM if one drops all color octet terms in Eq. 4.7, and all color singlet terms except the one that has the same quantum numbers as the final state [17].

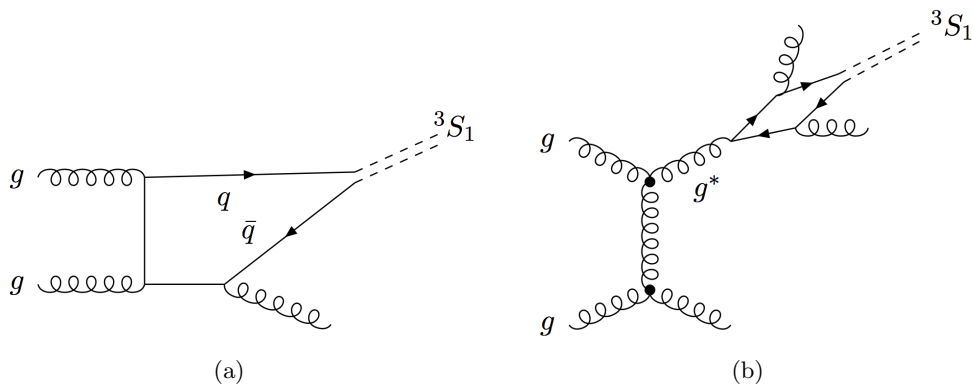


Figure 4.5: Leading order diagram for CSM production of a 3S_1 quarkonium (a). Production of a 3S_1 quarkonium due to a fragmentation process (b) [15].

The CSM J/ψ cross section can therefore be written as

$$\sigma(J/\psi) = \sigma[q\bar{q}(n_{J/\psi})] \langle \mathcal{O}^{J/\psi}(n_{J/\psi}) \rangle, \quad (4.9)$$

with $n_{J/\psi}$ being the color singlet $^3S_1^{(1)}$ J/ψ state. The only contributing long-distance matrix element $\langle \mathcal{O}^{J/\psi}(n_{J/\psi}) \rangle$ is completely determined by the wave function of the quarkonium and can be either determined by potential model approaches (Sect. 4.4.1) or experimentally from the decay width of the quarkonium state [15], as the production matrix element is related to the decay matrix element.

The CSM predicts absolute values for cross sections and therefore has great predictive power. However, predictions of quarkonium polarization are non trivial.

Additional contributions

From comparisons of predictions and measurements (Sect. 4.4.6) it became clear that quarkonium production cannot be described by the CSM alone. Additional contributions are needed to explain not only the overall normalization (that was too low by more than one order of magnitude), but also the shape of the differential cross section at high p_T , which falls too steeply.

Fragmentation contributions were considered to complete the CSM picture. Fragmentation processes occur when a high p_T parton (usually a gluon) fragments into a $q\bar{q}$ pair that then hadronizes in a quarkonium. Figure 4.5 (b) shows the diagram describing the production of a 3S_1 quarkonium due to a fragmentation process.

One should mention that the CSM is theoretically inconsistent in case of non zero orbital angular momentum, as it leads to infrared divergencies, which can only be removed by adding color octet matrix elements to the sum [17].

4.4.5 Color Evaporation Model (CEM)

The CEM is somewhat similar in philosophy to the COM, as it also allows $q\bar{q}$ pairs in color octet states to contribute to the total quarkonium cross section, in addition to the color singlet states. The model assumes that the production of a certain quarkonium does not depend on the initial $q\bar{q}$ color and spin state, as the color and spin state is modified by numerous interactions of the $q\bar{q}$ pair with the collision-induced color field during the hadronization process.

The CEM can be seen as special case of the NRQCD factorization approach and obtained by assuming that the long-distance matrix elements in Eq. 4.7 are proportional

to the expectation value of an operator, that can be obtained by replacing the projector onto the quarkonium state \mathcal{Q} by the projector onto the $q\bar{q}$ state [17].

The CEM chooses a statistical approach. The cross section for the production of a certain quarkonium is proportional to the cross section of producing a $q\bar{q}$ pair in any state, within a mass range between twice the mass of the quark and the threshold for the production of mesons with open charm in the case of charmonium (or open beauty in the case of bottomonium). The cross section for the production of a quarkonium \mathcal{Q} can be written as [15]

$$\sigma_{\mathcal{Q}} = \rho_{\mathcal{Q}} \sigma_{onia}, \quad (4.10)$$

with σ_{onia} the cross section of the $q\bar{q}$ pair described above and $\rho_{\mathcal{Q}}$, which is a non perturbative parameter for a specific quarkonium, describing the probability to project any $q\bar{q}$ state to the specific quarkonium state. It cannot be calculated and can only be determined by fits to data.

Therefore, the CEM cannot provide absolute predictions for quarkonium cross sections. Furthermore, the CEM predicts that any preferred spin alignment is randomized out by the soft interactions with the color field. This results in the prediction of zero polarization for any quarkonium state.

One other crucial prediction of the CEM is that the ratio of two quarkonium states is independent of the kinematic region of the production as well as from the production process, as the parameter $\rho_{\mathcal{Q}}$ is assumed to be universal, for a given quarkonium state. As there have been differences observed, for example in the ratio $\chi_c/J/\psi$ in hadroproduction and photoproduction, the validity of CEM predictions, at least for high energy hadronic colliders, is considered with major doubt [17].

Therefore, the CEM is not considered in the next section, which compares differential cross section measurements to model predictions, discussing the success of the individual models.

4.4.6 Quarkonium Cross Section: Model Predictions and Experimental Results

The CSM was proposed shortly after the discovery of the J/ψ in the early seventies. It was the logical model, considering the understanding at that time. Up to measurements at the Tevatron accelerator in the nineties, there was no indication that CSM predictions were wrong, in that particular formulation in leading order. However, the CDF (*Collider Detector at Fermilab*) measurement of the differential cross section of promptly produced J/ψ 's showed that the CSM prediction underestimated the production by more than

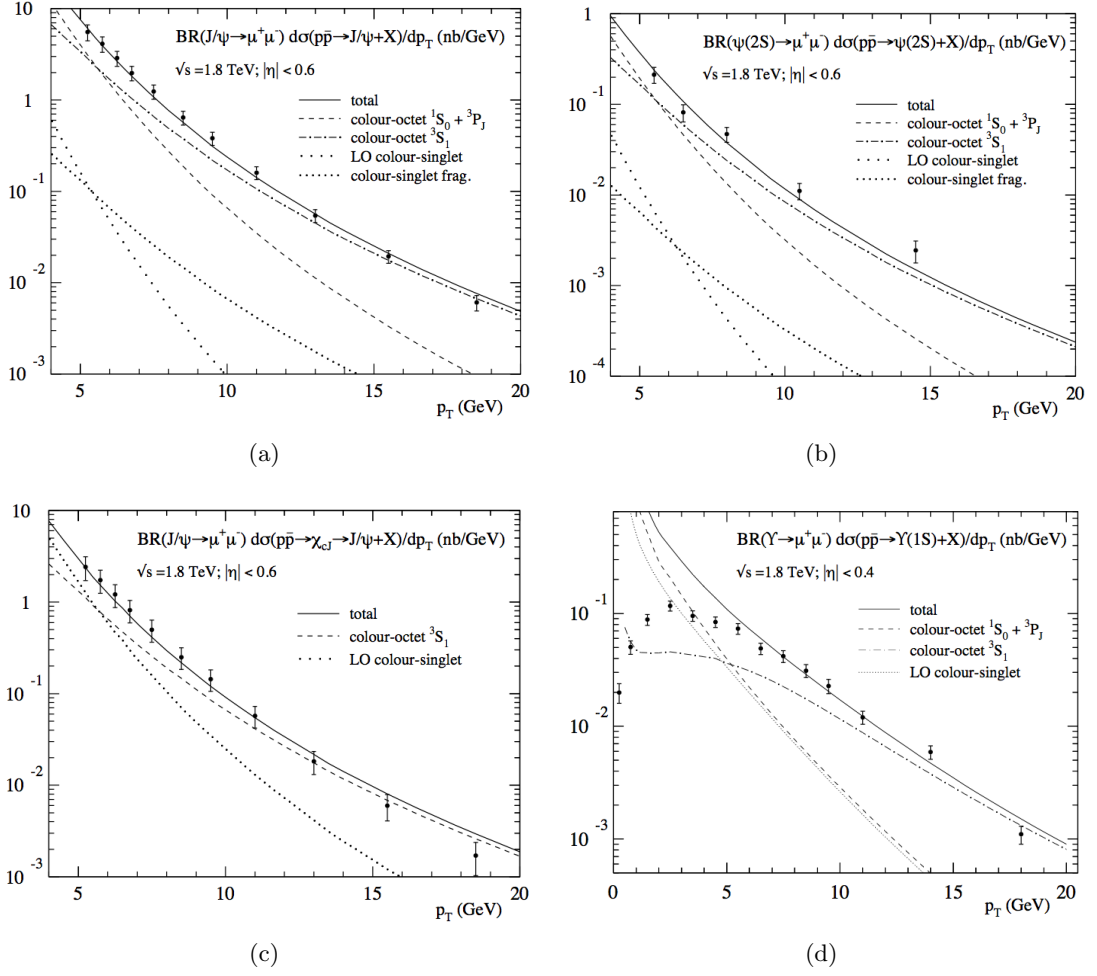


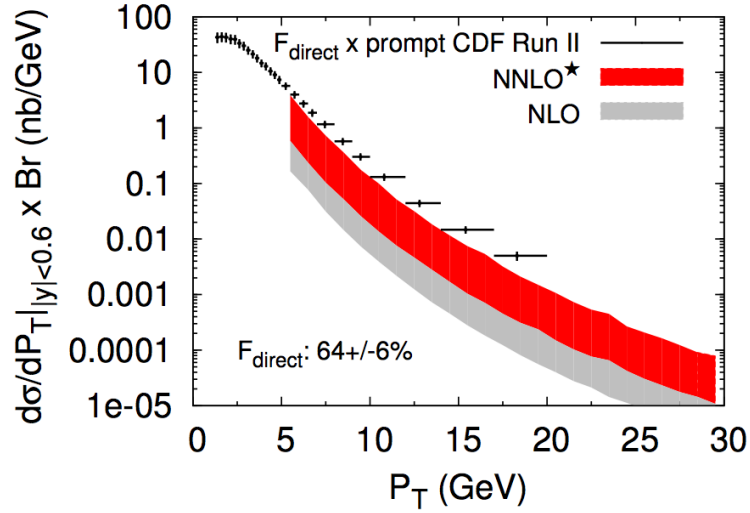
Figure 4.6: CSM LO and COM predictions for the differential cross section $d\sigma/dp_T$ at the Tevatron: Color singlet and color octet contributions to direct quarkonium production in $p\bar{p} \rightarrow Q + X$, compared to CDF results: (a) J/ψ , (b) ψ' , (c) χ_c and (d) $\Upsilon(1S)$ [18].

one order of magnitude (known as the J/ψ *anomaly*). Similarly, the differential cross sections of ψ' , χ_c and $\Upsilon(1S)$ were underestimated by the CSM predictions. This led to new considerations in the quarkonium physics community and to the development of the COM. The idea was that color octet contributions could account for the underestimation of quarkonium production, especially at high p_T .

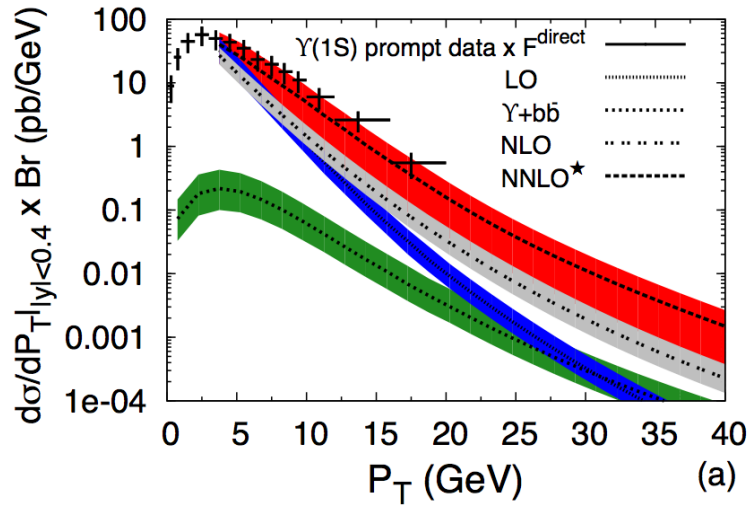
Figure 4.6 shows a comparison of differential cross section measurements at CDF with COM predictions - as the CSM contributions form a part of the COM contributions, those can also be identified. One can see that the COM predictions beautifully describe the shape of the p_T dependence of the quarkonium cross sections. As the COM does not

predict absolute values, but is fit to the data, in terms of letting the long-distance matrix elements float as free parameters, it is not surprising that good results were obtained.

However, the COM predicts transverse polarization of the J/ψ , increasing with p_T , which is in contradiction with what was seen at CDF (detailed discussion in Chap. 6 and Fig. 6.3 (b)). This fact disturbed the common belief in the importance of the color octet contributions.



(a)



(b)

Figure 4.7: CSM predictions for differential cross section $d\sigma/dp_T$ for direct J/ψ production [19] (a) and direct $\Upsilon(1S)$ production [20] (b) with NLO and NNLO* contributions, compared to CDF data.

Higher Order Corrections

Recent calculations of next-to-leading order (NLO) and next-to-NLO (NNLO*) corrections [19] [20] to LO CSM calculations show better agreement with CDF data in terms of differential cross section measurements (Fig. 4.7) and the J/ψ polarization measurement (Fig. 6.4). Although the calculations are characterized by higher orders of α_s (NLO: up to α_s^4 , NNLO*: α_s^5), they result in significant contributions to the quarkonium cross section, and are better able to describe the shape, as different kinematic scalings in p_T ($\frac{1}{p_T^4}$ and $\frac{1}{p_T^6}$ in comparison to $\frac{1}{p_T^8}$ at LO) enhance the yield at high p_T .

Very recent efforts to implement these higher order corrections in COM calculations [21] have led to a better understanding of the long-distance matrix elements and the corresponding color octet contributions. Global fits to J/ψ production data have been conducted. A total of 26 datasets from experiments involving hadroproduction, photoproduction and e^+e^- annihilation in different kinematic regions have been used to extract the universal long-distance matrix elements with great success. Figure 4.8 shows three examples out of the 26 sets of results, comparing J/ψ cross section measurements with datasets from different rapidity regions. The rapidity y of a particle is defined as $y = \frac{1}{2} \ln \frac{E+p_L}{E-p_L}$. Together with p_T and φ it fully defines the kinematic properties of the particle. The numerical value of y is very close to the value of pseudo-rapidity η .

Experimental results on J/ψ polarization and comparisons with model predictions will be described in detail in Chap. 6.

4.5 Quarkonium Production - Summary and Outlook

This section summarizes the current situation of the understanding of quarkonium production and prospects of clarification. After decades of gathering experimental results and developing models to predict observables of quarkonium production that can possibly discriminate between the individual models, the importance of color octet contributions can still not be estimated reasonably. Although CDF measurements indicate that color octet production should contribute significantly, recent higher order CSM predictions show an improvement in the comparison with Tevatron results - without the need of color octet contributions.

The plan for future measurements seems clear, as theorists have communicated well what information is needed to further clarify quarkonium production. Various quarkonium polarization measurements at the LHC experiments can vastly contribute. The detailed list of future measurements in this field will be discussed in Sect. 10.2.

Very recently, theorists have proposed to widen the perspective and added further

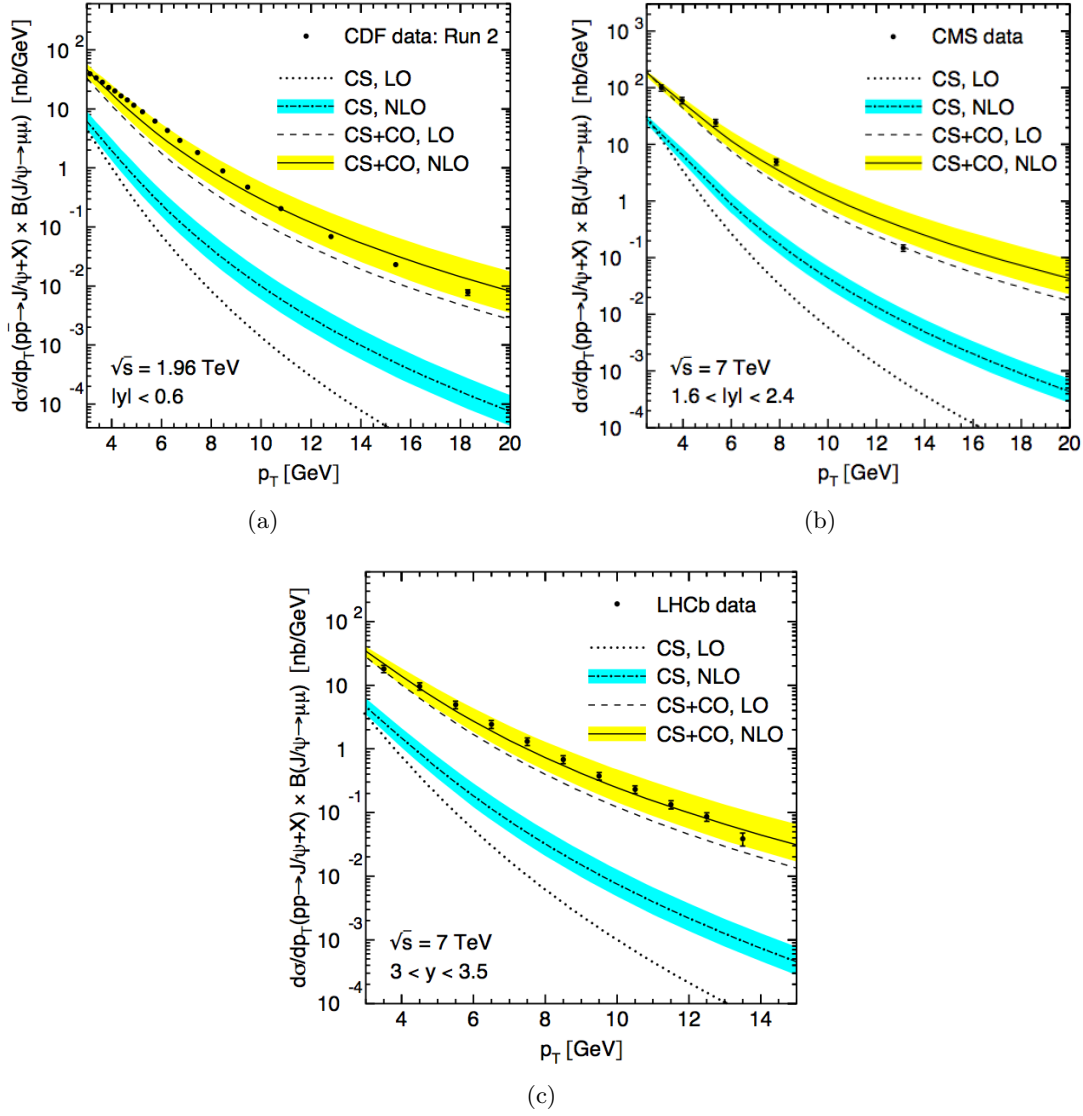


Figure 4.8: Global fits of NLO COM calculations to J/ψ data. Compared to three sets of results from different rapidity regions: (a) CDF, (b) CMS, (c) LHCb [21].

observables to their wish list of measurements to be conducted at the LHC and other experiments, which will help to evaluate the importance of color octet contributions. These considerations [22] involve the evaluation of hadronic activity around the quarkonium, studies of associated production ($J/\psi + c\bar{c}$, $\Upsilon + b\bar{b}$), in particular double J/ψ production, and analyses of other channels such as $J/\psi + \gamma$ and $\Upsilon + \text{Vector Boson}$.

Chapter 5

Quarkonium Polarization

5.1 General Concepts

This section discusses the basics of quarkonium polarization, explaining how specific production mechanisms can lead to a preferred *spin alignment* of the produced particle and describing the observable properties of the decay distributions of quarkonium states.

If a vector particle ($J^{PC} = 1^{--}$) is observed in a state containing as dominant component one of the three eigenstates of the angular momentum component J_z with respect to a certain quantization axis z , we call the particle polarized. Unpolarized particles are equal mixtures of $J_z = -1, 0$ and $+1$ eigenstates. Preferred spin alignments are caused by basic conservation laws and symmetries of the electroweak and strong interactions [23].

In the following, illustrative cases of elementary production mechanisms of vector quarkonia (J/ψ , ψ' and the $\Upsilon(nS)$ states), leading to specific polarizations, are discussed.

Vector quarkonia, having the same charge-parity quantum numbers of a photon, can be produced in $e^+ - e^-$ annihilation via an intermediate photon. Figure 5.1 (a) shows the corresponding leading order production diagram. Simple arguments show that this process leads to a preferred spin alignment, corresponding to the exclusive presence of the eigenstates $J_z = +1$ and $J_z = -1$ (and the absence of the $J_z = 0$ one) with respect to the direction of the colliding particles (the z axis of the *Collins-Soper (CS) frame*, Sect. 5.2). In fact, it is a general property of QED, in the limit of zero fermion masses, that the sum of the projections of the fermion spins over the respective momenta (helicities) is a conserved quantity. As the intermediate photon has zero helicity, the colliding leptons must have opposite helicities. This means that, having opposite momenta, they must have parallel spins. Because of angular momentum conservation, the produced quarkonium has, therefore, angular momentum projection $J_z = \pm 1$.

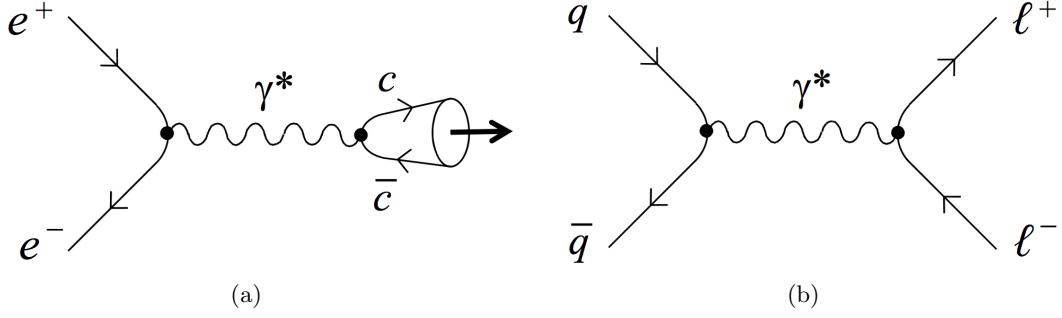


Figure 5.1: Leading order diagrams for vector quarkonium production in electron-positron annihilation (a) and for Drell-Yan production in quark-antiquark annihilation (b) [23].

For the same fundamental law, applied to quark-antiquark collisions (in the limit of zero quark masses), also Drell-Yan production is expected to show this kind of spin alignment. The leading order Drell-Yan production diagram is shown in Fig. 5.1 (b). The quark-antiquark system is produced in the eigenstates $J_z = \pm 1$ with respect to the direction of the beam (CS axis).

Gluon fragmentation will be the dominant process in high p_T quarkonium production in hadron collisions [24]. The LHC experiments, and in particular CMS, will be able to test this prediction up to very high p_T values. The fragmenting gluon should have helicity ± 1 and would transfer this property to the final state, predicted by NRQCD to be dominated by the color octet component $c\bar{c}[{}^3S_1^{(8)}]$. The diagram of this process was already shown in Fig. 4.5 (b). During the non perturbative transition into the color neutral physical quarkonium state via soft gluon emission, the helicity properties of the color octet state are transferred to the bound meson. These considerations result in the prediction of a dominant $J_z = \pm 1$ component for the produced vector quarkonium, in this case not along the direction of the colliding beams, but along the flight direction of the quarkonium (the *helicity (HX) axis*, Sect. 5.2).

5.2 The Polarization Reference Frame

5.2.1 Definition of the Reference Frame

As will be shown in Sect. 5.3, different polarization states are characterized by different shapes of the angular distribution of the decay products. The decay distribution is measured with respect to a certain system of coordinates defined in the rest frame of the quarkonium. A spherically symmetric distribution means that the produced state

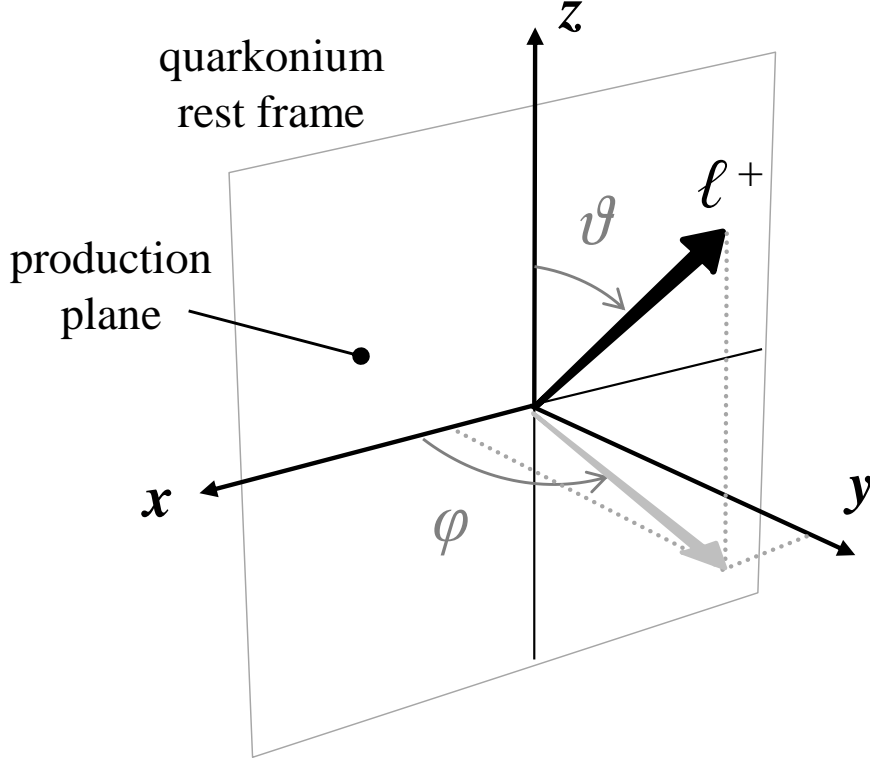


Figure 5.2: Definition of the polarization frame in the quarkonium rest frame. The quantization axis z is chosen in the production plane, containing the momenta of the colliding beams, according to one of several possible conventions [23].

is, on average, unpolarized, while an anisotropy of the distribution reflects a polarized state. In the case of the two body decay $J/\psi \rightarrow \mu^+ \mu^-$, the angular configuration of the decay is univocally defined by the direction of one of the decay products (in case of the present analysis the direction of the μ^+) with respect to a chosen reference frame.

The production process defines univocally a plane (the production plane), which, in the quarkonium rest frame, coincides with the plane formed by the two colliding beams. The y axis is taken as perpendicular to the production plane.

The quantization axis, z , can be chosen in the production plane according to one of several conventions. The (infinite) possible definitions of the reference frame differ only by a rotation about the y axis. Figure 5.2 shows the definition of the spherical coordinates - the polar angle ϑ and the azimuthal angle φ .

Published measurements have used basically three conventions for the quantization axis z , chosen on the basis of different physical motivations (Sect. 5.1). These definitions are shown in Fig. 5.3 and listed here:

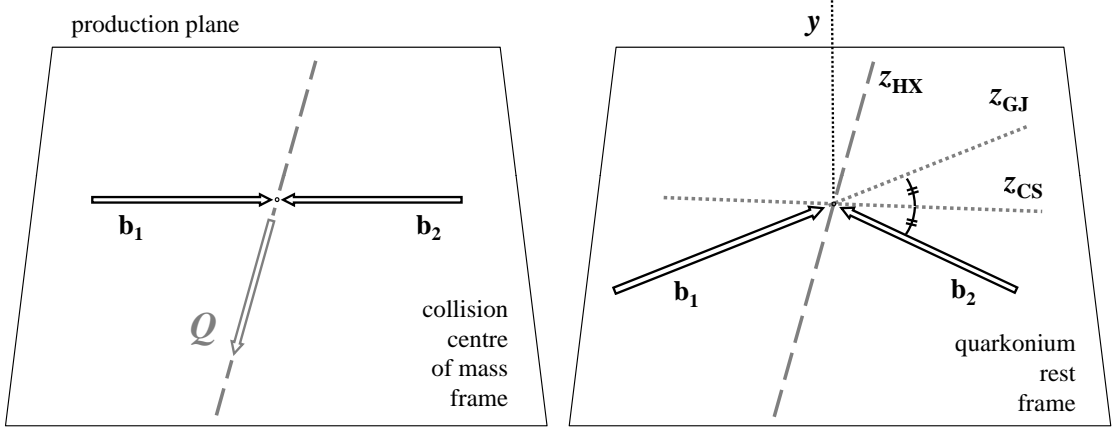


Figure 5.3: Definition of three reference frames (HX, GJ, CS) with respect to the momenta of the colliding beams (b_1 , b_2) and the momentum of the quarkonium Q [23].

- *Helicity frame (HX)*: The HX axis is aligned with the flight direction of the decaying quarkonium, as seen in the center of mass system of the colliding beams.
- *Gottfried Jackson frame (GJ)*: The GJ axis is defined as the direction of the momentum of one of the two colliding beams.
- *Collins-Soper frame (CS)*: The CS axis is defined as the bisector of the angle formed by the momentum of one colliding beam with respect to the opposite direction of the momentum of the other beam.

In this analysis, only the CS and HX frames are considered. In the limit of high p_T and low longitudinal momentum p_L ($p_T \gg |p_L|$) they represent two orthogonal choices (differing by a rotation of 90° about the y axis). In the limit of zero p_T , the three frame definitions coincide.

5.2.2 Conventions

The measurement of the angular distribution of the decay products is a measurement of the average spin alignment of the decaying particle. In analogy with the photon, we say that the quarkonium is produced *transversely* polarized if the preferred projection of the angular momentum J_z on the chosen quantization axis z is ± 1 . If the projection of the angular momentum is $J_z = 0$, we say that the quarkonium is *longitudinally* polarized.

5.3 Dilepton Decay Angular Distribution

This section examines the relation between the shape of the angular distribution of the dilepton decay of any vector quarkonium and its polarization. The calculation of the angular distribution will only be sketched. The full derivation can be found in Ref. [23]. All calculations and considerations apply to any vector quarkonium, although in this section only the J/ψ meson is mentioned explicitly.

Starting point for the following considerations is a process which produces the J/ψ as a superposition of the three possible eigenstates $J_z = 0$ and ± 1 , with respect to the chosen polarization axis z ,

$$|V\rangle = b_{+1} | +1 \rangle + b_{-1} | -1 \rangle + b_0 | 0 \rangle . \quad (5.1)$$

The conventions for axes, angles and angular momentum states are shown in Fig. 5.4. Because of helicity conservation at the photon-dilepton vertex in the decay $J/\psi \rightarrow \ell^+ \ell^-$, the angular momentum projection of the dilepton system $J_{z'}$, can only be $l' = \pm 1$. By a rotation $R(\varphi, \vartheta, -\varphi)$ of the axis z into the axis z' , this state can now be written as a superposition of eigenstates of J_z , corresponding to $l = 0$ and ± 1 , through the rotation

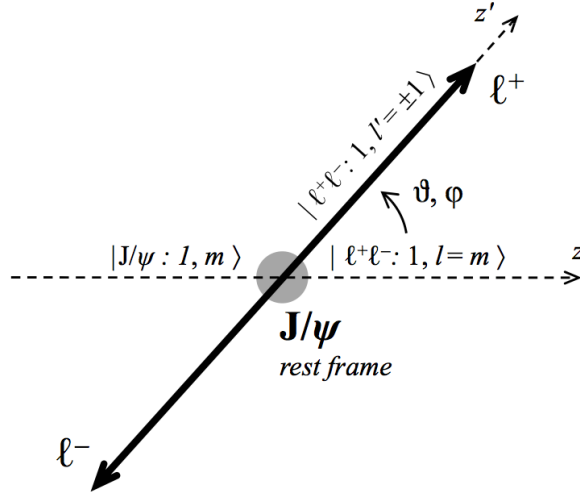


Figure 5.4: $J/\psi \rightarrow \ell^+ \ell^-$ decay: notations of axes, angles and angular momentum states [23].

transformation

$$|J, M'\rangle = \sum_{M=-J}^{+J} \mathcal{D}_{MM'}^J(\vartheta, \varphi) |J, M\rangle, \quad (5.2)$$

depending on the complex rotation matrix elements $\mathcal{D}_{MM'}^J(\vartheta, \varphi)$.

After calculating the amplitude for the partial process $J/\psi(m) \rightarrow \ell^+ \ell^- (l')$, squaring the amplitude and summing over the spin alignments $l' = \pm 1$ of the dilepton system, one obtains the expression of the angular distribution of the positive lepton,

$$\begin{aligned} W(\cos \vartheta, \varphi) \propto \frac{\mathcal{N}}{(3 + \lambda_\vartheta)} & (1 + \lambda_\vartheta \cos^2 \vartheta + \lambda_\varphi \sin^2 \vartheta \cos 2\varphi + \lambda_{\vartheta\varphi} \sin 2\vartheta \cos \varphi \\ & + \lambda_\varphi^\perp \sin^2 \vartheta \sin 2\varphi + \lambda_{\vartheta\varphi}^\perp \sin 2\vartheta \sin \varphi), \end{aligned} \quad (5.3)$$

with $\mathcal{N}, \lambda_\vartheta, \lambda_\varphi, \lambda_{\vartheta\varphi}, \lambda_\varphi^\perp$ and $\lambda_{\vartheta\varphi}^\perp$ defined by different combinations of the initial amplitudes of the individual angular momentum projection eigenstates of the J/ψ (Eq. 5.1 and [23]). The λ_X parameters, determining the shape of the angular distribution, will be referred to as *polarization parameters*.

The presence of the last two terms in Eq. 5.3 accounts for a possible asymmetry of the distribution with respect to the production plane. This asymmetry, however, vanishes on average and these two terms have to be dropped.

These considerations are valid for a single production process. When n production processes with resulting angular distributions $W^{(i)}(\cos \vartheta, \varphi)$ and weights $f^{(i)}$ contribute to the inclusive production of the J/ψ , we can write the observable angular distribution as

$$\begin{aligned} W(\cos \vartheta, \varphi) &= \sum_{i=1}^n f^{(i)} W^{(i)}(\cos \vartheta, \varphi) \\ &\propto \frac{1}{(3 + \lambda_\vartheta)} (1 + \lambda_\vartheta \cos^2 \vartheta + \lambda_\varphi \sin^2 \vartheta \cos 2\varphi + \lambda_{\vartheta\varphi} \sin 2\vartheta \cos \varphi). \end{aligned} \quad (5.4)$$

Eq. 5.4 represents the most general observable decay angular distribution of a vector quarkonium decaying into two leptons. Its functional form is equivalent to Eq. 5.3. However, each of the resulting polarization parameters λ_X , describing the shape of the distribution determined by the sum of all production processes, is a weighted average of

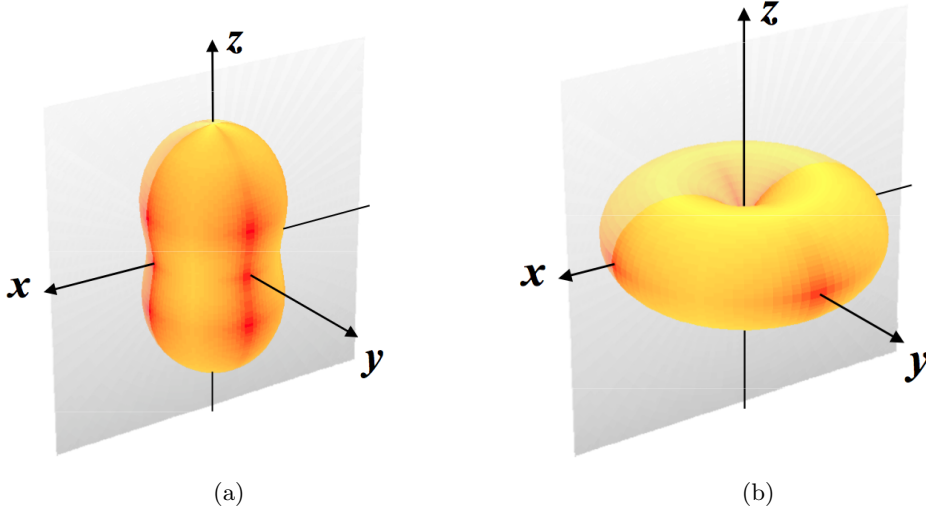


Figure 5.5: Visualization of the angular decay distribution of transversely polarized (a) and longitudinally polarized J/ψ 's (b) [23].

the polarization parameters $\lambda_X^{(i)}$ characterizing the individual elementary processes,

$$\lambda_X = \frac{\sum_{i=1}^n \frac{f^{(i)} \mathcal{N}^{(i)}}{(3 + \lambda_\vartheta^{(i)})} \lambda_X^{(i)}}{\sum_{i=1}^n \frac{f^{(i)} \mathcal{N}^{(i)}}{(3 + \lambda_\vartheta^{(i)})}}. \quad (5.5)$$

Figure 5.5 shows a graphical representation of the dilepton decay distributions for two extreme cases: fully transverse ($\lambda_\vartheta = 1, \lambda_\varphi = \lambda_{\vartheta\varphi} = 0$) and fully longitudinal polarization ($\lambda_\vartheta = -1, \lambda_\varphi = \lambda_{\vartheta\varphi} = 0$). The distance of the surface from the point of origin is proportional to the probability that the positive lepton decays in that direction. In the case of transverse polarization, the leptons tend to decay in the direction of the quantization axis; in the case of longitudinal polarization, the leptons tend to decay in the perpendicular direction.

The decay distribution of an unpolarized state would be represented by a sphere. At this point it should be mentioned that it is impossible to choose the amplitudes of the angular momentum states in Eq. 5.1 so that the resulting state is unpolarized [23]. Hence, a $J = 1$ meson produced exclusively in a single elementary production process can never be unpolarized. An inclusive measurement of vector quarkonium can only result in zero polarization if the state is produced in a mixture of production processes and the polarizations corresponding to the different subprocesses combine to zero, according to Eq. 5.5. Therefore, polarization is an intrinsic property of vector quarkonia.

5.4 Measurement Dependence on the Reference Frame

5.4.1 Transformation of Polarization Parameters into Different Frames

As any two polarization reference frames only differ by the chosen direction of the quantization axis z in the production plane, one can easily calculate the dependence of the polarization parameters on this choice, by performing a rotation about the y axis by the angle δ . After applying this rotation to Eq. 5.4, one obtains the angular distribution in the rotated frame,

$$W(\cos \vartheta', \varphi') \propto \frac{1}{(3 + \lambda'_{\vartheta})} (1 + \lambda'_{\vartheta} \cos^2 \vartheta' + \lambda'_{\varphi} \sin^2 \vartheta' \cos 2\varphi' + \lambda'_{\vartheta\varphi} \sin 2\vartheta' \cos \varphi'), \quad (5.6)$$

with the new polarization parameters λ'_X , given by

$$\lambda'_{\vartheta} = \frac{\lambda_{\vartheta} - 3\Lambda}{1 + \Lambda}, \quad \lambda'_{\varphi} = \frac{\lambda_{\varphi} + \Lambda}{1 + \Lambda}, \quad \lambda'_{\vartheta\varphi} = \frac{\lambda_{\vartheta\varphi} \cos 2\delta - \frac{1}{2}(\lambda_{\vartheta} - \lambda_{\varphi}) \sin 2\delta}{1 + \Lambda}, \quad (5.7)$$

with

$$\Lambda = \frac{1}{2}(\lambda_{\vartheta} - \lambda_{\varphi}) \sin^2 \delta - \frac{1}{2}\lambda_{\vartheta\varphi} \sin 2\delta. \quad (5.8)$$

The effect of this transformation can be appreciated by considering, for example, what a fully transverse polarization (Fig. 5.5 (a)) looks like when it is measured with respect to an axis z' rotated by $\delta = 90^\circ$ with respect to the axis z (Fig. 5.6 (a)). This situation is relevant in the case of the comparison between CS and HX frames in the limit $p_T \gg p_L$, where the CS frame is perpendicular to the HX frame. With respect to z one measures *fully transverse polarization*, given by a *polar anisotropy* $\lambda_{\vartheta} = +1$ and no *azimuthal anisotropy* ($\lambda_{\varphi} = \lambda_{\vartheta\varphi} = 0$). With respect to z' one measures a partially longitudinal polarization, $\lambda'_{\vartheta} = -\frac{1}{3}$ and a significant azimuthal anisotropy $\lambda'_{\varphi} = \frac{1}{3}, \lambda'_{\vartheta\varphi} = 0$.

As a further example, if the polarization is fully longitudinal with respect to z ($\lambda_{\vartheta} = -1, \lambda_{\varphi} = \lambda_{\vartheta\varphi} = 0$, Fig. 5.5 (b)), with respect to z' one observes a full transverse polarization $\lambda'_{\vartheta} = +1$ with maximal azimuthal anisotropy $\lambda'_{\varphi} = -1, \lambda'_{\vartheta\varphi} = 0$ (Fig. 5.6 (b)).

In conclusion, if one integrates over φ , and only measures the polar anisotropy, as has been the case in most previous analysis, the physically very different cases shown in Fig 5.5 (a) and Fig. 5.6 (b) are indistinguishable. These considerations anticipate the discussion in Sect. 5.5, where the formalism of frame-independent polarization parameters will be introduced.

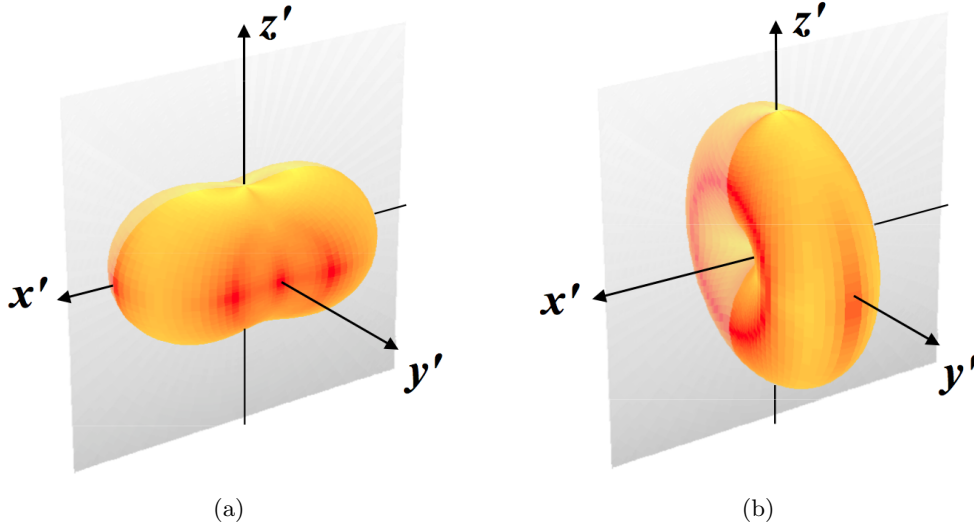


Figure 5.6: Visualization of the angular decay distribution of transversely polarized (a) and longitudinally polarized J/ψ 's (b), measured in a frame rotated by 90° with respect to the frame where the polarization is naturally induced [23].

5.4.2 Kinematic Dependence of the Polarization Parameters

The polarization of any vector quarkonium is in general expected to show a dependence of p_T and rapidity (y), as different mixtures of production processes are expected to contribute, depending on the kinematics of the production. This kinematic dependence is here called *intrinsic*.

In Sect. 5.4.1 it was shown that the measured polarization depends on the orientation of the reference frame. As the definitions of the CS and HX axes depend on the production kinematics, the angle $\delta_{HX \rightarrow CS}$, describing the rotation of the HX frame into the CS frame, also depends on the kinematics. Therefore, if a constant polarization is measured in one of the two frames, a significantly kinematic-dependent polarization is measured in the other frame. This kind of kinematic dependence is here denoted as *extrinsic*. A strong, extrinsic kinematic dependence can be originated by an unfortunate choice of the quantization axis. Such an extrinsic kinematic dependence can be distinguished from a true (intrinsic) physical dependence of the polarization by performing the measurement in at least two different frames.

A few simple calculations [23] lead to the expression

$$\delta_{HX \rightarrow CS} = -\delta_{CS \rightarrow HX} = \arccos \frac{p_L m}{p \sqrt{m^2 + p_T^2}}. \quad (5.9)$$

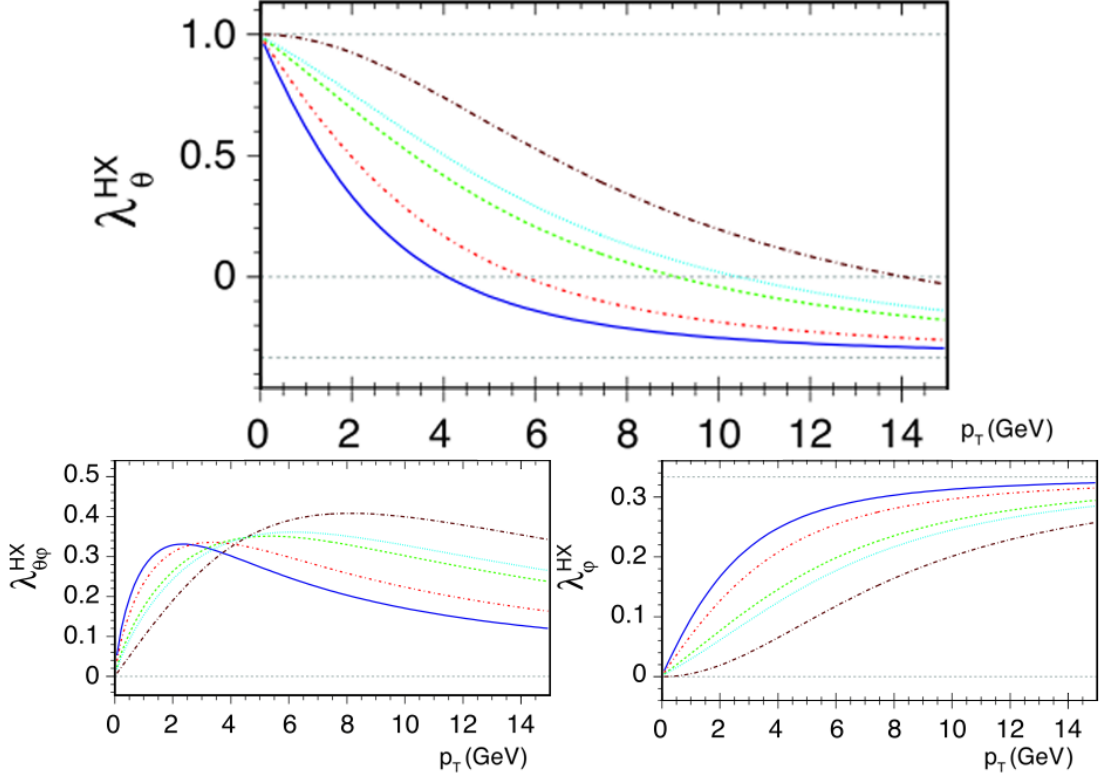


Figure 5.7: Kinematic dependence of the polarization parameters of J/ψ mesons with full transverse polarization in the CS frame ($\lambda_\theta^{CS} = +1$), as measured in the HX frame. The individual curves represent different rapidity intervals; starting from the solid line: $|y| < 0.6$ (CDF), $|y| < 0.9$ (ALICE), $|y| < 1.8$ (D0), $|y| < 2.5$ (ATLAS and CMS), $2 < y < 5$ (LHCb) [25].

The angle $\delta_{HX \rightarrow CS}$ reaches 90° , as discussed before, in the limit $p_T \gg p_L$ and vanishes in the opposite limit.

If one assumes a fully transverse polarization in the CS frame, with no intrinsic kinematic dependence, using this formula one finds that a strong extrinsic kinematic dependence must be measured in the HX frame. Figure 5.7 shows this extrinsic dependence in the p_T region of $0 - 15$ GeV for different rapidity regions.

5.4.3 Positivity Constraints

From the condition that the polar anisotropy λ_θ is always included between -1 and $+1$ in any possible frame it is possible to derive constraints on the three polarization parameters, called *positivity constraints* [26, 23]:

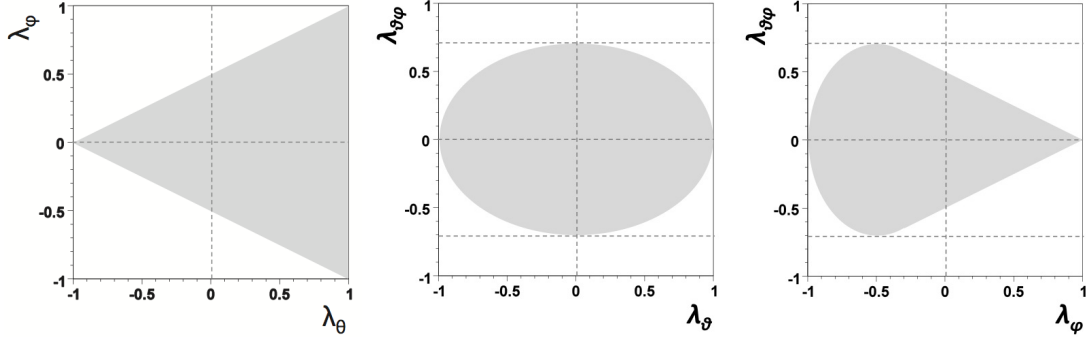


Figure 5.8: Allowed phase space regions for the polarization parameters due to positivity constraints [23, 26].

$$\begin{aligned}
 |\lambda_\varphi| \leq \frac{1}{2}(1 + \lambda_\vartheta), \quad \lambda_\vartheta^2 + 2\lambda_{\vartheta\varphi}^2 \leq 1, \quad |\lambda_{\vartheta\varphi}| \leq \frac{1}{2}(1 - \lambda_\varphi), \\
 (1 + 2\lambda_\varphi)^2 + 2\lambda_{\vartheta\varphi}^2 \leq 1 \quad \text{for} \quad \lambda_\varphi < -\frac{1}{3}.
 \end{aligned} \tag{5.10}$$

The allowed phase space regions for the polarization parameters, due to these constraints, are visualized in Fig. 5.8.

5.5 A Frame-Invariant Approach

Recent developments in the formalism for the description of the dilepton decay distributions of vector particles promise to lead to a better understanding of the polarization properties of quarkonia and of their physical interpretation. A crucial aspect of this new formalism is the *frame-invariant approach*.

Quarkonium production at the LHC is expected to be the result of several contributions of individual production processes (i) characterized by different polarizations, possibly with respect to different axes. Especially in these conditions, the frame-invariant approach is a useful tool for the description of polarization measurements and calculations. The existence of a frame-invariant quantity is implied by Eq. 5.7 [23], together with two propositions, describing general angular momentum properties of a vector state [27]:

- All combinations $b_{+1}^{(i)} + b_{-1}^{(i)}$ of the amplitudes defined in Eq. 5.1 are invariant by rotation about the y axis.
- For each single subprocess it is always possible to find one axis, $z^{(i)*}$, with respect to which the amplitude $b_0^{(i)*}$ vanishes.

The invariant quantities can be defined as

$$\mathcal{F}_{\{c_i\}} = \frac{(3 + \lambda_\vartheta) + c_1(1 - \lambda_\varphi)}{c_2(3 + \lambda_\vartheta) + c_3(1 - \lambda_\varphi)}, \quad (5.11)$$

for any chosen values of c_1, c_2, c_3 . This equation defines a family of equivalent forms for the frame-invariant parameter as a function of the frame-dependent anisotropy parameters λ_ϑ and λ_φ . The frame-invariant parameter does not depend on the specific quantization axis chosen for the measurement.

The analysis reported in this thesis considers the specific definition obtained with the combination $\{c_1, c_2, c_3\} = \{-3, 0, 1\}$:

$$\mathcal{F}_{\{-3,0,1\}} = \tilde{\lambda} = \frac{\lambda_\vartheta + 3\lambda_\varphi}{1 - \lambda_\varphi}. \quad (5.12)$$

This specific form of the invariant anisotropy parameter has the property that it results in $+1$ (-1) for any combination of fully transversely (longitudinally) polarized J/ψ 's, independently of the reference frame where the particles are fully polarized. If, for example, 60% of the J/ψ 's are produced transversely polarized in the CS frame and 40% are produced transversely polarized in the HX frame, a measurement made in any possible reference frame will lead to $\tilde{\lambda} = +1$.

Furthermore, $\tilde{\lambda}$ is free of extrinsic kinematic dependencies. In the hypothetical polarization scenario just mentioned, intrinsically independent of the production kinematics, every measurement in any kinematic region will lead to $\tilde{\lambda} = +1$. A kinematic dependence as the one shown in Fig. 5.7 can be identified easily as extrinsic by making use of the invariant formalism.

In general, the frame-invariant quantities describe the shape of the dilepton decay distribution independently of the reference frame. However, only the frame-dependent polarization parameters contain the information about the specific frame in which the polarization is naturally induced. Hence, a full understanding of the polarization properties of vector quarkonia can only be obtained by combining information from frame-invariant and frame-dependent parameters.

From an experimentalist's point of view, the frame-invariant approach provides an effective tool to detect unaccounted systematic effects. If measurements of J/ψ polarization are made in two different frames, a comparison between the measurements of the parameter $\tilde{\lambda}$ in the two frames can indicate the presence of unaccounted systematic effects, if the two results are not compatible. As the CS frame and the HX frame become orthogonal in the limit of high p_T , they represent a natural choice for this test.

5.6 Influence of Feed-Down Contributions from Heavier Charmonium States

A large fraction of J/ψ 's produced in hadronic collisions originates from the decay of heavier charmonium states, ψ' and χ_c . This contribution belongs, together with the directly produced J/ψ 's, to the so-called *prompt* component of the J/ψ data sample. The fractional contribution of the feed-down sources in proton-proton collisions has been estimated in a global average of the available proton-nucleus data [28]. The feed-down fractions (referred to the prompt sample) are, respectively, $8.1 \pm 0.3\%$ and $25 \pm 5\%$ for J/ψ 's coming from ψ' and χ_c decays. About 67% of the prompt J/ψ 's are directly produced.

Additionally, there are significant feed-down contributions from decays of b hadrons: B^+ , B_s , B^0 and Λ_b . J/ψ events from these decays can be separated from the prompt events very efficiently, thanks to the fact that b hadrons decay to J/ψ 's with lifetimes of the order of 10^{-12} s, well measurable with the CMS detector. This is the reason why this contribution is referred to as the *non-prompt* component of the J/ψ data sample. The separation will be described in detail in Sect. 7.5.2.

The feed-down contribution due to the decays from heavier charmonium states is not separated in the analysis reported in this thesis. Therefore, it is important to mention that the unknown polarization of the J/ψ 's from χ_c decays represents a significant contamination to the polarization of the directly produced J/ψ 's. In fact, the χ_c states have different parity and angular momentum properties with respect to the J/ψ . Moreover, the production of the χ_c states is based on different partonic processes with respect to the production of direct J/ψ 's. These facts strongly suggest that the polarization properties of J/ψ 's originating from χ_c feed-down may be very different from those of the direct J/ψ 's [29].

The contribution of feed-down from χ_{c0} decays is irrelevant, as the branching fraction $\chi_{c0} \rightarrow J/\psi \gamma$ is only $\sim 1\%$ [14]. The χ_{c1} (branching fraction $\chi_{c1} \rightarrow J/\psi \gamma \sim 34\%$ [14]) is a $J = 1$ meson, with possible angular momentum projections $J_z = 0, \pm 1$. The χ_{c2} (branching fraction $\chi_{c1} \rightarrow J/\psi \gamma \sim 19\%$ [14]) is a $J = 2$ state, with possible projections $J_z = 0, \pm 1$ and ± 2 . Figure 5.9 shows the possible influence of the χ_c feed-down on the measurement of the polarization of prompt J/ψ 's, when the directly produced J/ψ 's are fully transversely polarized ($\lambda_\theta = 1$). Depending on the total fraction $R(\chi)$ of the χ_c feed-down, on the relative contribution χ_{c1}/χ_{c2} and on the χ_c polarization properties, the resulting λ_θ can be strongly reduced with respect to the full polarization characterizing the directly produced J/ψ 's.

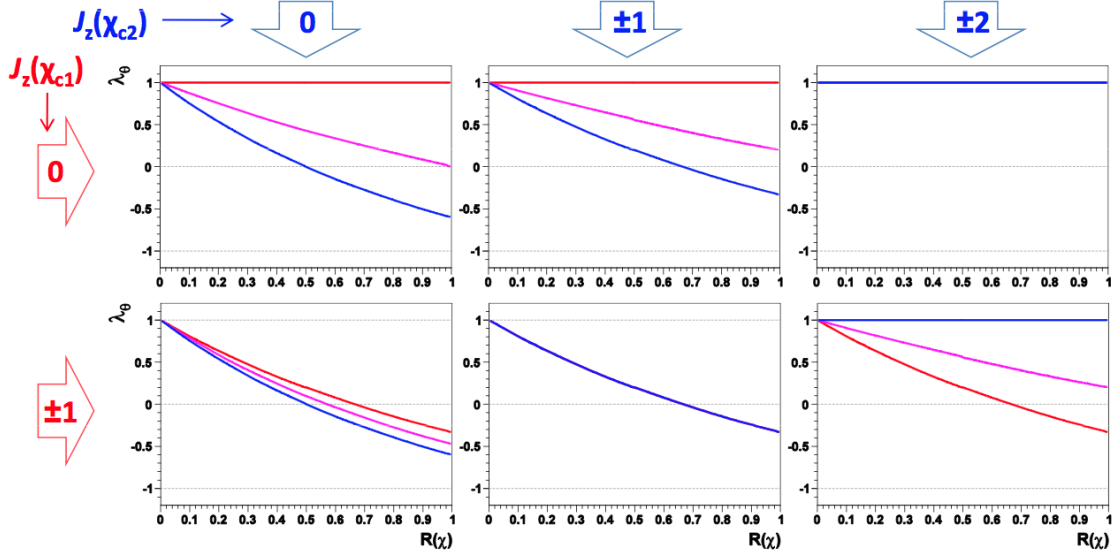


Figure 5.9: Effect of the χ_c feed-down contribution on the measurement of J/ψ polarization, when the directly produced J/ψ 's are fully transversely polarized. The observable prompt polarization is represented as a function of the total χ feed-down fraction $R(\chi)$, of the relative contribution of the two χ states and of the χ polarization states, $J_z(\chi_{c1})$ and $J_z(\chi_{c2})$. Red (and blue) curves: J/ψ 's from χ_{c1} dominate over J/ψ 's from χ_{c2} (and vice-versa). Magenta: the two contributions are equal [30].

5.7 Summary: Final Considerations on the Measurement of Quarkonium Polarization

The polarization of a vector quarkonium is measured by determining the anisotropy of the angular distribution of the decay products in the quarkonium rest frame. This anisotropy reflects the preferred spin alignment of the produced quarkonium, which originates from basic conservation laws and from the specific properties of the underlying production mechanisms. Therefore, polarization contains detailed information about the elementary production processes. The experimental determination of quarkonium polarization in the LHC experiments will certainly contribute to a better understanding of quarkonium production.

A further experimental motivation for quarkonium polarization measurements is the fact that quarkonium cross section analyses are affected by a systematic uncertainty of 20% or more due to the unknown polarization properties.

Polarization is an intrinsic property of vector quarkonia, given that it is impossible, for a single subprocess, to produce unpolarized quarkonia. Polarization is, therefore, a crucial aspect of quarkonium production, which demands the most careful study from

both the experimental and the theoretical point of view.

Since polarization is a direct consequence of the properties of the underlying production processes, feed-down contributions have to be carefully considered. The feed-down contributions from b-hadron decays have to be separated and the contributions from heavier charmonium states have to be taken into account when interpreting the physics results.

A new approach to quarkonium polarization measurements has been recently developed [23], which can lead to a better understanding of the angular momentum properties of vector quarkonia. The key aspects of this approach are:

- The decay angular distribution has to be measured in all its degrees of freedom, including the terms of polar and azimuthal anisotropy. In fact, the measurement of the polar anisotropy alone leads, in general, to ambiguous results.
- The polarization should be measured in at least two different reference frames, in order to distinguish between intrinsic and extrinsic kinematic dependencies.
- A new, frame-independent formulation of the polarization measurement has been proposed. The measurement of the frame-independent polarization parameter can provide clearer and more significant information on the intrinsic quality of the polarization (transverse or longitudinal) in the presence of the superposition of several production processes. Moreover, it can also be used to perform efficient experimental cross checks.
- The frame-dependent and the frame-independent approaches are complementary and should be used in parallel. In fact, while the frame-invariant approach provides the cleanest indication of the intrinsic nature of the polarization, only the measurement of the full angular distribution (in its frame-independent form) provides the information on what is the direction along which the polarization is induced.

Chapter 6

Experimental Situation of J/ψ Polarization

This section gives an overview of existing measurements of J/ψ polarization in hadronic collisions. Several measurements have been made in different experimental setups and different kinematic regions, using various approaches. The majority of the analyses, including the only existing measurement at collider energies, by CDF, determined the polar angle distribution ignoring possible azimuthal anisotropies and their results present, therefore, serious ambiguities of interpretation. It will be shown that several possible polarization scenarios, characterized by very different values of the azimuthal anisotropy and of the frame-invariant parameters, are compatible with the CDF measurement of the polar anisotropy. Furthermore, expectations for the J/ψ polarization measurement at CMS will be discussed, including a study of the potential of discrimination among those scenarios offered by the CMS data.

6.1 Survey of Existing J/ψ Polarization Measurements

6.1.1 Fixed Target Experiments

The Fermilab experiment *E866* measured the J/ψ polarization in terms of the polar anisotropy parameter λ_θ , in the CS frame. The experimental setup was a proton beam of 800 GeV energy interacting with a copper target. The analysis was made in the dimuon decay channel, $J/\psi \rightarrow \mu^+\mu^-$. The results were presented in intervals of the Feynman-variable $x_F = \frac{2p_L}{\sqrt{s}}$ and of p_T . Figure 6.1 shows the p_T dependence of the results, which are compatible with zero polarization in the whole probed kinematic region, within systematic errors [31].

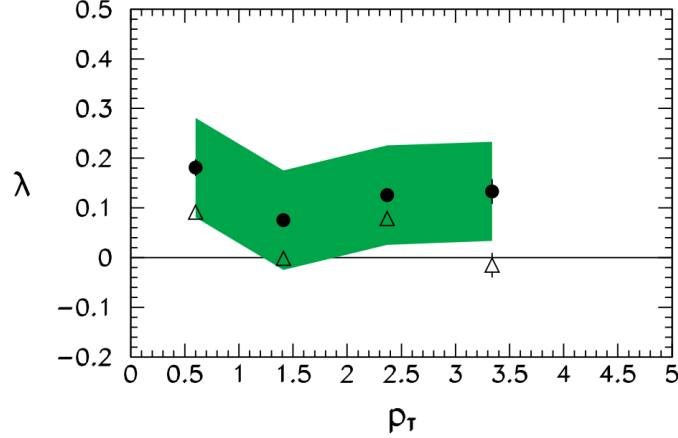


Figure 6.1: The J/ψ polarization parameter $\lambda(=\lambda_\vartheta)$ measured by E866 versus p_T and for two x_F ranges: $x_F < 0.45$ (solid circles) and $x_F > 0.45$ (open triangles). Systematic uncertainties are represented by the green band [31].

The DESY experiment *HERA-B* has measured the full angular decay distribution, determining the azimuthal anisotropy parameters λ_φ and $\lambda_{\vartheta\varphi}$ in addition to λ_ϑ . Two experimental setups were considered: a proton beam interacting with a carbon target and a proton beam interacting with a tungsten target, in both cases at a center of mass energy of $\sqrt{s} = 41.6$ GeV [32]. The analysis included both dilepton decay channels $J/\psi \rightarrow e^+e^-$ and $J/\psi \rightarrow \mu^+\mu^-$ and was performed in the CS, HX and GJ frames. The results were presented as a function of x_F and p_T , individually for the two decay channels, the two target materials, and as combined results (Fig. 6.2). The results of the individual frames show the same trends in all parameters, but are quantitatively clearly different. As HERA-B probed a kinematic region where the definitions of the three frames almost coincide (the limit of low p_T), a strong frame dependence was neither expected nor seen. Summarizing the results, the measurement indicates $\lambda_\vartheta < 0$ with $\lambda_\vartheta^{CS} < \lambda_\vartheta^{GJ} < \lambda_\vartheta^{HX}$, corresponding to a longitudinal polar anisotropy, decreasing with p_T . At the same time the results indicate an azimuthal anisotropy ($\lambda_\varphi < 0$) increasing with p_T . The measurement of λ_φ^{CS} is compatible with 0 in the full considered kinematic region (this is relevant for the discussion of the scenario 2 considered below).

6.1.2 Collider Experiments

In 2000 the Tevatron experiment CDF published results of prompt J/ψ polarization in the HX frame, after subtracting the non-prompt component originating from the decay of beauty hadrons. The experiment studied the dimuon decay of J/ψ 's produced

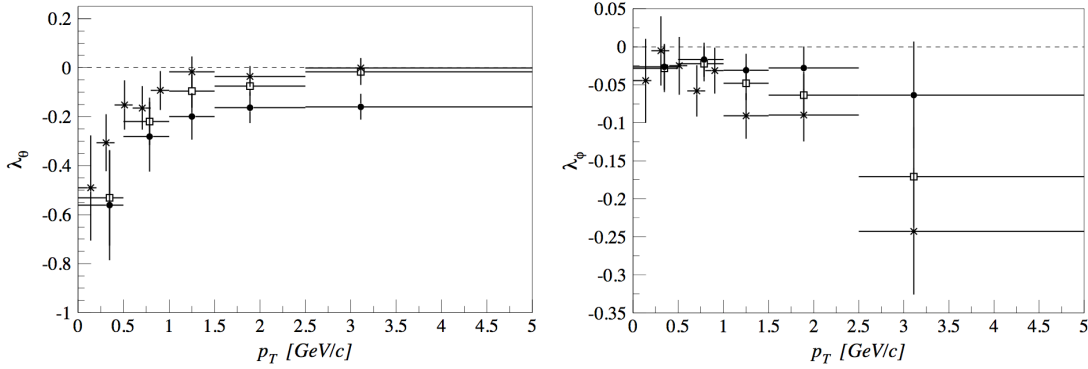


Figure 6.2: p_T dependence of the J/ψ polarization parameters measured by HERA-B, CS, GJ and HX results are represented by the black circles, white squares and asterisks, respectively (both channels and both target datasets combined). Statistical and systematic errors are added in quadrature [32].

in proton-antiproton collisions at $\sqrt{s} = 1.8$ TeV, based on data collected in Run I. The covered kinematic region was $4 < p_T < 20$ GeV and $|y| < 0.6$. The azimuthal anisotropy was not measured, and the results were given in terms of the polarization parameter α (corresponding to λ_θ) in the HX frame. The resulting p_T dependence of α is shown in Fig. 6.3 (a). The analysis indicates a significant transverse polarization for $6 < p_T < 12$ GeV. The results are compared to a NRQCD (COM) prediction (including contributions from χ_c and ψ' feed-down), compatible with the data up to 12 GeV [33].

In 2007, CDF published a result on prompt J/ψ polarization at the slightly higher center of mass energy $\sqrt{s} = 1.96$ TeV, based on a dataset collected in Run II [34]. The data analysis followed the same analysis strategy and covered an almost identical kinematic region as the previous one. The results indicate a slightly longitudinal polarization, increasing with p_T . This p_T dependence is shown in Fig. 6.3 (b), where it is compared with predictions of NRQCD (COM) and of the k_t factorization model [35]. While NRQCD predicts that the polarization increase from zero to transverse with increasing p_T , the k_t factorization model predicts a strong longitudinal polarization over the whole p_T range covered by CDF.

The model predictions are not compatible with the measured data. However, recent CSM calculations at NLO and NNLO* [19] (Fig. 6.4) predict values of α closer to the measured values after including the uncertainty due to the unknown feed-down contribution from heavier charmonium states. This uncertainty is quite large. Significant conclusions could be drawn from these calculations only after an explicit calculation of the feed-down contribution to the observable prompt J/ψ polarization (in particular, the feed-down fraction due to χ_c decays and the χ_c polarizations).

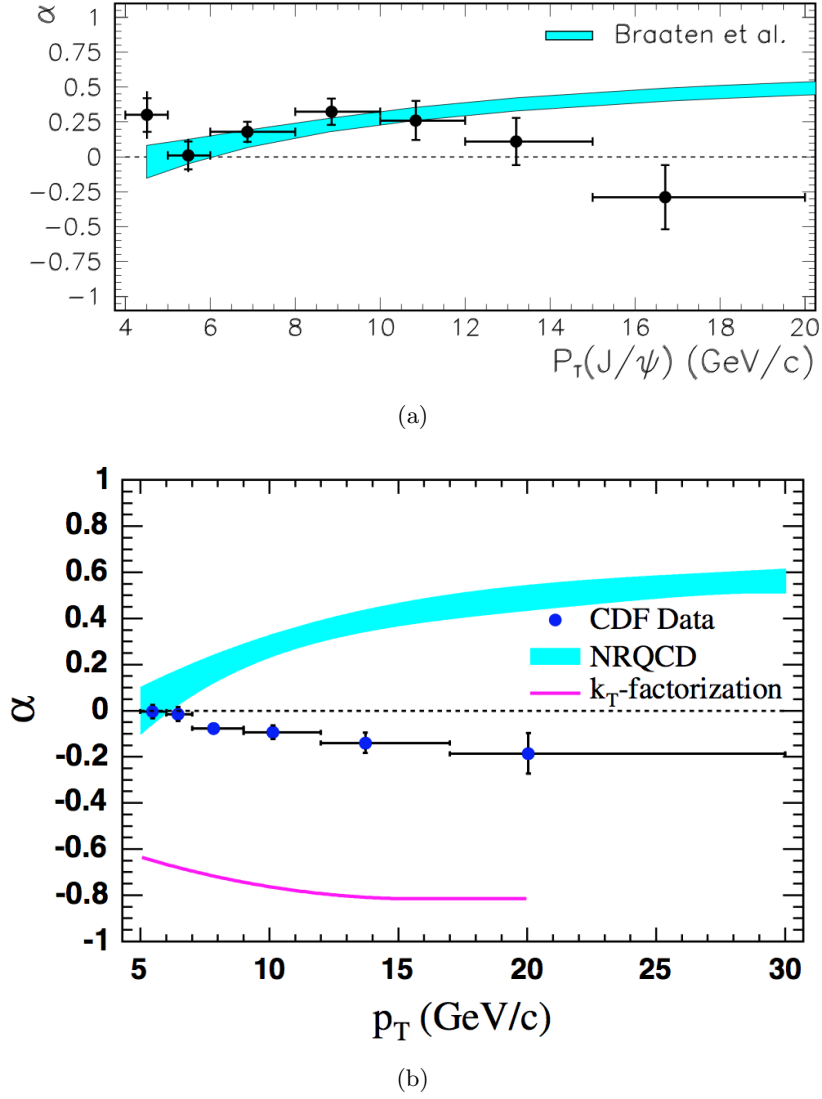


Figure 6.3: Prompt J/ψ polarization measurements obtained by CDF in the years 2000 [33] (a) and 2007 [34] (b), and corresponding model calculations [33].

The results of the two CDF measurements are incompatible over a large fraction of the covered p_T range. This discrepancy has not yet been satisfactorily explained, obviously decreasing the trust in the validity of these results.

Moreover, as the CDF analyses only measured the polar anisotropy parameter in one reference frame, the results cannot be interpreted unambiguously. In the following, if not explicitly mentioned, the *CDF polarization measurement* refers to the measurement published in 2007.

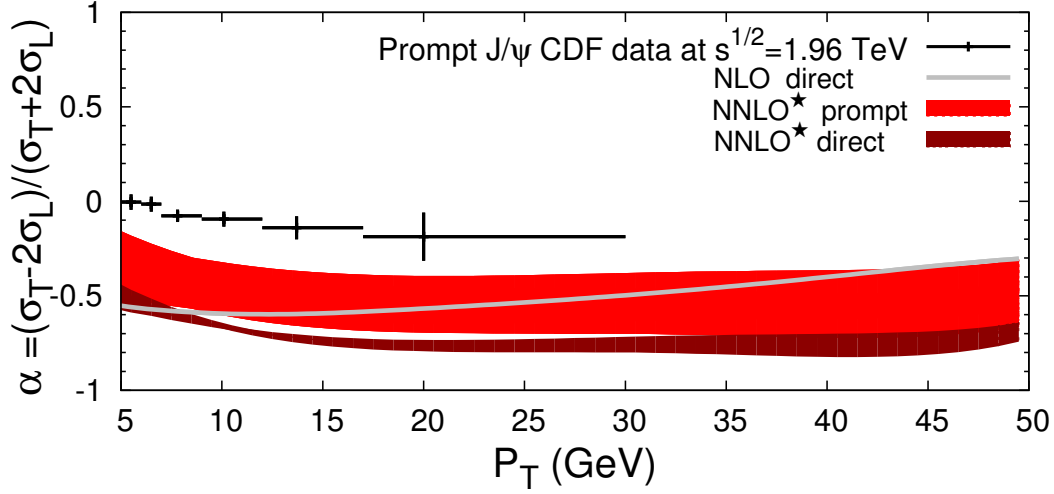


Figure 6.4: Comparison of the prompt J/ψ polarization measurement of CDF (2007) to recent CSM NLO and NNLO* calculations [36, 19].

These considerations strongly motivate a new, more complete measurement of J/ψ polarization, especially in the region of high p_T , where the model predictions are more reliable (a full transverse polarization of the directly produced vector quarkonia is an inescapable limit prediction of NRQCD, which must become valid at *sufficiently* high p_T) and more significantly different from one another.

6.2 J/ψ Polarization Scenarios from the Tevatron to the LHC

This section gives examples of how the CDF prompt J/ψ polarization measurement lends itself to several different interpretations, corresponding to different hypotheses on the unmeasured azimuthal anisotropy.

Based on these possible polarization scenarios, predictions for the LHC experiments LHCb and CMS are obtained.

The possible impact of a CMS measurement, using data collected in 2010, is illustrated by comparing the expected precision of the data with these predictions. This study shows that a high discrimination power among the different scenarios not distinguished by the CDF measurement can be achieved by measuring the azimuthal anisotropy and/or the invariant polarization parameter.

6.2.1 Possible Interpretations of Tevatron Results

As the azimuthal anisotropy of the decay was not measured by CDF, the full (two-dimensional) shape of the decay distribution is unknown. It is not possible, therefore, to infer what CDF would have measured in another reference frame, for example the CS frame. However, by taking into account all possible values of λ_φ^{HX} in the physically allowed parameter space, defined by the positivity constraints of Eq. 5.10, it is possible to constrain the range of values of λ_ϑ that CDF could have measured in the CS frame. The result of this procedure is shown in Fig. 6.5. The figure shows that a large number of very different polarization scenarios is compatible with the CDF measurement. In the following discussion three possible scenarios, corresponding to particularly simple assumptions and significantly different from one another, are considered. Figure 6.6 summarizes the kinematic dependencies of λ_ϑ^{HX} , λ_φ^{HX} , $\lambda_{\vartheta\varphi}^{HX}$ and $\tilde{\lambda}$ in the three scenarios, calculated using the transformation in Eqs. 5.7 and 5.9. The three scenarios are defined as follows.

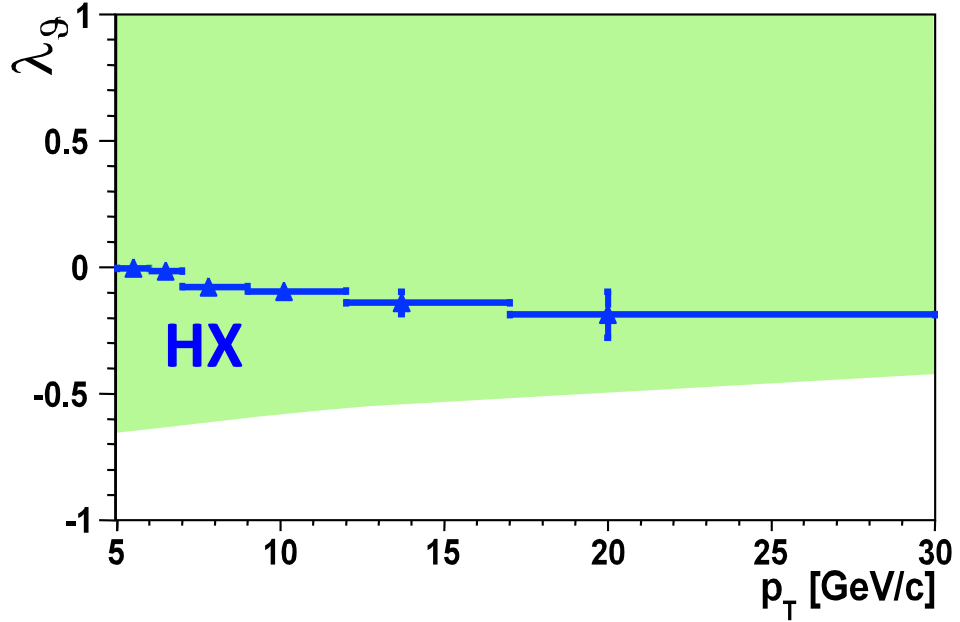


Figure 6.5: The possible values of λ_ϑ^{CS} (green area) corresponding to the CDF measurement in the HX frame (blue points) [23].

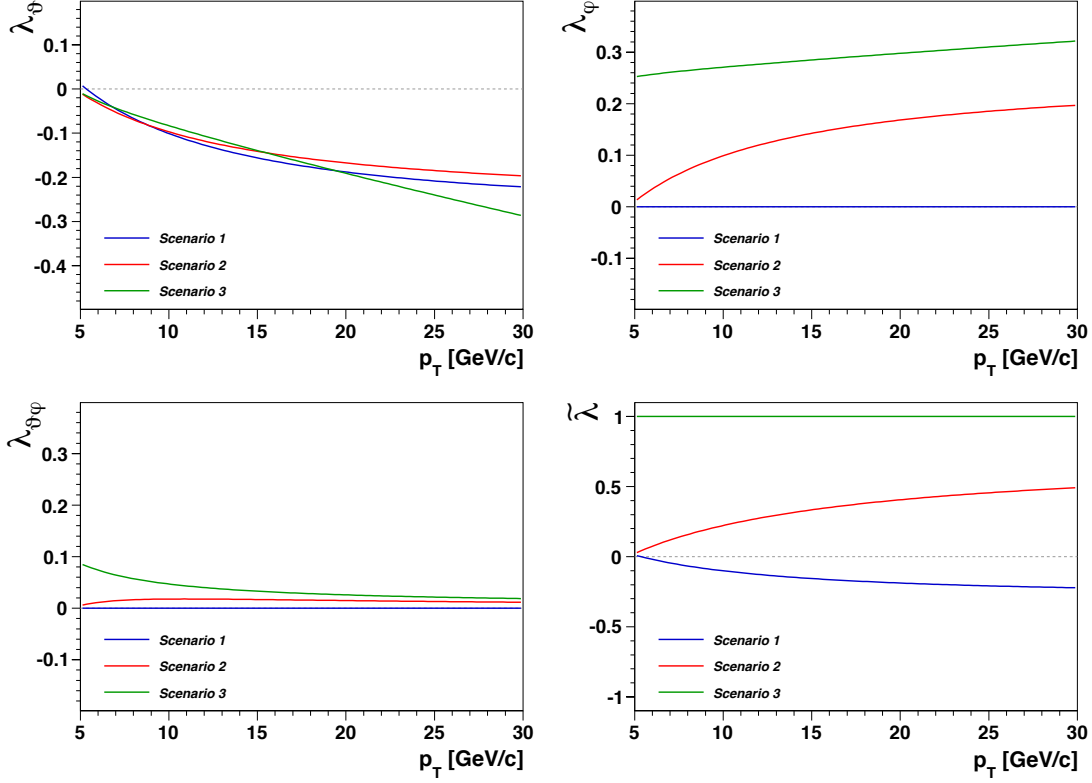


Figure 6.6: Kinematic dependence of λ_θ^{HX} , λ_ϕ^{HX} , λ_θ^{CS} and $\tilde{\lambda}$ for the three scenarios discussed in the text, in the kinematic region of the CDF measurement ($|y| < 0.6$).

Scenario 1

Scenario 1 assumes that the angular distribution is azimuthally isotropic in the HX frame, $\lambda_\phi^{HX} = 0$. This means that the polar anisotropy measured at CDF is naturally induced in the HX frame and $\lambda_\theta^{HX} = \tilde{\lambda}$. These considerations result in λ_θ^{CS} and λ_ϕ^{CS} being close to zero over the whole kinematic region. The kinematic dependence seen by CDF is purely intrinsic, induced in the HX frame.

Scenario 2

Scenario 2 assumes that the angular distribution is azimuthally isotropic in the CS frame, $\lambda_\phi^{CS} = 0$. This means that the polarization is naturally induced in the CS frame, $\lambda_\theta^{CS} = \tilde{\lambda}$. This assumption implies a transverse polarization in the CS frame ($\lambda_\theta^{CS} > 0$) and a significant azimuthal anisotropy in the HX frame, $\lambda_\phi^{HX} > 0$, both increasing with p_T . A non-zero value of λ_θ^{HX} should be measured. The kinematic dependence is purely

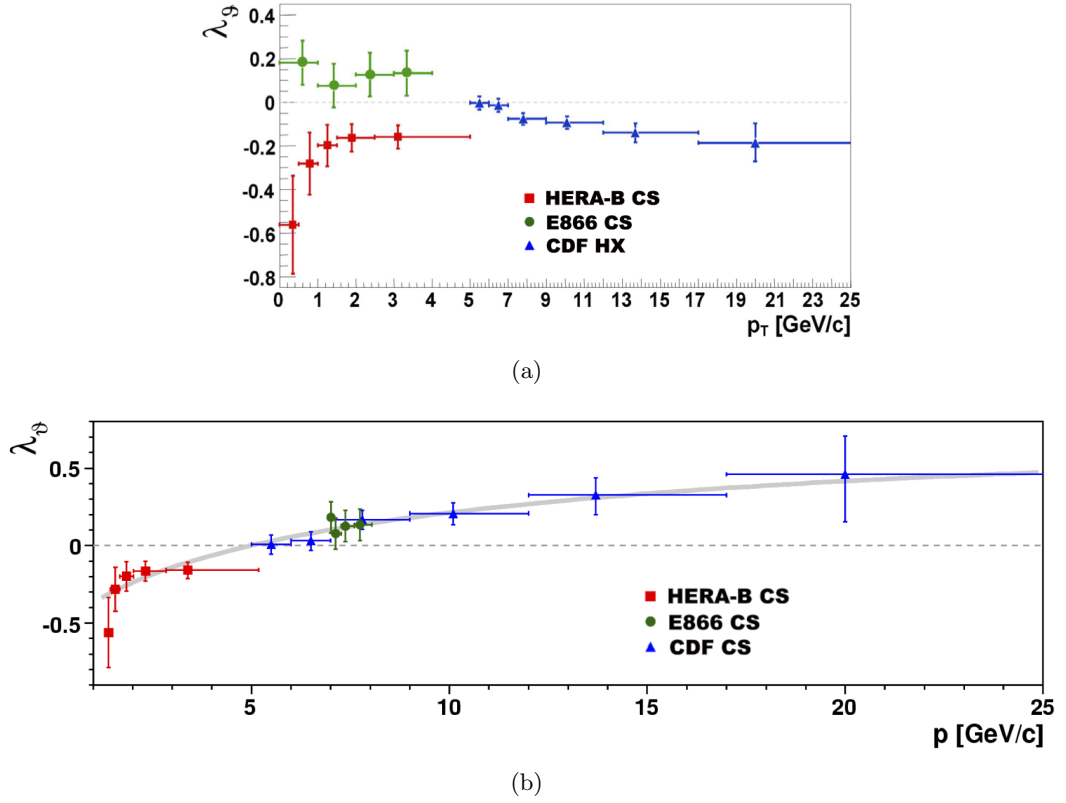


Figure 6.7: The E866 and HERA-B measurements in the CS frame and the CDF measurement in the HX frame, as a function of p_T (a). Reinterpretation of the measurements according to scenario 2 (b): the CDF measurement is translated to the CS frame and the three measurements are re-expressed as a function of p . A best-fit curve interpolates the data [37].

intrinsic when observed in the CS frame, while in the HX frame it has an extrinsic component.

This scenario is motivated by the aim of reconciling the seemingly contradictory results of E866 (CS), HERA-B (CS) and CDF (HX) (Fig. 6.7 (a)). If the CDF result is translated, under the assumptions of this scenario, into the CS frame and the three measurements are re-expressed as functions of the *total* J/ψ momentum p , it is possible to see the three measurements in smooth continuation of one another [37] (Fig. 6.7 (b)).

This scenario would indicate that J/ψ production in hadronic collisions is characterized by a natural polarization with respect to the CS axis, direction of the relative momentum of the colliding partons. This scenario can be described as assuming that the polarization of the *directly* produced J/ψ in the CS frame changes from fully longitudinal at low p to fully transverse at high p . The observed prompt J/ψ polarization saturates

6.2. J/ψ POLARIZATION SCENARIOS FROM THE TEVATRON TO THE LHC65

at high p_T (above ~ 25 GeV) at a value that is determined by the fraction of the direct component (~ 0.67), in the hypothesis that the polarizations of the feed-down contributions are negligible [37] (see discussion in Sect. 5.6).

Scenario 3

This scenario assumes that all J/ψ's are fully transversely polarized, one fraction of them having as natural polarization frame the CS frame, the other fraction being naturally polarized in the HX frame. The relative proportions between the two kinds of processes vary with p_T . The mixture changes from 70% of transversely polarized J/ψ's in the CS frame and 30% in the HX frame at 5 GeV to 85% transversely polarized J/ψ's in the CS frame and 15% in the HX frame at 20 GeV. This scenario leads to the kinematic dependence of λ_ϑ^{HX} observed by CDF, to a very large λ_φ^{HX} and to a non-negligible $\lambda_{\vartheta\varphi}^{HX}$. The frame-invariant $\tilde{\lambda}$ is +1 in the whole region, and the kinematic dependence of λ_ϑ is purely extrinsic in any frame.

6.2.2 Predictions for J/ψ Polarization at LHCb

The polarization scenarios discussed above can be translated into predictions for a polarization measurement at LHCb, using Eqs. 5.7 and 5.9 in a rapidity range accessible by the experiment, $3 < y < 3.5$. Figure 6.8 shows the predicted kinematic dependence of λ_ϑ^{HX} , λ_φ^{HX} , $\lambda_{\vartheta\varphi}^{HX}$ and $\tilde{\lambda}$.

In this rapidity region, the three scenarios acquire significantly different polar anisotropies, especially in the p_T region where the measurement will be performed ($p_T < 15$ GeV). It seems possible to discriminate between the individual scenarios by measuring λ_ϑ^{HX} alone, if the uncertainty in the parameter is smaller than 0.1. While the predictions for the kinematic dependencies of λ_φ^{HX} , $\lambda_{\vartheta\varphi}^{HX}$ and $\tilde{\lambda}$ are very close in scenarios 2 and 3, a measurement at LHCb will easily discriminate between these two and scenario 1, supporting or invalidating the hypothesis that the polarization is natural in the HX frame.

6.2.3 Predictions for J/ψ Polarization at CMS

Figure 6.9 shows the predicted kinematic dependence of λ_ϑ^{HX} , λ_φ^{HX} , $\lambda_{\vartheta\varphi}^{HX}$ and $\tilde{\lambda}$ for a CMS measurement in the rapidity range $0.9 < |y| < 1.2$. The red markers in these plots are placed at an arbitrary ordinate, coinciding with the prediction of scenario 2. The error bars indicate the estimated statistical uncertainties obtainable in a CMS measurement in the rapidity region $0.9 < |y| < 1.2$ and in three bins in p_T ($10 < p_T < 15$, $15 < p_T < 20$ and $20 < p_T < 30$ GeV), using an integrated luminosity of 40 pb^{-1} (approximately

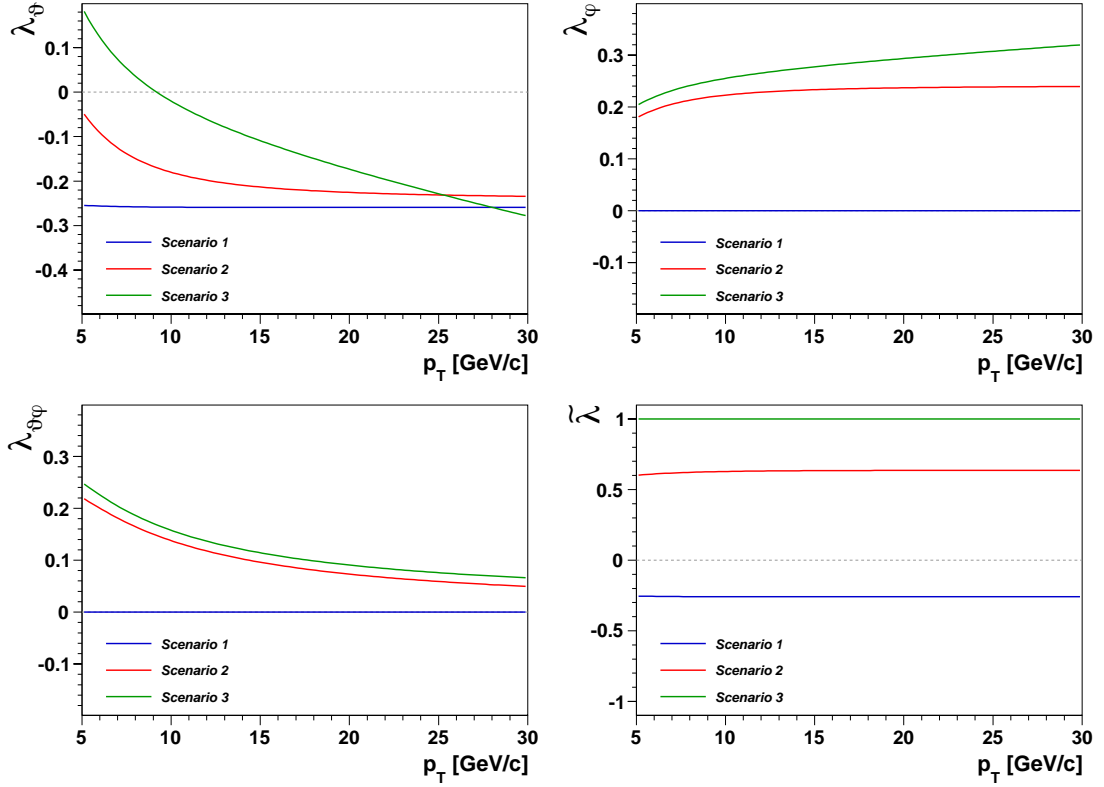


Figure 6.8: Kinematic dependence of the prompt J/ψ polarization parameters λ_θ^{HX} , λ_ϕ^{HX} , $\lambda_{\theta\phi}^{HX}$ and $\tilde{\lambda}$ in the three scenarios discussed in the text, in the kinematic region accessible by the LHCb experiment ($3 < y < 3.5$).

corresponding to the integrated luminosity collected by CMS in 2010). For the fraction of non-prompt J/ψ 's, the measured values are used (Sect. 7.5.2).

The uncertainties are estimated with toy-MC experiments (see Sect. 8.1 for more details on the method), where a simultaneous extraction of the prompt and non-prompt polarization parameters is performed over 200 statistically independent pseudo-data sets in the analysis framework described in Chap. 7. The first moment of the distribution of the resulting maximum likelihood estimates, $\hat{\lambda}_i$, is assumed to be a reasonable estimate for the statistical uncertainty on the parameter λ_i . Table 6.1 lists the estimated statistical uncertainties in the polarization parameters in five kinematic bins. The quoted uncertainties are the ones specifically corresponding to the case of zero central values.

It can be seen that the statistical uncertainty on the polar anisotropy parameter λ_θ^{HX} alone is too large for a discrimination between the three polarization scenarios. However, an effective discrimination is possible by studying the kinematic dependencies of λ_ϕ^{HX} and $\tilde{\lambda}$ at high p_T , as well as the one of $\lambda_{\theta\phi}^{HX}$ at low p_T , for which the predictions of the

6.2. J/ψ POLARIZATION SCENARIOS FROM THE TEVATRON TO THE LHC67

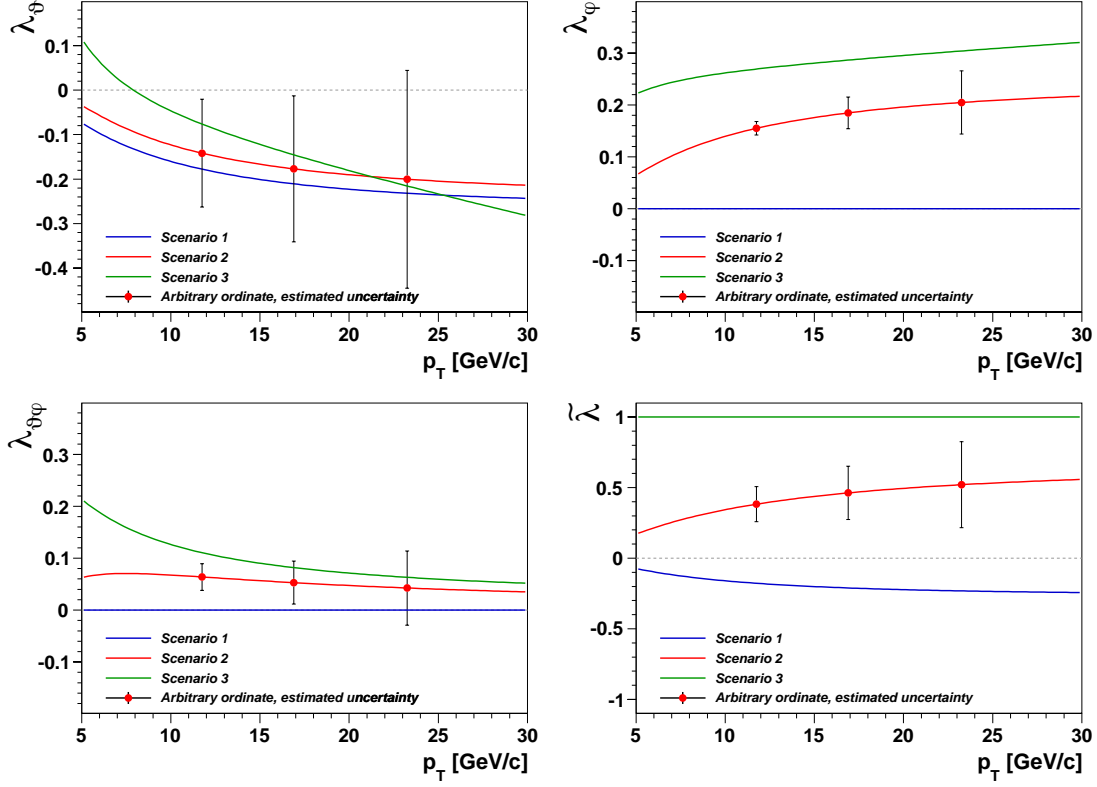


Figure 6.9: Kinematic dependence of the prompt J/ψ polarization parameters $\lambda_\theta^{H^X}, \lambda_\phi^{H^X}, \lambda_{\theta\phi}^{H^X}$ and $\tilde{\lambda}$ in the three scenarios discussed in the text, in a kinematic region accessible by the CMS experiment ($0.9 < |y| < 1.2$). Red markers indicate a possible CMS measurement with 40 pb⁻¹ (arbitrary ordinate) and the respective statistical uncertainties, estimated with toy-MC experiments.

individual scenarios are most different.

By combining the information of the measured parameters, the discrimination power increases. Figure 6.10 shows the two-dimensional parameter spaces of $\lambda_\phi^{H^X}$ vs. $\lambda_\theta^{H^X}$ and $\lambda_\phi^{H^X}$ vs. $\tilde{\lambda}$ for the bins $10 < p_T < 15$ and $20 < p_T < 30$ GeV, where the measurement has, respectively, the smallest and largest statistical uncertainties. The predictions for the three scenarios are indicated by colored markers. The error ellipses, representing the 1σ and 2σ contours, are centered on top of the prediction for scenario 2.

This study shows that, by combining information from two polarization parameters, the three scenarios can be distinguished from one another at a confidence level of more than 95%. These three scenarios only represent a small subset of the possibilities that are compatible with the CDF result. However, Fig. 6.10 (c) shows that, in certain kinematic regions, it is possible to exclude also a large fraction of the parameter space

p_T [GeV]	$\sigma(\lambda_\vartheta)$	$\sigma(\tilde{\lambda})$	$\sigma(\lambda_{\vartheta\varphi})$	$\sigma(\lambda_\varphi)$
$ y < 0.9$				
15–20	0.1109 ± 0.0057	0.1296 ± 0.0066	0.0296 ± 0.0015	0.0179 ± 0.0009
20–30	0.1549 ± 0.0077	0.1817 ± 0.0091	0.0455 ± 0.0023	0.0309 ± 0.0015
$0.9 < y < 1.2$				
10–15	0.1212 ± 0.0061	0.1241 ± 0.0062	0.0257 ± 0.0013	0.0130 ± 0.0007
15–20	0.1642 ± 0.0082	0.1883 ± 0.0094	0.0414 ± 0.0021	0.0307 ± 0.0015
20–30	0.2454 ± 0.0123	0.3039 ± 0.0152	0.0716 ± 0.0036	0.0609 ± 0.0030

Table 6.1: Statistical uncertainties, $\sigma(\lambda_i)$, of the polarization parameters λ_i in the HX frame, estimated in toy-MC experiments (unpolarized scenario).

that lies between the three indicated scenarios. Only statistical uncertainties are taken into account in these considerations.

6.3 Summary

Although many experiments have studied the spin alignment properties of the J/ψ meson, the experimental situation is inconclusive. None of the quarkonium production models discussed in Sect. 4.4 can reproduce the experimental results. As several measurements reported inconsistent results, which cannot be satisfactorily explained, the trust in these measurements decreases. Furthermore, most experiments have reported polarization properties, that cannot be interpreted unambiguously, as only the polar anisotropy was reported.

The ambiguous J/ψ polarization measurement at CDF can be interpreted in several ways. Three physically very different polarization scenarios have been discussed, that are all compatible with the CDF measurement. The study of these scenarios allow the calculation of predictions for polarization measurements at the LHC experiments. Studies with pseudo-data samples, simulating the data sample collected at CMS in 2010 allow for the estimation of the statistical uncertainties on the measurement of the individual polarization parameters. These studies lead to the conclusion, that a measurement of J/ψ polarization with the 2010 CMS data sample can already exclude a large fraction of possible scenarios that are compatible with the CDF measurement.

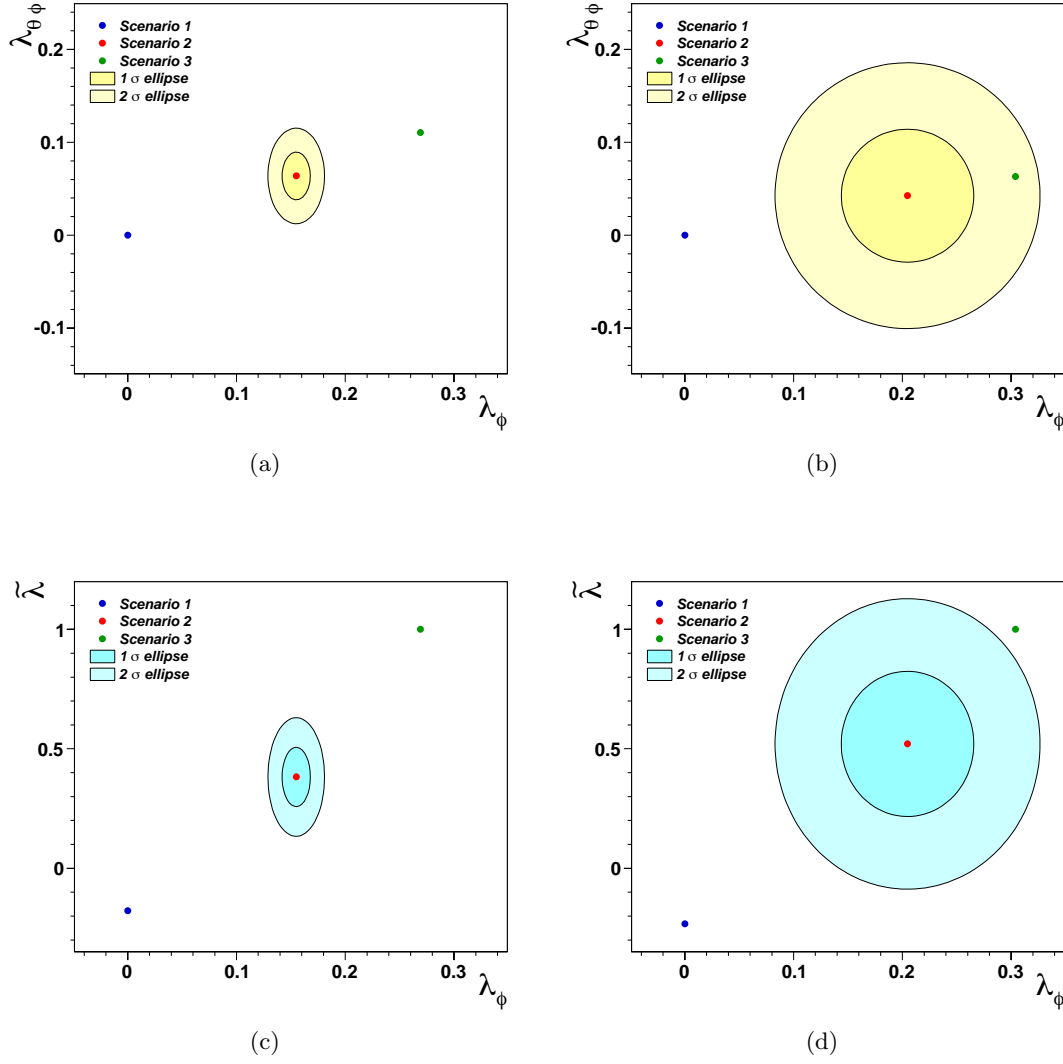


Figure 6.10: Predictions for the three scenarios (colored markers) in the two-dimensional parameter spaces λ_ϕ^{HX} vs. $\lambda_{\theta\phi}^{HX}$ ((a) (b)) and λ_ϕ^{HX} vs. $\tilde{\lambda}$ ((c) (d)) in the bins $10 < p_T < 15$ GeV ((a) (c)) and $20 < p_T < 30$ GeV ((b) (d)) and the expected statistical precisions of corresponding CMS measurements. The error ellipses (indicating the 1σ and 2σ contours) are arbitrarily placed on top of the predictions for scenario 2.

Chapter 7

J/ψ Polarization Analysis - The Baseline Method

This chapter will give a detailed report of the CMS J/ψ polarization measurement, which is the first full determination of the polar and azimuthal anisotropy of J/ψ mesons produced in proton-proton collisions at a center of mass energy of 7 TeV, based on a data sample collected by CMS.

First, to provide an overview of the measurement, the general analysis strategy will be characterized briefly (Sect. 7.1). Then, the data sample and the geometrical acceptance will be discussed (Sect. 7.2), followed by a description of the strategy to extract the detector efficiency from Monte Carlo (MC) (Sect. 7.3). Finally, the fitting procedure will be discussed in detail (Sects. 7.4 and 7.5). Various cross checks confirming the validity of the measurement strategy as well as the evaluation of the systematic effects will be presented in Chap. 8.

In view of the very large data accumulated so far in 2011, the CMS Collaboration decided to publish results based on the combination of the 2010 and 2011 data. Therefore, the analysis strategy presented in this chapter is a *snapshot* in the evolution of the measurement framework. The primary measurement strategy, discussed in this chapter, will be referred to as the *baseline method*, while the analysis strategy including further changes and improvements is referred to as the *optimized method*. These changes are partially discussed in parallel to the discussion of the baseline approach and summarized in Chap. 9.

As the measurement strategy was developed in a collective effort by the CMS polarization team, the author's individual contributions will be summarized in Appendix C.

7.1 Analysis Strategy

The measurement of quarkonium polarization is a very challenging physics analysis that involves several dimensions. Therefore a very careful approach is crucial for this study. The recently developed quarkonium polarization formalism described in Chap. 5 has been studied in detail and all suggestions of Ref. [23], summarized in Sect. 5.7, have been fully taken into account.

Decay Channel: The J/ψ polarization measurement considers the dimuon decay channel $J/\psi \rightarrow \mu^+ \mu^-$ for the extraction of the polarization result. This decay channel is very easily accessible with the CMS detector, as it was specifically designed to detect, trigger and reconstruct muons in a wide range of p_T . The branching fraction of this decay channel is approximately 5.9% [14].

Extraction of the Polarization: As discussed in Sect. 5.3, the extraction of the polarization of a vector quarkonium is equivalent to the measurement of the angular decay distribution of the positive muons in spherical coordinates $\cos\vartheta$ and φ , with respect to a certain reference frame, determined by the production plane and a chosen quantization axis. This analysis chooses to measure the angular decay distribution with respect to the CS and HX frames. From the definition of the frames (given in Sect. 5.2) it is clear that $\cos\vartheta$ and φ are fully determined by the momentum vectors of the two muons. The most general observable decay angular distribution is parametrized by the three polarization parameters $\lambda_\vartheta, \lambda_\varphi$ and $\lambda_{\vartheta\varphi}$ (Eq. 5.4) which fully determine the polarization state of the measured J/ψ data sample. The measurement of the frame-invariant parameter $\tilde{\lambda}$ provides additional information.

Geometrical Acceptance and Detector Efficiency: Although very carefully designed, CMS is not an ideal detector. Therefore, the geometrical acceptance has to be studied and taken into account. Furthermore, the detector efficiency of the muons distorts the decay angular distribution, as the efficiency has a modulation in the kinematic variables of the single muons. The effects of the geometrical acceptance and the detector efficiency are compensated by a correction of the *probability density function* (PDF), that describes the general decay angular distribution. This treatment is discussed in detail in Sect. 7.5.

Treatment of Feed-Down Contributions: While feed-down contributions from heavier charmonium states are not separated from the direct component, the feed-down contributions originating from the decay of b hadrons can be taken into account, as the respective b hadrons have lifetimes of the order of 10^{-12} s, which results in decay lengths that can be resolved by the silicon pixel detector. A detailed study of the decay length distribution allows the extraction of the results of the polarization measurement

individually for the prompt and non-prompt J/ψ contributions.

Background Estimation: The fraction of background events under the J/ψ peak is estimated by a fit to the dimuon mass distribution of the J/ψ data sample (Sect. 7.5.1). Crucial information about the decay length and decay angular distribution of the background is extracted from the background regions.

Kinematic Dependence: As the polarization is expected to show a kinematic dependence (either intrinsic or extrinsic, Sect. 5.4.2), and as kinematic smearing over large ranges in J/ψ rapidity and p_T should to be avoided [23], the data sample is divided in several kinematic bins, for which the results are obtained individually.

Monte Carlo Simulation: In the actual extraction of the polarization, MC simulations are only used for acceptance and efficiency evaluation. Furthermore, MC simulations have been used to validate the analysis strategy.

Fitting Techniques: The baseline results are obtained by *Monte Carlo Markov Chain* (MCMC) methods. Cross checks and systematic checks are conducted with the unbinned maximum likelihood method.

7.2 The Data Sample

This section will first discuss the muon, as it is defined and reconstructed at CMS, and the High Level Triggers (HLT) used in this analysis. The geometrical acceptance and the corresponding necessary single muon fiducial cuts will be discussed, followed by a brief summary of the data processing step, a description of the Monte Carlo simulations, and the presentation of the final event yields used in the analysis to extract the polarization.

7.2.1 Muon Reconstruction in CMS

The muon reconstruction starts in each individual subdetector of the muon system (Sect. 3.4.2). The individual signals in the DTs, CSCs and RPCs are matched to form *segments*. The reconstructed segments of the individual muon stations are then matched, which already leads to first estimates of position, direction and momentum vectors, which are called *seeds*. The seeds are used as starting point for the track fit, which is then performed based on *Kalman filter* techniques. The result of the track fit is a muon object which is referred to as *standalone muon* and is defined by the *muon track* [38].

As the information content of the muon systems depends on the muon momentum, there are two differing approaches to match information from the inner tracking systems with information from the muon systems, which results in two definitions of the eventually used muons in the HLT menus and for physics analysis: *global muons* and *tracker muons*.

Global Muons

The global muon is created by an *outside-in* method. A standalone muon track is combined with each consistent track of the inner tracker (*tracker track*), and matched to the one that best matches the muon track. The track fitting algorithm is repeated, with the combined information of the tracker track and the muon track, exploiting the full CMS resolution for the track reconstruction and muon momentum estimation [38].

This combined track is defined as a global muon, which is the default, high quality muon, also referred to as *HLT muon*.

Tracker Muons

The tracker muon is created by an *inside-out* method. Every single tracker track is considered a muon candidate, and used as seed to search for compatible signals in the muon system. The requirements of a tracker muon are looser than for a global muon, as a single reconstructed segment fulfills the tracker muon requirements. Therefore, the purity is worse than for global muons [38].

However, this approach is useful, especially for analyses such as the J/ψ polarization analysis, as tracker muons allow lower p_T muons to be reconstructed, with respect to global muons, as these muons often cannot reach the outer muon stations to leave enough hits to be reconstructed as a standalone muon.

One has to be careful in the usage of tracker muons though. By using well designed muon quality cuts, the muon purity can be increased. The single muon quality cuts used in this analysis are discussed in Sect. 7.2.3.

In this analysis, if a muon is identified both as global and tracker muon, it is defined as global muon, to keep the two categories exclusive.

7.2.2 The High Level Trigger

The standard dimuon HLT path used in most dimuon analyses is the *HLT_DoubleMu0* (referred to as *DoubleMu trigger*). The DoubleMu trigger requires two HLT muons to be reconstructed in a certain event to fire the trigger. While this trigger ensures a very good dimuon purity with a very low fake rate, it is inefficient for low p_T muons. There are three reasons why this inefficiency is problematic in view of a J/ψ polarization analysis [39]:

- The largest fraction of the produced J/ψ mesons are in a p_T range not accessible by the DoubleMu trigger.

- The J/ψ polarization analysis should cover the widest p_T range possible, to be able to measure possible kinematic dependencies.
- If the single muon p_T is affected by some lower threshold, the acceptance coverage in $\cos\vartheta$ and φ is limited. In the HX frame this affects the $\cos\vartheta$ dimension (only good coverage around 0), in the CS frame this affects the φ dimension.

Therefore, a low p_T trigger has been developed and studied for this analysis, the *HLT_Mu0_TkMu0_Jpsi* trigger path (referred to as *low p_T trigger*). The requirements for this trigger are very similar as for the DoubleMu trigger, except that one of the muons can be a tracker muon, only inducing a signal in one single muon station (see discussion above). This trigger has a significantly increased efficiency for low p_T muons and hence for low p_T dimuons and therefore allows the analysis to probe lower p_T regions [39]. The DoubleMu trigger was used for the baseline method. After encountering problems with the ρ -factor (Sect. 9.2), the efforts were focused on the low p_T trigger, being used in the optimized method.

As during the 2010 runs the instantaneous luminosity increased by more than five orders of magnitude, the individual trigger paths had to be adjusted and made stricter, to avoid exceeding the trigger bandwidth limits. The total collected integrated luminosity in 2010 was 43.17 pb^{-1} [10], 39.6 pb^{-1} were certified for studies involving muons [39].

Evolution of the DoubleMu Trigger

Two DoubleMu trigger paths were active during the 2010 data taking period. 8.65 pb^{-1} were collected with the standard configuration, without any further requirements. 31.34 pb^{-1} were collected with the *HLT_DoubleMu0_Quarkonium_v1* path, which required two opposite sign muons in a dimuon mass window of $1.5 < m_{\mu\mu} < 14.5 \text{ GeV}$, to reduce the trigger rate [40].

Evolution of the low p_T Trigger

The low p_T trigger was active in four versions during the 2010 data taking period. Table 7.1 shows the different trigger paths used, and the corresponding integrated luminosities. In RunA the low p_T trigger selected dimuon events in a suitable dimuon mass region about the J/ψ pole mass. In RunB1 an opposite sign criterium was added to the HLT path. In the *tight* versions of the trigger paths of RunB2 and RunB3, there was a further dimuon cut implemented, the *cowboy dimuon cut*. If the two muons are emitted so that the magnetic field bends them towards each, $\phi(\mu^-) - \phi(\mu^+) < 0$, the dimuon is defined as cowboy dimuon and is rejected. This cut, not active in the trigger

Run Period	Trigger path	\hat{L} [pb^{-1}]
RunA	HLT_Mu0_TkMu0_Jpsi	3.1
RunB1	HLT_Mu0_TkMu0_OST_Jpsi	15.7
RunB2	HLT_Mu0_TkMu0_OST_Jpsi_Tight_v2	18.6
RunB3	HLT_Mu0_TkMu0_OST_Jpsi_Tight_v3	2.3

Table 7.1: Run periods, corresponding low p_T trigger paths, and the collected integrated luminosity [39].

paths used in RunA and RunB1, is applied offline (in the optimized method only) to all events. This dimuon cut is necessary because of the inefficiencies caused by the fact that the two muons can cross the muon detectors too close to each other, being interpreted as a single muon [39].

7.2.3 Data Processing

All offline data processing at CMS is done within the *CMS software framework* (CMSSW), which provides all tools necessary for the individual steps of the physics analysis. One important part of the CMSSW framework is the *Physics Analysis Toolkit* (PAT), which is a high-level analysis layer that includes all algorithms provided by the *Physics Objects Groups* (POGs) such as the muon POG. After the *PATification* step, a reconstructed muon (consisting of tracker tracks and muon tracks) is converted in a PAT muon, a physics object allowing for easy access to all relevant quantities within one object [41].

The reconstructed samples are processed with the modules */HeavyFlavorAnalysis/Onia2MuMu* (PATification) and *JPsiAnalyzerPAT.cc*, providing a data set containing all variables relevant for the analysis.

During this step, certain single muon quality cuts are applied, which are needed to increase the muon purity of tracker and global muons. Table 7.2 summarizes the quality cuts used in this analysis [39]. Furthermore, a minimum vertex probability of 1% is requested, to ensure that the two reconstructed muons originate from the same vertex with a high probability.

7.2.4 Monte Carlo Samples

The primary MC sample used in this analysis was generated with the PYTHIA 6.4.22 event generator and processed with the *full simulation* package of the CMSSW framework, based on GEANT-4. Final state radiation (FSR) effects were simulated with the PHOTOS package [39]. This MC sample (referred to as *Fall10 MC sample*, following

Number of silicon track hits	> 10
χ^2/ndf of track fit	< 1.8
Number of pixel layer hits	> 1
$ dx(\text{Primary Vertex}) $	$< 3 \text{ cm}$
$ dz(\text{Primary Vertex}) $	$< 15 \text{ cm}$
Number of valid muon hits (only for global muons)	> 0
χ^2/ndf of global fit (only for global muons)	< 20

Table 7.2: Single muon quality cuts used in the J/ψ polarization analysis [39].

the standard CMS MC nomenclature) is used for the efficiency evaluation and certain cross checks, such as *tests with simplified MC simulation* and the *MC consistency test* (Chap. 8).

Additionally, a high statistics ($2 \cdot 10^9$ events) *private MC sample* was produced in order to evaluate the geometrical acceptance with reduced statistical fluctuations. This sample was produced including smearing and FSR effects with the packages EvtGen and PHOTOS. The events were produced flat in p_T and y , then re-weighted according to p_T and $|y|$ functions, obtained from distributions published by ATLAS. Due to the assumed kinematic distributions, the use of this sample introduces a model dependence [39].

7.2.5 Geometrical Acceptance and Fiducial Cuts

Even if the trigger bandwidth would allow the collection of muons without a p_T threshold, CMS would not be able to reconstruct muons with a transverse momentum below a certain value, depending on $|\eta|$. In the barrel region, a muon with $p_T < 3 \text{ GeV}$ cannot reach the outer muon stations. The strong magnetic field of 3.8 T curls the muon tracks, and the muons are absorbed in the detector before they can enter the muon systems. In the forward region, this effect is less pronounced. However, if the momentum of the muon is too low, the muon cannot reach the muon system in the endcap region either, because of energy loss in the material in front of the muon system [39].

These effects and the detector geometry define the CMS muon *geometrical acceptance*. As muons at the edges of the acceptance regions are very difficult to describe in terms of efficiency, it is of advantage to apply cuts on the single muons, called *fiducial cuts*, to avoid those problems. These cuts are exactly defined and can be taken into account in the fitting framework (Sect. 7.5).

The baseline method defines these cuts as functions of single muon pseudo-rapidity $|\eta|$. Figure 7.1 shows kinematic distributions of single muons originating from J/ψ decays from the Fall10 MC sample, after generation and reconstruction. The edges of

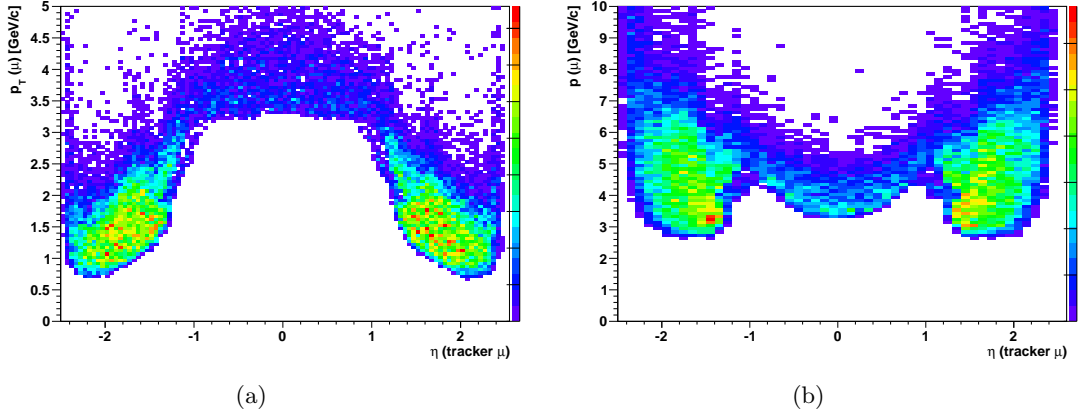


Figure 7.1: Event population of generated and reconstructed single muons (Fall10 MC sample) decaying from J/ψ 's. (a) p_T vs. η , (b) p vs. η of the tracker muon [39].

the geometrical acceptance show flat behavior in p_T at midrapidity and very forward rapidity, and flat behavior in p at forward rapidity. The single muon fiducial cuts are therefore defined as [39]

$$\begin{aligned}
 p_T &> 3.3 \text{ GeV} & \text{for } |\eta| < 1.3, \\
 p &> 2.9 \text{ GeV} & \text{for } 1.3 < |\eta| < 2.2, \\
 p_T &> 0.8 \text{ GeV} & \text{for } 2.2 < |\eta| < 2.4.
 \end{aligned} \tag{7.1}$$

These cuts ensure that the muons considered in the analysis are in phase space regions where the efficiency is larger than zero, and the J/ψ can be measured.

The acceptance is evaluated with the private MC sample as two-dimensional histograms (*acceptance maps*) in the dimuon variables $\cos \vartheta$ and φ , separately for the CS and HX frames as well as for each kinematic cell in p_T and $|y|$, individually for the prompt and non-prompt component. The acceptance maps of the prompt and non-prompt components only differ due to the assumed p_T and $|y|$ distributions.

The acceptance is defined as the fraction of events N_{acc} that pass the selection criteria of Eq. 7.1 with respect to all generated events N_{gen} [39]

$$A(p_T, |y|, \cos \vartheta, \varphi) = \frac{N_{acc}(p_T, |y|, \cos \vartheta, \varphi)}{N_{gen}(p_T, |y|, \cos \vartheta, \varphi)}. \tag{7.2}$$

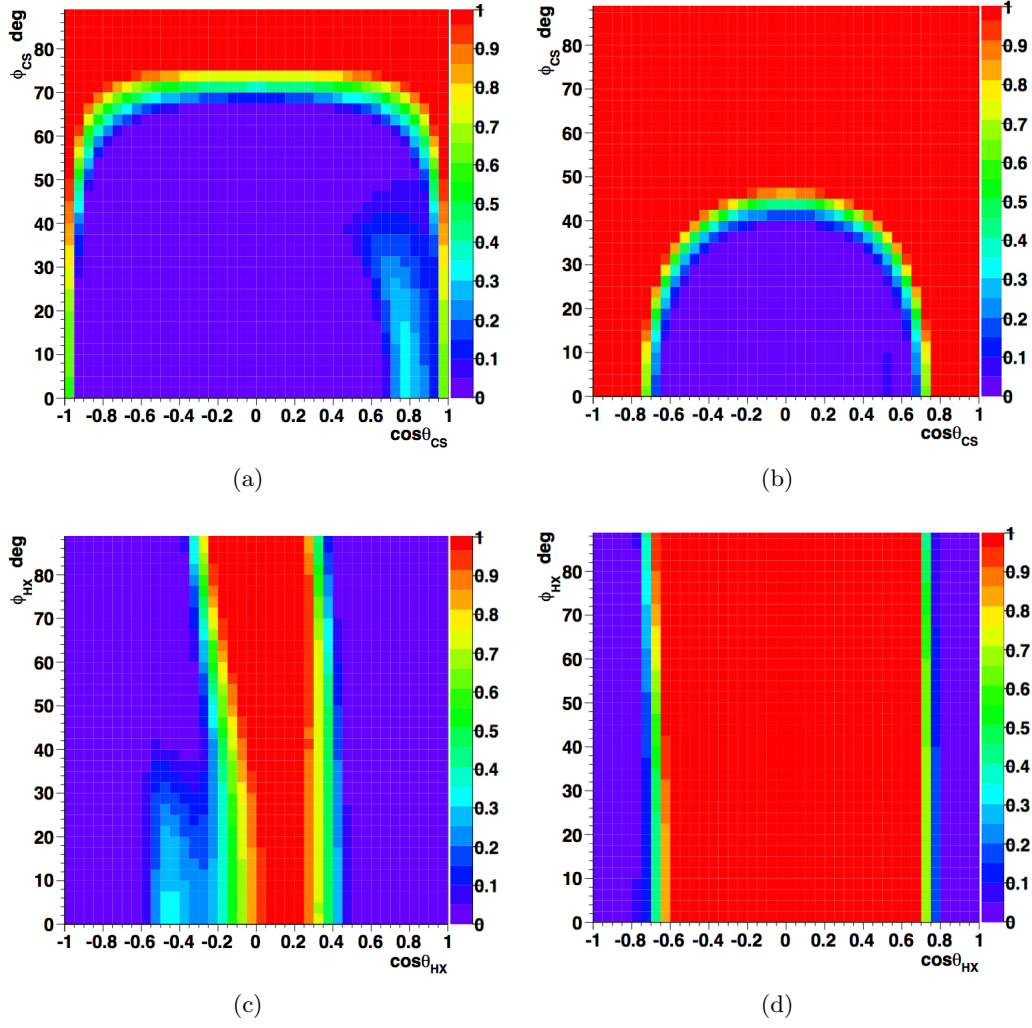


Figure 7.2: Geometrical acceptance maps at midrapidity ($|y| < 0.9$) in the CS frame for (a) $8 < p_T < 10$ GeV, (b) $20 < p_T < 30$ GeV and in the HX frame for (c) $8 < p_T < 10$ GeV, (d) $20 < p_T < 30$ GeV. The values of the acceptance is indicated by the color code, changing linearly from 0% (violet) to 100% (red) [39].

Due to limited statistics in the evaluation of acceptance maps and the efficiency maps as well as the data itself, the decay angular distribution is folded in φ [39]:

$$\begin{aligned}
 \varphi &\rightarrow 180^\circ + \varphi, \vartheta \rightarrow -\vartheta & \text{for } -180^\circ < \varphi < -90^\circ, \\
 \varphi &\rightarrow -\varphi, \vartheta \rightarrow \vartheta & \text{for } -90^\circ < \varphi < 0^\circ, \\
 \varphi &\rightarrow 180^\circ - \varphi, \vartheta \rightarrow -\vartheta & \text{for } 90^\circ < \varphi < 180^\circ.
 \end{aligned} \tag{7.3}$$

Figure 7.2 shows examples of folded geometrical acceptance maps, calculated for the

CS and HX frames in different kinematic regions. The fiducial cuts cause large holes in the $\cos\vartheta - \varphi$ phase space. The higher the p_T , the better the phase space coverage. While in the CS frame the φ coverage is limited due to the geometrical acceptance, the HX frame suffers from a loss of $\cos\vartheta$ coverage at the edges of the $\cos\vartheta$ distribution ($\cos\vartheta \rightarrow \pm 1$). This is especially problematic, as this is the most sensitive area concerning the polarization parameters.

To account for the necessary single muon cuts, these acceptance maps are used as corrections to the PDF, describing the decay angular distribution. This correction is described in more detail in Sect. 7.5.

The optimized method uses tighter cuts than the baseline method. These cuts will be motivated and shown in Chap. 9, as well as the respective treatment of the geometrical acceptance.

7.2.6 Event Yields

Due to the acceptance holes at low p_T and due to worse dimuon mass and lifetime resolutions at forward rapidity, as well as a less accessible efficiency determination, the analysis is limited to the phase space of $p_T > 8$ GeV and $|y| < 1.2$. In this kinematic region, after reconstruction, fulfilling DoubleMu trigger requirements, data processing, single muon fiducial and dimuon cuts, the data sample contains $\sim 186k$ J/ψ events in a mass range of $\pm 2\sigma$ about the fitted J/ψ pole mass [39]. The event yields of the individual kinematic bins are shown in Tab. 7.3. The fit to obtain these yield estimates is based on a gaussian signal model and a linear background model.

	$ y < 0.9$	$0.9 < y < 1.2$
$8 < p_T < 10$ GeV	39	24
$10 < p_T < 15$ GeV	63	25
$15 < p_T < 20$ GeV	18	6
$20 < p_T < 30$ GeV	8	3

Table 7.3: Approximate J/ψ event yields in the considered kinematic cells in thousands of events, triggered by the DoubleMu trigger and surviving all cuts [39].

7.3 Efficiency Determination with MC Simulation

The efficiency determination is a very crucial part of the J/ψ polarization analysis. The baseline method relies on MC based efficiencies, while the optimized method evaluates the efficiencies with the data driven *tag and probe* method (Sect. 9.2).

The dimuon efficiency $\epsilon_{\mu\mu}$ can be factorized in the *reconstruction efficiency* ϵ_{reco} , representing inefficiencies due to the muon quality cuts and due to reconstruction, and the *trigger efficiency* ϵ_{trig} ,

$$\epsilon_{\mu\mu} = \epsilon_{reco} \cdot \epsilon_{trig}. \quad (7.4)$$

The reconstruction efficiency describes the probability that a muon reaching the muon system is reconstructed. The trigger efficiency describes the probability that a reconstructed muon fulfills the trigger requirements.

The *efficiency maps* are evaluated similarly to the acceptance maps as two-dimensional histograms in the dimuon variables $\cos \vartheta$ and φ , separately for the CS and HX frames as well as for each kinematic cell in p_T and $|y|$ from the Fall10 MC sample. Efficiency maps are individually evaluated for the prompt and non-prompt component, only differing by the assumed p_T and $|y|$ distributions.

The reconstruction efficiency is defined as the fraction of reconstructed events N_{reco} that satisfy the muon quality criteria (Tab. 7.2) with respect to the events N_{acc} that satisfy the acceptance criteria [39]

$$\epsilon_{reco}(p_T, |y|, \cos \vartheta, \varphi) = \frac{N_{reco}(p_T, |y|, \cos \vartheta, \varphi)}{N_{acc}(p_T, |y|, \cos \vartheta, \varphi)}. \quad (7.5)$$

The trigger efficiency is defined as the fraction of events N_{trig} that satisfy the trigger requirements with respect to the events N_{reco} that are reconstructed and satisfy the muon quality cuts [39]

$$\epsilon_{trig}(p_T, |y|, \cos \vartheta, \varphi) = \frac{N_{trig}(p_T, |y|, \cos \vartheta, \varphi)}{N_{reco}(p_T, |y|, \cos \vartheta, \varphi)}. \quad (7.6)$$

The factorization of reconstruction and trigger efficiencies is therefore justified, by construction. Figure 7.3 shows examples of reconstruction and trigger efficiency maps for a certain kinematic cell. One clearly sees that the available statistics of the Fall10 MC sample leads to large statistical fluctuations of the efficiency maps, therefore a coarse binning has to be used, even after the folding in φ .

As the efficiency maps show a significant modulation in the $\cos \vartheta$ - φ plane, the decay angular distribution is distorted due to these inefficiencies. Therefore, the efficiency has to be taken into account, similarly to the acceptance maps, by applying the efficiency maps as corrections to the PDF (Sect. 7.5).

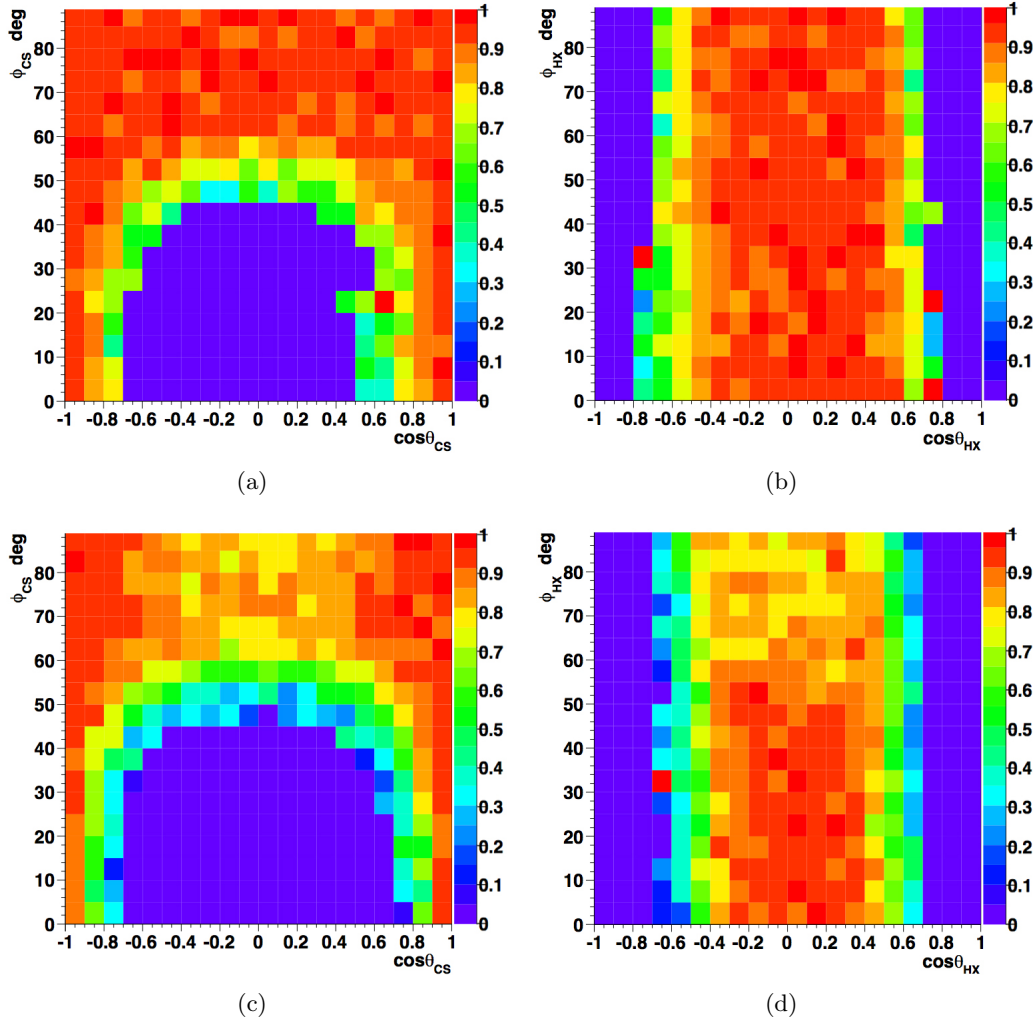


Figure 7.3: Reconstruction efficiency maps in the CS frame (a) and in the HX frame (b), trigger efficiency maps for the DoubleMu trigger in the CS frame (c) and in the HX frame (d). All maps for midrapidity ($|y| < 0.9$) in the cell $15 < p_T < 20$ GeV. The values of the efficiencies are indicated by the color code, changing linearly from 0% (violet) to 100% (red) [39].

In the following, efficiency maps of the prompt ($E_{PR}(\cos\vartheta, \varphi)$) and non-prompt component ($E_{NP}(\cos\vartheta, \varphi)$) refer to the product of the reconstruction and trigger efficiency maps. For these and the acceptance maps of the prompt and non-prompt components ($A_{PR}(\cos\vartheta, \varphi), A_{NP}(\cos\vartheta, \varphi)$), the p_T and $|y|$ dependence is no longer indicated explicitly, as the fits are conducted separately for each kinematic cell, correcting the PDF with the corresponding maps.

7.4 Fitting Technique and Minimization

The fitting framework described in Sect. 7.5 uses two different approaches for the extraction of the polarization parameters. The baseline results are obtained with Markov Chain Monte Carlo methods, which allow reliable error estimates. As these methods are very time consuming, a maximum likelihood method is used for cross checking purposes and systematic checks. In the following sections the maximum likelihood method is discussed in detail, starting with an introduction to the principles and illustrated by an example. Then, the MINUIT minimizing algorithms and the *RooFit* package will be discussed. MCMC methods are described in detail elsewhere ([14] and references within).

7.4.1 The Likelihood Method

Given a sample of n observations X_1, \dots, X_n , distributed according to a probability density function $f(x|\lambda)$, in the random variable x , parametrized by the parameter λ , one can define the *likelihood function* by [42]

$$L(\lambda) = \prod_{i=1}^n f(X_i|\lambda). \quad (7.7)$$

In general, x can also be a vector and λ can be a set of parameters. The normalization of the PDF $f(x|\lambda)$ has to be appropriately taken into account, as the integral

$$\int f(x|\lambda) dx = 1 \quad (7.8)$$

over the full region in which x is properly defined has to result in 1, independently of the parameter λ . The *maximum likelihood estimator* $\hat{\lambda}$ is the value of λ that maximizes the likelihood function $L(\lambda)$. The estimator $\hat{\lambda}$ has some beneficial properties as it is asymptotically unbiased, efficient and consistent [42].

In the majority of cases, instead of the likelihood function the logarithm of the likelihood function is maximized - the log-likelihood function

$$l(\lambda) = \log L(\lambda) = \sum_{i=1}^n \log f(X_i|\lambda). \quad (7.9)$$

Alternatively, as mathematically equivalent, the *negative-log-likelihood* (NLL) function can be minimized, in order to find the maximum likelihood estimator $\hat{\lambda}$.

The likelihood method allows fits to binned and unbinned datasets, in opposition to a usual least χ^2 binned fit. It allows to extract the maximum information from a low

statistics sample, which is advantageous given the requirements of the multi-dimensional fit discussed in this analysis.

Example: Exponential Decay

In order to illustrate the consistency of the maximum likelihood estimator, and to emphasize the importance of the correct normalization of the PDF, the method is demonstrated by a simple example.

Assume a sample of n measurements t_1, \dots, t_n of a process following an exponential decay

$$N(t) = N_0 \cdot e^{-\frac{t}{\tau}}. \quad (7.10)$$

Under the condition of Eq. 7.8, we obtain $N_0 = \frac{1}{\tau}$ and can define the properly normalized PDF of the exponential decay

$$E(t|\tau) = \frac{1}{\tau} \cdot e^{-\frac{t}{\tau}}. \quad (7.11)$$

The corresponding likelihood function $L(\tau)$ and the log-likelihood function $l(\tau)$ then result in

$$L(\tau) = \prod_i \frac{1}{\tau} \cdot e^{-\frac{t_i}{\tau}}, \quad l(\tau) = -\frac{\sum_i t_i}{\tau} - n \ln \tau. \quad (7.12)$$

After maximization of the log-likelihood function with the condition $\frac{dl}{d\tau}|_{\hat{\tau}} = 0$ we obtain the maximum likelihood estimate

$$\hat{\tau} = \frac{\sum_i t_i}{n} = \bar{t}_i, \quad (7.13)$$

as expected, the arithmetic mean of the n measurements of t . In order to calculate an error estimate on the obtained maximum likelihood estimate we calculate the second derivative at the obtained value of $\hat{\tau}$

$$\frac{d^2 l}{d\tau^2} \Big|_{\hat{\tau}} = \frac{n}{\hat{\tau}^2} - 2 \frac{\sum_i t_i}{\hat{\tau}^3} = -\frac{n}{\hat{\tau}^2}, \quad (7.14)$$

and can therefore define the variance $V_{\hat{\tau}}$ and the error estimate $\sigma_{\hat{\tau}}$ as

$$V_{\hat{\tau}} = -\frac{1}{\frac{d^2 l}{d\tau^2} \Big|_{\hat{\tau}}} = \frac{\hat{\tau}^2}{n}, \quad \sigma_{\hat{\tau}} = \sqrt{V_{\hat{\tau}}} = \frac{\hat{\tau}}{\sqrt{n}}, \quad (7.15)$$

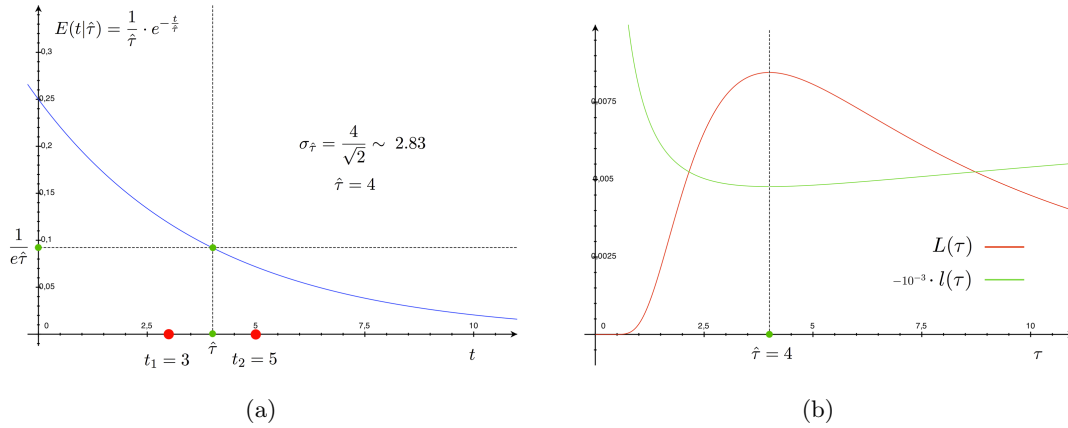


Figure 7.4: Example of a maximum likelihood estimation of an exponential decay PDF $E(t|\tau)$, based on a sample of 2 measurements $t_1 = 3$, $t_2 = 5$. The maximum likelihood estimator results in $\hat{\tau} = 4$ with an error estimate of $\sigma_{\hat{\tau}} \sim 2.83$. (a) shows the resulting PDF, (b) shows the likelihood function and the NLL function (scaled by factor 10^{-3}).

which delivers the expected results. Figure 7.4 shows an example of a maximum likelihood estimation based on a sample of two measurements of t .

If the normalization condition of Eq. 7.8 is omitted ($N_0 = 1$), the PDF, the likelihood function and the log-likelihood function transform to

$$E'(t|\tau) = e^{-\frac{t}{\tau}}, \quad L'(\tau) = \prod_i e^{-\frac{t_i}{\tau}}, \quad l'(\tau) = -\frac{\sum_i t_i}{\tau}. \quad (7.16)$$

Minimizing the log-likelihood function returns the maximum likelihood estimate $\hat{\tau}' = 0$ and the corresponding error estimate $\sigma_{\hat{\tau}'} = 0$ which are, of course, wrong results.

This simple example shows the consistency of the maximum likelihood method, as well as the importance of the correct normalization of the PDF.

7.4.2 Minimization Algorithms

The NLL functions that have to be minimized in order to extract the polarization properties of the J/ψ (Eqs. 7.35 and 7.36) cannot be differentiated analytically. Therefore, numerical minimization algorithms have to be used.

The MINUIT minimization package [43] offers a very well tested and stable set of algorithms used for minimization and error estimation. Several MINUIT algorithms are employed in this analysis. For the central values of the likelihood estimate the MIGRAD algorithm is used. It is a variable-metric minimizer that produces an error matrix

estimate as by-product. The error matrix estimate can be unreliable in some cases, e.g. if the number of steps used to approach the minimum is too small. In these cases MINUIT offers two algorithms for proper error estimation. The HESSE algorithm calculates the matrix of second derivatives at the point of the minimum by numerical differentiation. This algorithm is very reliable, if the log-likelihood function shows parabolic behavior in all parameters, in the surrounding area of the minimum. The MINOS algorithm can cope with non-parabolic behavior, as it does not rely on the calculation of derivatives, but follows the likelihood outwards, until it reaches a certain value above the minimum [43]. However, the MINOS algorithm is very time consuming.

The MINUIT algorithms are called from within the *RooFit* framework [44], which is a very powerful and flexible toolkit that is implemented in the object oriented ROOT environment. The RooFit package and its rich libraries allow us to easily build PDFs, to perform binned and unbinned likelihood fits and to generate pseudo-data samples (*toy-MC samples*) drawn from the models. As RooFit allows very intuitive access to the MINUIT package, it is common to design the NLL function within the RooFit framework, and minimize it via the MINUIT interface.

7.5 The Fitting Procedure

In this section the details of the fitting framework designed for the estimation of the J/ψ polarization parameters and the correct error estimates are given. The analysis presented is a proper multivariate analysis that uses a two-step fitting procedure for the extraction of the polarization parameters.

The first step is a two-dimensional simultaneous unbinned maximum likelihood fit to the dimuon mass and decay length distributions, in order to estimate the fraction of the background and non-prompt J/ψ contributions. The corresponding likelihood function is determined by the studied data set and two one-dimensional PDFs $M(m_{\mu\mu}|\mathcal{M},\mathcal{N}_{ML})$ and $L(l_{J/\psi}|\mathcal{L},\mathcal{N}_{ML})$, characterizing the dimuon mass and decay length distributions with \mathcal{M} and \mathcal{L} , sets of parameters parametrizing the mass and decay length PDFs together with \mathcal{N}_{ML} , the set of normalization parameters of the mass/decay length PDF.

The second step is a two-dimensional simultaneous unbinned maximum likelihood fit to the decay angular distribution, extracting the polarization properties of the prompt and non-prompt J/ψ contributions individually. The likelihood function of the second step is determined by the data set and the two-dimensional PDF $P(\cos\vartheta, \varphi|\mathcal{P},\mathcal{N}_P)$, describing the decay angular distribution with \mathcal{P} , the set of parameters parametrizing the PDF, together with \mathcal{N}_P , the set of normalization parameters of the decay angular distribution PDF.

7.5.1 Dimuon Mass Model

The dimuon mass variable $m_{\mu\mu}$ is determined (in natural units) by the two muon momentum vectors in the laboratory frame

$$\vec{p}^{\mu^+} = \begin{pmatrix} p_x^{\mu^+} \\ p_y^{\mu^+} \\ p_z^{\mu^+} \end{pmatrix}, \quad \vec{p}^{\mu^-} = \begin{pmatrix} p_x^{\mu^-} \\ p_y^{\mu^-} \\ p_z^{\mu^-} \end{pmatrix}, \quad (7.17)$$

and the total energies of the two muons

$$E^{\mu^+} = \sqrt{m_\mu^2 + |\vec{p}^{\mu^+}|^2}, \quad E^{\mu^-} = \sqrt{m_\mu^2 + |\vec{p}^{\mu^-}|^2}, \quad (7.18)$$

with the general relation for the invariant mass of a dimuon decay

$$m_{\mu\mu} = \sqrt{2m_\mu^2 + 2(E^{\mu^+}E^{\mu^-} - \vec{p}^{\mu^+} \cdot \vec{p}^{\mu^-})}. \quad (7.19)$$

The dimuon mass distribution is characterized by a background contribution and a signal contribution. The background is modeled by an exponential PDF

$$M_{Bkg}(m_{\mu\mu}|\lambda_m) = e^{-\lambda_m m_{\mu\mu}}. \quad (7.20)$$

The prompt and the non-prompt components are expected to show the same dimuon mass distribution, hence they cannot be distinguished by the dimuon mass variable $m_{\mu\mu}$, and are combined in a single signal contribution. This contribution is modeled by a *Crystal Ball* (CB) function, which allows to take the FSR tail into account. This CB function is characterized by four CB parameters $\mathcal{CB}_4 = \{\mu_m, \sigma_m, \alpha_m, n_m\}$. The CB function is defined differently in two parts of the dimuon mass/parameter space, separated by the cut $CB_{cut} = \frac{m_{\mu\mu} - \mu_m}{2\sigma_m}$. In the region $CB_{cut} > -\alpha_m$ the CB function takes the form of a gaussian

$$M_{Sig}(m_{\mu\mu}|\mathcal{CB}_4) = e^{-\frac{(m_{\mu\mu} - \mu_m)^2}{2\sigma_m^2}}, \quad (7.21)$$

while under the condition $CB_{cut} \leq -\alpha_m$ the CB function describes the effects of the FSR tail

$$M_{Sig}(m_{\mu\mu}|\mathcal{CB}_4) = \left(\frac{n_m}{|\alpha_m|}\right)^{n_m} e^{\frac{-|\alpha_m|^2}{2}} \left[\left(\frac{n_m}{|\alpha_m|} - |\alpha_m|\right) - \frac{(m_{\mu\mu} - \mu_m)}{2\sigma_m} \right]^{-n_m}. \quad (7.22)$$

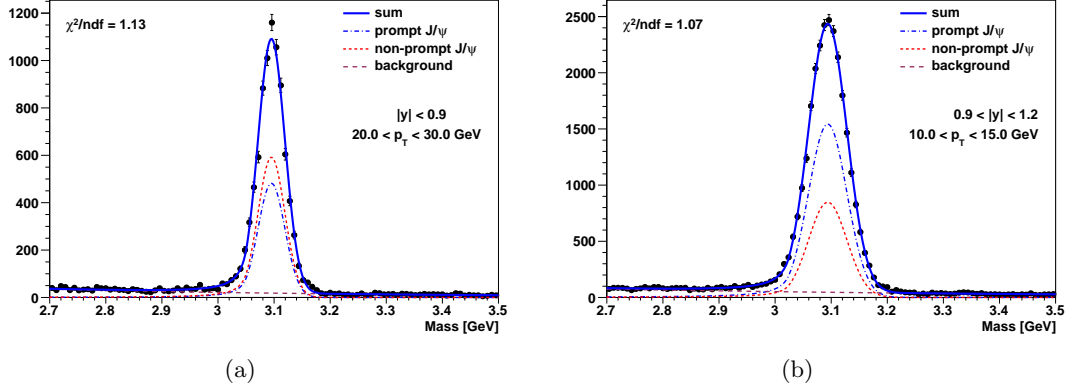


Figure 7.5: Examples of the distribution of data in the dimuon mass variable $m_{\mu\mu}$ together with the fit results, visualizing the individual components, in the bins $|y| < 0.9$, $20 < p_T < 30$ GeV (a) and $0.9 < |y| < 1.2$, $10 < p_T < 15$ GeV (b) [39].

The ansatz for the combined dimuon mass PDF then reads

$$M(m_{\mu\mu}|\mathcal{M},\mathcal{N}) = n_{Sig} \cdot M_{Sig}(m_{\mu\mu}|\mathcal{CB}_4) + n_{Bkg} \cdot M_{Bkg}(m_{\mu\mu}|\lambda_m) \quad (7.23)$$

with $\mathcal{M} = \{\mathcal{CB}_4, \lambda_m\}$ the set of parameters parametrizing the dimuon mass distribution and $\mathcal{N} = \{n_{Sig}, n_{Bkg}\}$ the set of normalization parameters for the signal and background contributions.

Figure 7.5 shows examples of fit results, projected on the dimuon mass variable $m_{\mu\mu}$. The dimuon mass can then be used to define a *signal region* (SR) and a *background region*, referred to as the *mass sidebands* (SB) [39]

$$\begin{aligned} \text{Left sideband (LSB): } & 2.7 \text{ GeV} < m_{\mu\mu} < \mu_m - 4\sigma_m, \\ \text{Signal region (SR): } & \mu_m - 3.5\sigma_m < m_{\mu\mu} < \mu_m + 3.5\sigma_m, \\ \text{Right sideband (RSB): } & \mu_m + 4\sigma_m < m_{\mu\mu} < 3.5 \text{ GeV}. \end{aligned} \quad (7.24)$$

The data in the SBs is not included in the extraction of the polarization parameters, but relevant information about the background normalization, the decay length distribution and the decay angular distribution of the background can be collected from data in the mass SBs (discussion in Sect. 7.5.4).

The *signal over background ratio* (S/B) can be estimated correspondingly to the event yields shown in Tab. 7.3. Under the J/ψ peak, in a mass window of $\pm 2\sigma_m$ about the pole mass, the background fraction is less than 5% in all kinematic bins (Tab. 7.4).

	$ y < 0.9$	$0.9 < y < 1.2$
$8 < p_T < 10 \text{ GeV}$	2.3	3.4
$10 < p_T < 15 \text{ GeV}$	2.6	3.8
$15 < p_T < 20 \text{ GeV}$	3.1	4.2
$20 < p_T < 30 \text{ GeV}$	3.5	4.6

Table 7.4: Background fraction (in %) under the J/ψ peak, in a mass window of $\pm 2\sigma_m$ about the pole mass. Estimated from the DoubleMu trigger sample in the considered kinematic cells [39].

7.5.2 Decay Length Model

The feed-down of J/ψ 's from the decay of b hadrons (mostly from the B^+ , B_s and B^0 mesons and the Λ_b baryon) constitutes a very significant contribution to the J/ψ data sample. As discussed in Sect. 5.6, feed-down contributions are expected to have different polarization properties as directly produced J/ψ 's. Therefore, it is important to carefully take this feed-down contribution into account.

As these b hadrons decay in characteristic lifetimes of the order of 10^{-12} s [14], they can cover a mean distance of the order of 500 μm , before they decay to a J/ψ which in turn quasi instantly decays ($\sim 10^{-20}$ s [14]) in two muons. These distances can be resolved by the carefully designed silicon tracker. Therefore, the discrimination between the prompt and the non-prompt J/ψ component relies on the measurement of the distance between the secondary dimuon vertex and the primary vertex, in the plane orthogonal to the beam line, which is characterized by the *pseudo-proper decay length* $l_{J/\psi}$ [45]

$$l_{J/\psi} = L_{J/\psi} \cdot \frac{m_{\mu\mu}}{p_T}, \quad (7.25)$$

with $L_{J/\psi}$ the *proper decay length*, defined as the most probable transverse decay length

$$L_{J/\psi} = \frac{\mathbf{u}^T \sigma^{-1} \mathbf{x}}{\mathbf{u}^T \sigma^{-1} \mathbf{u}}, \quad (7.26)$$

with \mathbf{x} the vector joining the primary and secondary vertex in the transverse plane, \mathbf{u} the unit vector of the J/ψ momentum \vec{p} projected on the plane orthogonal to the beam pipe and σ the sum of the primary and secondary vertex covariance matrices [45]. The *pseudo-proper decay length* will be referred to as *decay length* or *lifetime*, in the context of $c\tau = l_{J/\psi}$ describing the pseudo-proper decay time.

Although unphysical, negative values of $l_{J/\psi}$ are possible due to resolution effects, in cases where the vector \mathbf{x} points in the opposite direction with respect to the vector \mathbf{u} .

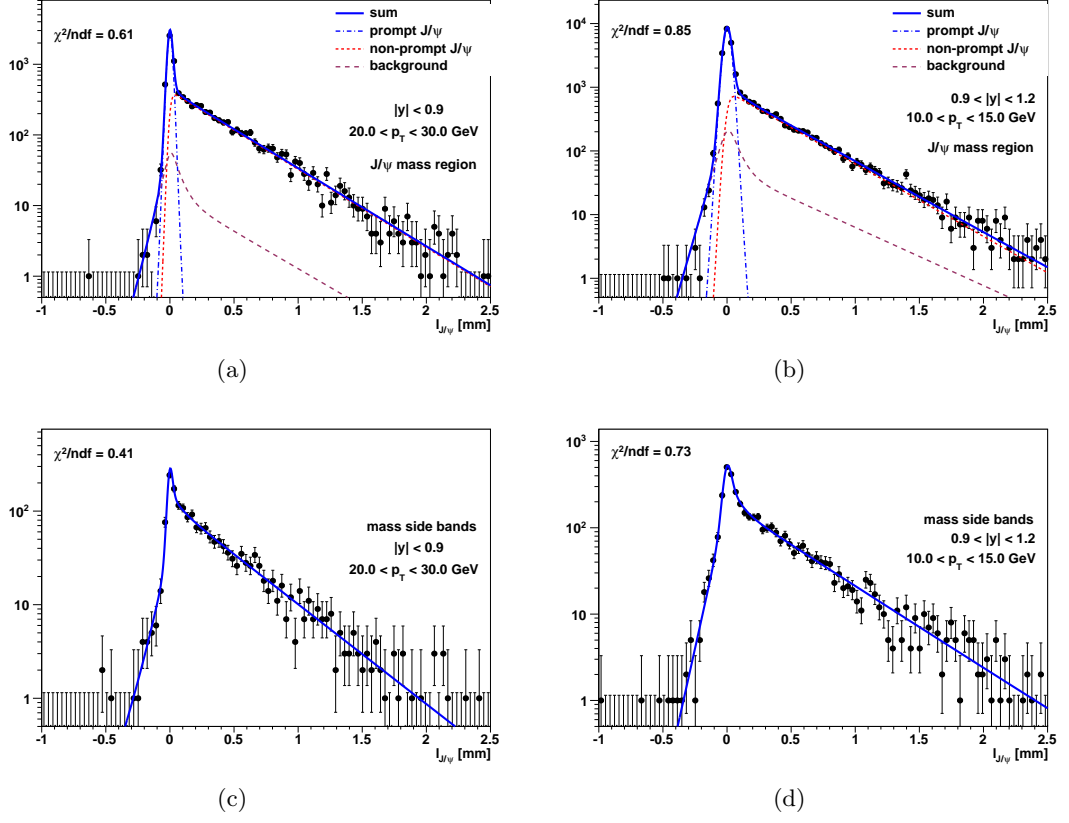


Figure 7.6: Examples of the distribution of data in the decay length variable $l_{J/\psi}$ together with the fit results, in the mass signal region ((a) (b)) and in the mass sidebands ((c) (d)) in the bins $|y| < 0.9$, $20 < p_T < 30$ GeV ((a) (c)) and $0.9 < |y| < 1.2$, $10 < p_T < 15$ GeV ((b) (d)) [39].

The decay length distribution is described by a composite model consisting of three contributions, the prompt and non-prompt J/ψ components, as well as the background contribution. On a *truth* level, the distribution of the quasi instantly decaying prompt component can be characterized by a delta function at $l_{J/\psi} = 0$. Thus, the measured distribution can be modeled by a resolution function, describing the decay length resolution of the tracker. The description of this resolution function makes use of the *per-event vertexing error* σ_i , determined by the covariance matrices of the primary and secondary vertices. The resolution function for n events is then modeled as a weighted sum of n gaussians (G)

$$L_{PR}(l_{J/\psi}|\mu_l, \sigma_l) = \sum_{i=1}^n \left[\frac{1}{\sigma_i} G(l_{J/\psi}|\mu_l, \sigma_l \cdot \sigma_i) \right], \quad (7.27)$$

which can be interpreted as a fit of the pull distribution of the errors. Therefore, μ_l is expected to result in a value close to 0 and σ_l close to 1, which is observed. The pull distribution is equivalent to the distribution of the standard scores, see Sect. 8.1 for a detailed discussion.

The non-prompt component is modeled by an analytical convolution of the resolution function with an exponential decay shape,

$$L_{NP}(l_{J/\psi}|\mu_l, \sigma_l, \tau_l^{NP}) = L_{PR}(l_{J/\psi}|\mu_l, \sigma_l) \otimes e^{-\tau_l^{NP} l_{J/\psi}}, \quad (7.28)$$

characterized by the parameter τ_l^{NP} , which was found to be a sufficient description.

The background is modeled similarly, with an additional contribution, a double sided exponential decay, to describe the background events with negative $l_{J/\psi}$,

$$\begin{aligned} L_{Bkg}(l_{J/\psi}|\mu_l, \sigma_l, \tau_{l1}^{Bkg}, \tau_{l2}^{Bkg}, f_{DS}) &= L_{PR}(l_{J/\psi}|\mu_l, \sigma_l) \otimes \\ &\otimes \left[(1 - f_{DS}) \cdot e^{-\tau_{l1}^{Bkg} l_{J/\psi}} + f_{DS} \cdot e^{-\tau_{l2}^{Bkg} |l_{J/\psi}|} \right], \end{aligned} \quad (7.29)$$

with τ_{l1}^{Bkg} and τ_{l2}^{Bkg} the parameters characterizing the slope of the single sided and double sided exponential PDFs and f_{DS} defining the fraction of the double sided exponential with respect to the single sided exponential PDF.

The combined decay length PDF then reads

$$\begin{aligned} L(l_{J/\psi}|\mathcal{L}, \mathcal{N}) &= n_{PR} \cdot L_{PR}(l_{J/\psi}|\mu_l, \sigma_l) \\ &+ n_{NP} \cdot L_{NP}(l_{J/\psi}|\mu_l, \sigma_l, \tau_l^{NP}) \\ &+ n_{Bkg} \cdot L_{Bkg}(l_{J/\psi}|\mu_l, \sigma_l, \tau_{l1}^{Bkg}, \tau_{l2}^{Bkg}, f_{DS}), \end{aligned} \quad (7.30)$$

with $\mathcal{L} = \{\mu_l, \sigma_l, \tau_l^{NP}, \tau_{l1}^{Bkg}, \tau_{l2}^{Bkg}, f_{DS}\}$ the set of parameters parametrizing the decay length distribution, the normalization parameter n_{PR} for the prompt signal contribution, n_{NP} for the non-prompt signal contribution (with the condition $n_{Sig} = n_{PR} + n_{NP}$) and n_{Bkg} for the background contribution.

This parametrization of the decay length distribution is completely data driven, and describes the distribution found in the data very well. Figure 7.6 shows examples of fit results, projected on $l_{J/\psi}$, in the signal and sideband regions separately.

With this approach, it is possible to extract the polarization properties of the prompt and non-prompt J/ψ contributions separately.

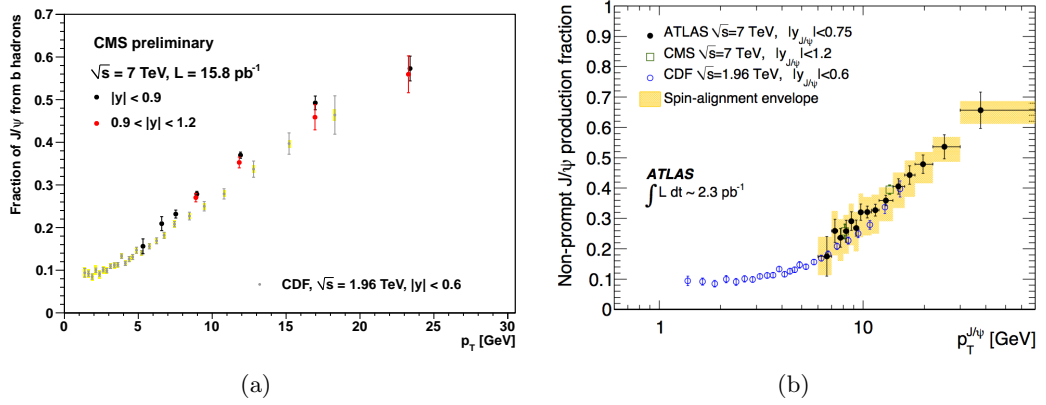


Figure 7.7: (a) B-fraction measurement, as a by-product of the polarization measurement, compared to results of the b-fraction measurement of CDF [39]. (b) ATLAS measurement of the b-fraction at midrapidity, compared to CMS (differential cross section analysis) and CDF results [46]. The yellow band represents the spin alignment envelope, the systematic error arising from the unknown polarization of prompt and non-prompt J/ψ 's.

The four-dimensional treatment of the extraction of the polarization properties provides an interesting physics result as a by-product, the *b-fraction*

$$f_b = \frac{N_{NP}}{N_{PR} + N_{NP}}, \quad (7.31)$$

with N_{PR} and N_{NP} the estimated number of prompt and non-prompt signal events in the data sample. The b-fraction shows a strong kinematic dependence, increasing with p_T , and provides a further cross check, as the results of the p_T dependence of f_b can be compared to the results of b-fraction measurements reported by CMS [45], ATLAS [46] and CDF [47]. Figure 7.7 (a) shows the results of the f_b measurement of the polarization analysis, compared to CDF results. Figure 7.7 (b) shows results of an ATLAS measurement, compared to measurements of CMS and CDF at midrapidity. This plot indicates a saturation of the b-fraction at $p_T > 30$ GeV.

7.5.3 Decay Angular Distribution Model

The PDF modeling the decay angular distribution of the positive muon in spherical coordinates $\cos\vartheta$ and φ , with respect to the CS and HX reference frames, is based on

Eq. 5.4. For a single component (prompt or non-prompt) this model can be written as

$$w_{PR(NP)}(\cos \vartheta, \varphi | \vec{\lambda}^{PR(NP)}) = \frac{1}{(3 + \lambda_{\vartheta}^{PR(NP)})} (1 + \lambda_{\vartheta}^{PR(NP)} \cos^2 \vartheta + \lambda_{\varphi}^{PR(NP)} \sin^2 \vartheta \cos 2\varphi + \lambda_{\vartheta\varphi}^{PR(NP)} \sin 2\vartheta \cos \varphi). \quad (7.32)$$

This PDF is corrected by the acceptance and efficiency maps. The composite PDF describing all contributions from background, prompt and non-prompt J/ψ 's then reads

$$P(\cos \vartheta, \varphi | \mathcal{P}, \mathcal{N}) = n_{PR} \cdot w_{PR}(\cos \vartheta, \varphi | \vec{\lambda}^{PR}) \cdot A_{PR}(\cos \vartheta, \varphi) \cdot E_{PR}(\cos \vartheta, \varphi) + n_{NP} \cdot w_{NP}(\cos \vartheta, \varphi | \vec{\lambda}^{NP}) \cdot A_{NP}(\cos \vartheta, \varphi) \cdot E_{NP}(\cos \vartheta, \varphi) + n_{Bkg} \cdot w_{Bkg}(\cos \vartheta, \varphi), \quad (7.33)$$

with the set of parameters $\mathcal{P} = \{\vec{\lambda}^{PR} = (\lambda_{\vartheta}^{PR}, \lambda_{\varphi}^{PR}, \lambda_{\vartheta\varphi}^{PR}), \vec{\lambda}^{NP} = (\lambda_{\vartheta}^{NP}, \lambda_{\varphi}^{NP}, \lambda_{\vartheta\varphi}^{NP})\}$, the set of normalization parameters $\mathcal{N} = \{n_{PR}, n_{NP}, n_{Bkg}\}$, the acceptance and efficiency maps of the prompt ($A_{PR}(\cos \vartheta, \varphi)$, $E_{PR}(\cos \vartheta, \varphi)$) and non-prompt components ($A_{NP}(\cos \vartheta, \varphi)$, $E_{NP}(\cos \vartheta, \varphi)$), and the decay angular distribution of the background $w_{Bkg}(\cos \vartheta, \varphi)$, evaluated from the mass sidebands.

Figure 7.8 shows examples of fit results, projected on $\cos \vartheta$ and φ , visualizing the individual contributions.

At this point it should be mentioned that the frame-invariant parameter $\tilde{\lambda}$ can be obtained directly, substituting λ_{φ} by the expression

$$\lambda_{\varphi} = \frac{\tilde{\lambda} - \lambda_{\vartheta}}{3 + \tilde{\lambda}}. \quad (7.34)$$

This substitution has the advantage that the error on the frame-invariant parameter is propagated correctly within the RooFit package, taking correlations into account. This way the error on $\tilde{\lambda}$ is directly estimated without the need of linear error propagation.

7.5.4 The Two-Step Fitting Procedure

In the baseline method the four-dimensional problem is divided into two steps, each conducting a two-dimensional simultaneous unbinned maximum likelihood fit:

1. The first step is a fit to the dimuon mass and decay length distributions, extracting the correct normalizations of background, prompt and non-prompt components.

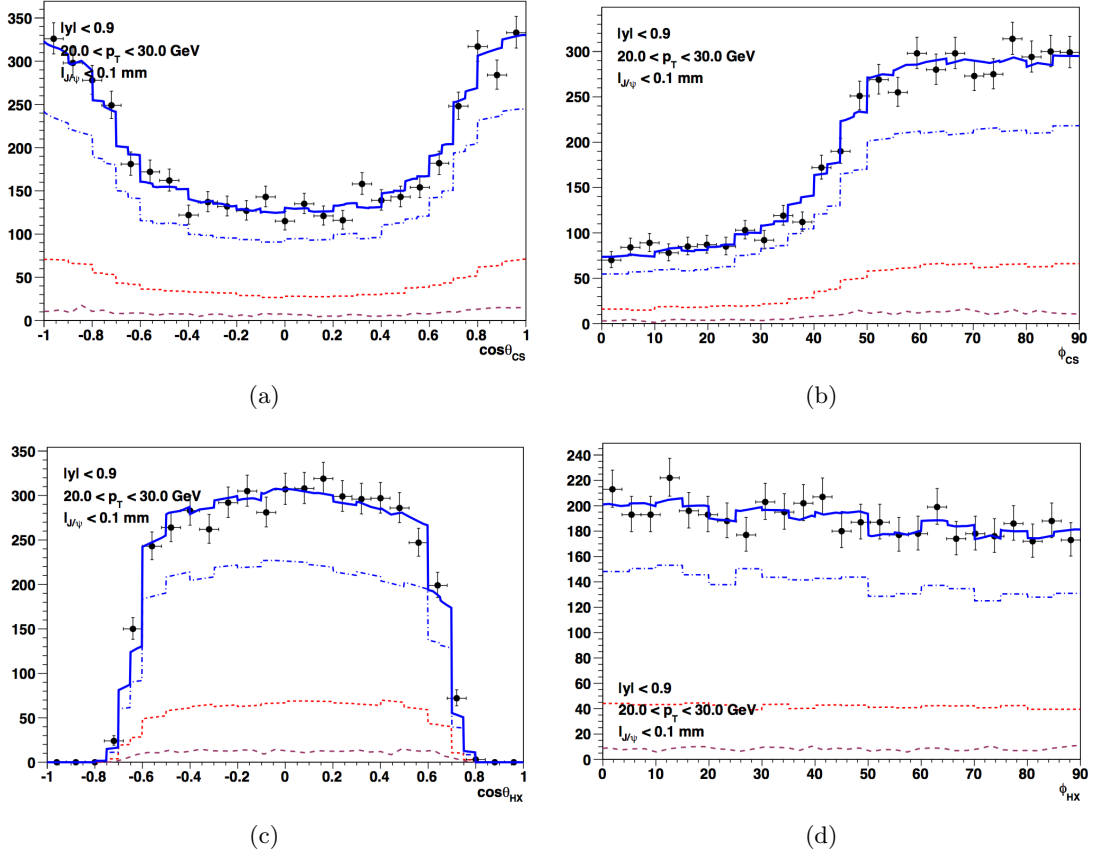


Figure 7.8: Examples of the distribution of data in $\cos\vartheta$ and φ together with the fit results in the CS frame ((a) (b)), and in the HX frame ((c) (d)), in the prompt J/ψ enriched (cut on $l_{J/\psi} < 0.1$ mm) mass signal region, showing the individual components (violet dashed: background, red dashed: non-prompt, blue dashed: prompt, blue solid: composite PDF) in the bin $|y| < 0.9$, $20 < p_T < 30$ GeV [39].

2. The second step is a fit to the decay angular distribution, extracting the polarization parameters for the prompt and non-prompt components.

This procedure simplifies the fitting framework, and decreases the time needed for the fits to converge. This factorized approach is justified if one assumes that the dimuon mass and decay length distributions are not correlated with the decay angular distribution, in the mass signal region.

Two-Dimensional Dimuon Mass and Decay Length Fit

The two-dimensional mass and decay length plane is subdivided in four regions, as visualized in Fig. 7.9:

- The left and right mass sidebands as defined by Eq. 7.24 (LSB and RSB region, grey areas);
- The non-prompt signal region, defined by a cut of $l_{J/\psi} > 0.1$ mm, to ensure that the non-prompt contribution dominates in this region (NPS region, green area);
- The prompt signal region, dominated by the prompt J/ψ contribution (PRS region, red area).

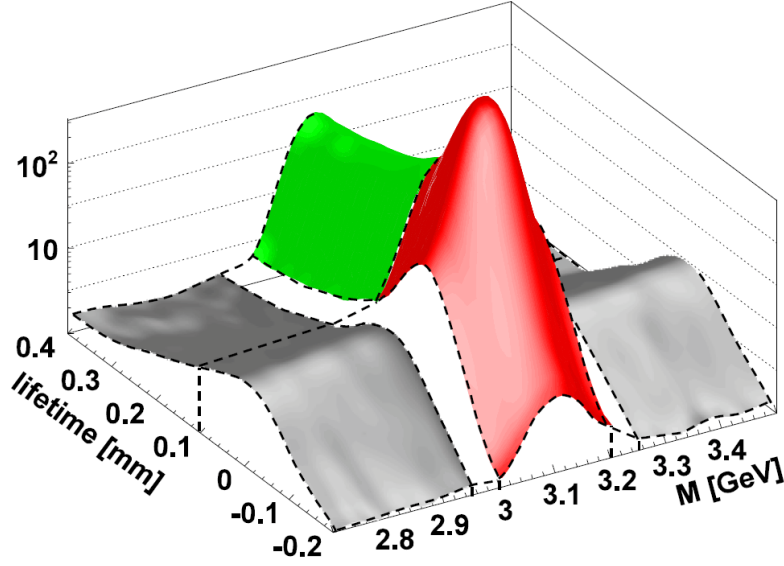


Figure 7.9: Schematic visualization of the four regions defined for the two-dimensional mass/decay length fit [39].

The background normalization is very well constrained by the dimuon mass distribution. The events in the mass SBs allow for the evaluation of the decay angular distribution of the background and constrain the decay length distribution of the background component. The decay length distributions of the prompt and non-prompt components are evaluated in the signal region. The parameters of the non-prompt decay length PDF are dominantly constrained in the non-prompt signal region, while the parameters of the prompt resolution function are constrained by the full signal region. This method increases the number of normalization parameters, as the background normalization has to be evaluated separately in the signal region and both SB regions: $\mathcal{N}_{ML} = \{n_{PR}^{(SR)}, n_{NP}^{(SR)}, n_{Bkg}^{(SR)}, n_{Bkg}^{(LSB)}, n_{Bkg}^{(RSB)}\}^i$. The SB regions are assumed to contain no signal events.

ⁱNomenclature $n_{Component}^{(Region)}$

This method is MC independent, as the sets of parameters \mathcal{M} , \mathcal{L} and \mathcal{N}_{ML} can be extracted from data alone. The advantage of this approach is that the parameters can be shared in different regions of phase space, being constrained in those regions where that parameter is most sensitive.

The total likelihood of the fit is the product of the likelihoods of the individual regions. The log-likelihood function can then be defined as the sum of the individual components,

$$\begin{aligned} \log[L_{ML}(\mathcal{M}, \mathcal{L}, \mathcal{N}_{ML})] = & \sum_{i \text{ (PRS)}} \log[M(m_{\mu\mu}^{i \text{ (PRS)}}|\mathcal{M}, \mathcal{N}_{ML})] + \sum_{i \text{ (PRS)}} \log[L(l_{J/\psi}^{i \text{ (PRS)}}|\mathcal{L}, \mathcal{N}_{ML})] \\ & + \sum_{i \text{ (NPS)}} \log[M(m_{\mu\mu}^{i \text{ (NPS)}}|\mathcal{M}, \mathcal{N}_{ML})] + \sum_{i \text{ (NPS)}} \log[L(l_{J/\psi}^{i \text{ (NPS)}}|\mathcal{L}, \mathcal{N}_{ML})] \\ & + \sum_{i \text{ (LSB)}} \log[M(m_{\mu\mu}^{i \text{ (LSB)}}|\mathcal{M}, \mathcal{N}_{ML})] + \sum_{i \text{ (LSB)}} \log[L(l_{J/\psi}^{i \text{ (LSB)}}|\mathcal{L}, \mathcal{N}_{ML})] \\ & + \sum_{i \text{ (RSB)}} \log[M(m_{\mu\mu}^{i \text{ (RSB)}}|\mathcal{M}, \mathcal{N}_{ML})] + \sum_{i \text{ (RSB)}} \log[L(l_{J/\psi}^{i \text{ (RSB)}}|\mathcal{L}, \mathcal{N}_{ML})], \end{aligned} \quad (7.35)$$

with $M(m_{\mu\mu}|\mathcal{M}, \mathcal{N}_{ML})$ and $L(l_{J/\psi}|\mathcal{L}, \mathcal{N}_{ML})$, the composite PDFs defined in Eqs. 7.23 and 7.30. The corresponding NLL can then be minimized simultaneously.

In total, this unbinned likelihood fit determines 16 free parameters: The five previously mentioned normalization parameters \mathcal{N}_{ML} , $\mathcal{M} = \{\mu_m, \sigma_m, \alpha_m, n_m, \lambda_m\}$ and $\mathcal{L} = \{\mu_l, \sigma_l, \tau_l^{NP}, \tau_{l1}^{Bkg}, \tau_{l2}^{Bkg}, f_{DS}\}$. Out of these fit parameters four parameters of interest

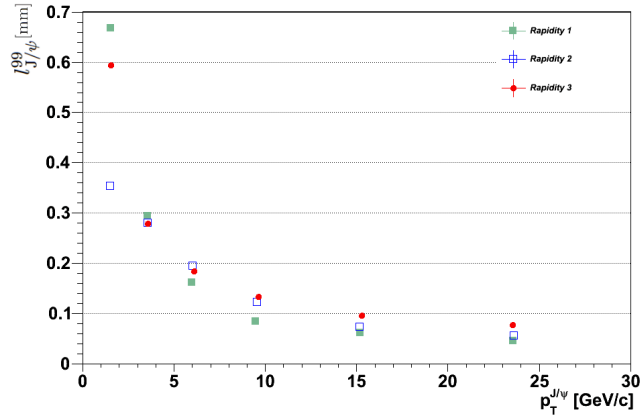


Figure 7.10: MC estimated value of $l_{J/\psi}^{99}$ vs. p_T for three rapidity regions (green: $|y| < 0.9$, blue: $0.9 < |y| < 1.2$, red: $1.2 < |y| < 1.6$).

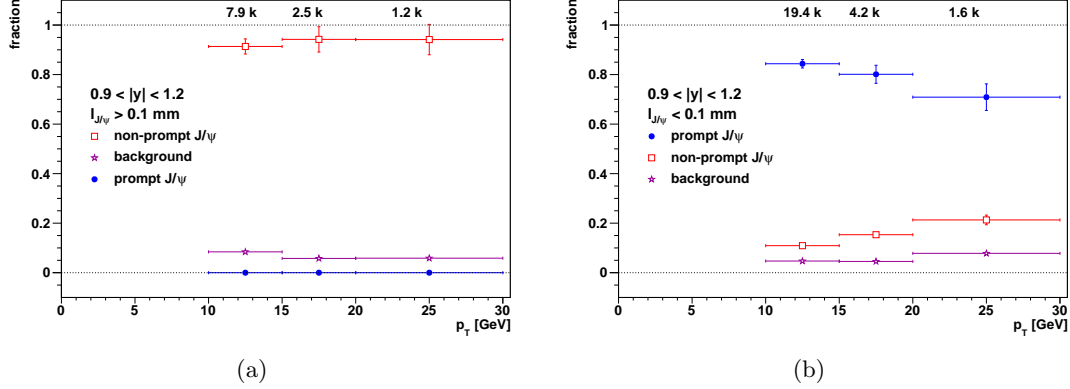


Figure 7.11: Estimated fractions of prompt, non-prompt and background components in the non-prompt signal region with $l_{J/\psi} > 0.1$ mm (a) and in the prompt signal region with $l_{J/\psi} < 0.1$ mm (b) in the bin $0.9 < |y| < 1.2$ vs. p_T . The total number of events in the respective region is shown on the top [39].

can be calculated, which are passed on as input for the two-dimensional polarization fit: the four fractions $f_{NP}^{(PRS)}$, $f_{NP}^{(NPS)}$, $f_{Bkg}^{(PRS)}$ and $f_{Bkg}^{(NPS)}$, which can be determined by numeric integration over the resulting decay length PDFs, defined by the set \mathcal{L} and normalized by the parameters \mathcal{N}_{ML} .

Figure 7.10 shows the value of $l_{J/\psi}^{99}$ vs. p_T for different rapidity regions. The values have been chosen using MC simulation and requiring at most 1% of prompt events above $l_{J/\psi}^{99}$. This value steeply decreases with p_T , reflecting the improving decay length resolution with p_T . Figure 7.11 (a) and (b) show the fractions of the individual components in the prompt and non-prompt signal regions, determined from fits to data. These figures show that the cut of $l_{J/\psi} = 0.1$ mm is well chosen so that the prompt contribution can be neglected in the non-prompt signal region.

Two-Dimensional Decay Angular Distribution Fit

The polarization parameters are extracted in the second step of the fitting procedure, for both frames in two individual fits. The two-dimensional decay angular distribution is fit to the PDF $P(\cos\vartheta, \varphi|\mathcal{P}, \mathcal{N}_P)$ introduced in Eq. 7.33. The definitions of the four regions are maintained. While data from the SB regions are only used to build the background model, the likelihood is constrained by data from the signal regions only. The fractions obtained in step 1 are fixed, as they cannot be further constrained by the $\cos\vartheta - \varphi$ distribution. The decay angular distribution of the background component is assumed to be the average distribution of the left and right mass SBs. This approach is

justified by the generally high S/B ratio and comparisons of the kinematic distributions of the LSB to the RSB.

The fit is simultaneously conducted in the prompt and non-prompt signal regions. While the non-prompt polarization parameters are mostly constrained in the non-prompt signal region, the polarization parameters of the prompt component are mostly constrained by data in the prompt signal region. The fits in the individual regions could of course be split in two separate fits, but this approach has the advantage that correlations of the prompt and non-prompt polarization parameters are taken into account directly.

The log-likelihood function of this fit can be defined as

$$\begin{aligned} \log[L_P(\mathcal{P}, \mathcal{N}_P)] = & \sum_{i \text{ (PRS)}} \log[P(\cos \vartheta^i \text{ (PRS)}, \varphi^i \text{ (PRS)} | \mathcal{P}, \mathcal{N}_P)] \\ & + \sum_{i \text{ (NPS)}} \log[P(\cos \vartheta^i \text{ (NPS)}, \varphi^i \text{ (NPS)} | \mathcal{P}, \mathcal{N}_P)] - \text{Penalty}(\mathcal{P}), \end{aligned} \quad (7.36)$$

with the penalty function $\text{Penalty}(\mathcal{P})$ which ensures that the value of the NLL is large for combinations of the polarization parameters that violate the positivity constraints (Eq. 5.10). Besides only two free normalization parameters that are necessary to steer the overall normalization in both signal regions (\mathcal{N}_P), this fit determines the 6 parameters of interest - λ_{ϑ}^{PR} , λ_{φ}^{PR} , $\lambda_{\vartheta\varphi}^{PR}$, λ_{ϑ}^{NP} , λ_{φ}^{NP} , $\lambda_{\vartheta\varphi}^{NP}$. As previously mentioned, instead of λ_{φ} , $\tilde{\lambda}$ can be obtained directly by substitution, for the prompt and non-prompt components.

7.6 Summary of the Baseline Analysis Strategy

The spin alignment properties of the J/ψ meson are studied in the dimuon decay channel. The polarization parameters λ_{ϑ} , λ_{φ} , $\lambda_{\vartheta\varphi}$ and $\tilde{\lambda}$ are extracted with a two-step fitting procedure, obtaining the results individually for the prompt and non-prompt J/ψ contributions in several narrow kinematic cells. A two-dimensional simultaneous unbinned maximum likelihood fit to the dimuon mass and decay length distribution to extract the fractions of the background and non-prompt J/ψ components is followed by a two-dimensional simultaneous unbinned maximum likelihood fit to the decay angular distribution of the positive muons in the CS and HX frames to extract the polarization parameters.

The geometrical acceptance and the muon detection efficiency are taken into account by a correction of the PDF describing the decay angular distribution.

Chapter 8

Validation of the Framework

The complete analysis framework has to be tested extensively, to ensure unbiased results and correct error estimates. The validity of the polarization fit can be tested with simplified MC simulations (Sect. 8.1). Any problem in the approach chosen for the description of the decay angular distribution can be detected by these tests. Furthermore, in Sect. 8.2 the MC consistency test will be discussed. This test detects any inconsistencies in the acceptance and efficiency determination and their implementation. Tests for the evaluation of the systematic errors are summarized in Sect. 8.3.

8.1 Tests with Simplified Monte Carlo Simulations

8.1.1 The Toy-MC Method

The polarization fit has to be tested, to ensure that the framework itself does not bias the final results. This can be done with so-called *toy-MC* tests. The RooFit package allows us to generate *pseudo-data sets* with a certain number of events N_{Events} from any chosen PDF in N_{Dim} dimensions, parametrized by N_{Param} well defined parameters P_i . The pseudo-data set is then a set of N_{Events} events that is characterized by the distribution of the PDF in all N_{Dim} variables.

A toy-MC test is conducted by generating N_{Toy} pseudo-data sets, and using those as input for the fitting framework to be tested. From the maximum likelihood estimates \hat{P}_i of the N_{Param} parameters P_i , the known injected parameter P_i^{Truth} and the respective error estimates $\hat{\sigma}_{P_i}$ one can calculate the *standard score*

$$z(P_i) = \frac{\hat{P}_i - P_i^{Truth}}{\hat{\sigma}_{P_i}}, \quad (8.1)$$

individually for each toy experiment and for each free fit parameter. The statistical properties of the distribution of the standard scores (commonly also referred to as *pull distribution*) of all N_{Toy} experiments reflect any bias arising from the fit and the reliability of the returned error estimates. The distribution of the standard scores of all generated pseudo-data sets can be fit by a gaussian $G = G(\mu_z, \sigma_z)$, individually for all parameters. In the limit of $N_{Toy} \rightarrow \infty$, the distribution of the standard scores should reflect a gaussian distribution with $\mu_z = 0$ and $\sigma_z = 1$, if there is no bias and the errors are correctly estimated [48].

As only a finite number of toys can be generated and processed, the deviations from the expected characteristics of the distribution of the standard scores can be judged in terms of significance. The gaussian fit to the standard scores returns error estimates on μ_z and σ_z (σ_{μ_z} and σ_{σ_z}) which mostly depend on N_{Toy} . A significant deviation of the mean from 0 indicates either a bias of the returned parameter estimate, or a asymmetrically wrong error estimate. A significant deviation of σ_z from 1 reflects unreliable error estimates. If σ_z is significantly larger (smaller) than one, the errors are, on average, underestimated (overestimated). Figure 8.1 shows an example of fitted λ_{ϑ}^{HX} parameter and standard score distributions for a specific bin from the polar asymmetry study (see discussion below).

8.1.2 Application to Polarization Analysis

Several toy-MC tests have been developed and conducted for various purposes, in various levels of complexity. In the standard configuration, all those tests employ MIGRAD as minimization algorithm and HESSE for the error estimation, MINOS has also been studied though. The first implementation was made to study convergence problems of MINUIT. As these problems have been solved by changing the method of the internal numeric integration method of RooFit, these toy-MC tests will not be discussed.

The particular toy-MC test developed and conducted to test the baseline fitting framework for the J/ψ polarization analysis will now be described in detail. For each kinematic cell, and both frames individually, $N_{Toy} = 200$ pseudo-data sets are drawn from the total composite PDF introduced by Eq. 7.33 in $N_{Dim} = 2$ dimensions $(\cos \vartheta, \varphi)$, characterized by $N_{Param} = 8$ parameters $P_i = \{\lambda_{\vartheta}^{PR}, \tilde{\lambda}^{PR}, \lambda_{\vartheta\varphi}^{PR}, \lambda_{\vartheta}^{NP}, \tilde{\lambda}^{NP}, \lambda_{\vartheta\varphi}^{NP}, f_{NP}^{(PRS)}, f_{NP}^{(NPS)}\}$. The term describing the background in Eq. 7.33 is neglected, and therefore all background related terms in the log-likelihood, described in Eq. 7.36, are neglected as well. Therefore, this toy-MC test cannot validate the background treatment in the likelihood, but presents a very effective test of the separate extraction of possibly very different prompt and non-prompt polarization parameters. In short, this toy-MC

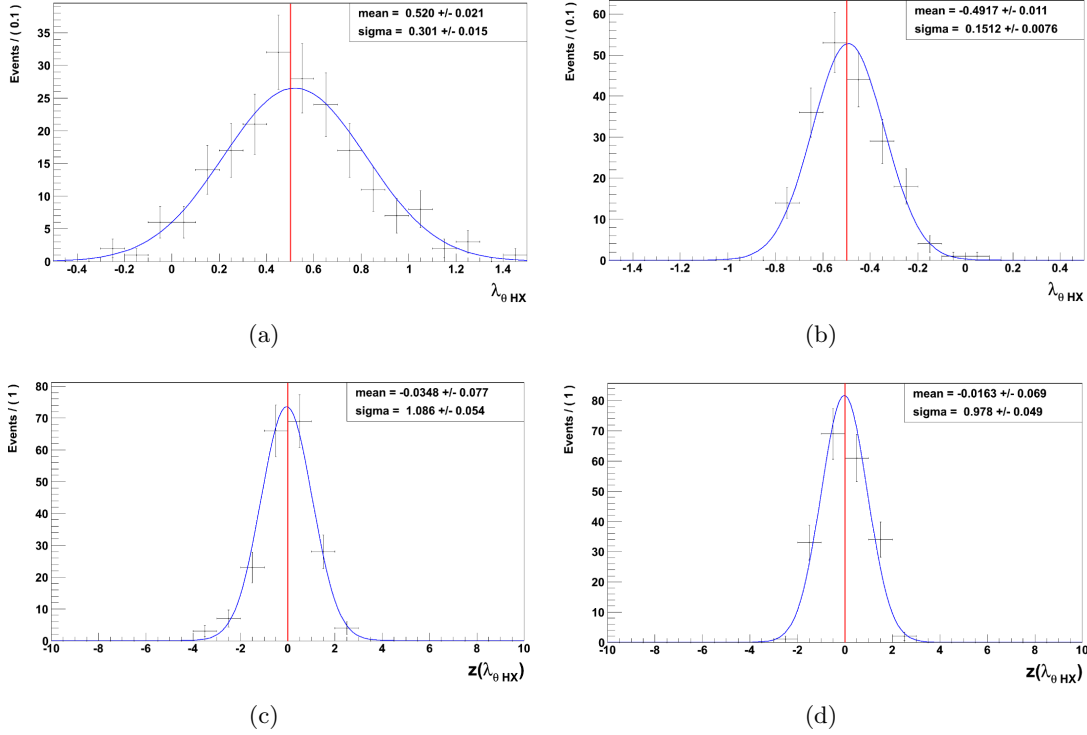


Figure 8.1: Toy-MC study of λ_{θ}^{HX} in the polar asymmetry scenario in bin $0.9 < |y| < 1.2$, $20 < p_T < 30$ GeV. Parameter distributions: (a) $\lambda_{\theta}^{HX^{PR}}$, (b) $\lambda_{\theta}^{HX^{NP}}$. Distribution of the standard scores: (c) $z(\lambda_{\theta}^{HX^{PR}})$, (d) $z(\lambda_{\theta}^{HX^{NP}})$. All distributions are compared to the expected mean (red line). The ordinate represents the number of toys returning values in the respective bins.

study tests the second step of the two-step approach discussed in Sect. 7.5.4, omitting the background treatment.

Additionally to the angular variables $\cos\vartheta$ and φ , the pseudo-data sample has to include information about the decay length distribution. This is taken into account by assigning a flag to each event, stating whether the event belongs to the prompt or non-prompt signal region. The total number of events N_{Events} is chosen to be the number of signal events estimated from the data sample, in the respective kinematic bin, triggered by the DoubleMu trigger (Tab. 7.3). Furthermore, the b-fraction f_b is chosen according to the estimate from data (corresponding to the parameters $f_{NP}^{(PRS)}$ and $f_{NP}^{(NPS)}$, as extracted from data), to ensure a realistic fraction of the non-prompt sample.

Three physically very different and extreme polarization scenarios were tested with this toy-MC method (Tab. 8.1):

1. *Unpolarized scenario:* Both contributions are generated unpolarized.

	λ_{ϑ}^{PR}	$\tilde{\lambda}^{PR}$	$\lambda_{\vartheta\varphi}^{PR}$	λ_{ϑ}^{NP}	$\tilde{\lambda}^{NP}$	$\lambda_{\vartheta\varphi}^{NP}$
Unpolarized scenario	0	0	0	0	0	0
Polar asymmetry scenario	0.5	0.5	0	-0.5	-0.5	0
Azimuthal asymmetry scenario	0	3	0	0	-1	0

Table 8.1: Polarization scenarios tested with the toy-MC method.

2. *Polar asymmetry scenario:* The prompt component is transversely polarized ($\lambda_{\vartheta}^{PR} = 0.5$), the non-prompt component is longitudinally polarized ($\lambda_{\vartheta}^{NP} = -0.5$).
3. *Azimuthal asymmetry scenario:* The prompt component is generated with an azimuthal asymmetry ($\tilde{\lambda}^{PR} = 3$, corresponding to $\lambda_{\varphi}^{PR} = 0.5$). The non-prompt component is generated with $\tilde{\lambda}^{NP} = -1$, corresponding to $\lambda_{\varphi}^{NP} = -0.5$. This case is a physically extreme case, as both contributions have polarization properties that correspond to a boundary of the positivity constraints (Fig. 5.8). Testing this scenario is a useful exercise for validation purposes but one does not expect to measure $\tilde{\lambda} > 1$, at least not within the context of SM physics.

These toy-MC tests are further used to estimate the discrimination power of several polarization scenarios, that are based on the CDF J/ψ polarization measurement, with a measurement at CMS (see Sect. 6.2.3 for details and results).

8.1.3 Results of the Toy-MC Tests

Figure 8.2 compares fit results of one of the fits of the toy-MC study of the unpolarized scenario with the projections of the pseudo-data on $\cos\vartheta$ and φ in both frames. The corresponding negative-log-likelihood function in the vicinity of the minimum found by MIGRAD is visualized in Fig. 8.3 with two-dimensional contour plots, comparing various polarization parameters. One clearly sees that the NLL is well behaved around the minimum and shows parabolic behavior. The NLL does not seem to indicate any local minima that could confuse the minimization algorithm.

In all scenarios, the differences between the average fitted and injected values of the parameters are far lower than the standard deviation of the fitted parameter distributions. The first two moments of the distribution of the standard scores for the unpolarized scenario are collected in Tab. 8.2 and Tab. 8.3. The values are compatible with those expected from a normal distribution. These results show that the fit converges to the correct minimum, and that the corresponding error estimates can be trusted. The non-prompt results of the unpolarized study, as well as the study of the polar asymmetry scenario show the same trends.

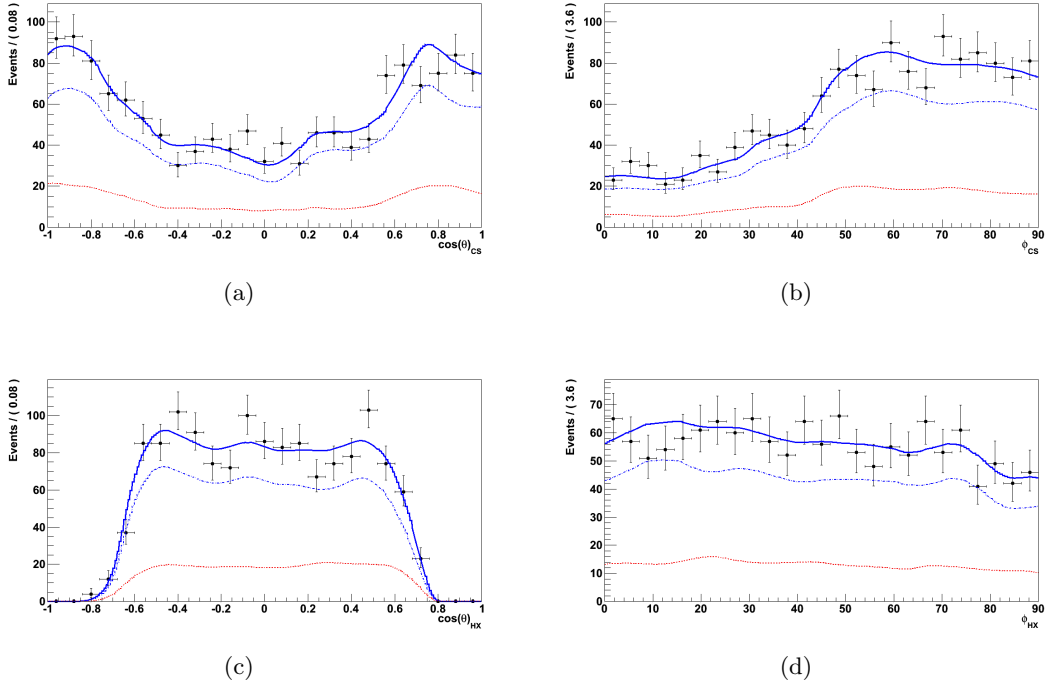


Figure 8.2: Examples of the distribution of unpolarized pseudo-data in $\cos \vartheta$ and φ in the prompt signal region in the bin $0.9 < |y| < 1.2$, $20 < p_T < 30$ GeV. The dotted red and the dotted blue lines correspond to the fitted contributions from non-prompt and prompt J/ψ 's, respectively. The solid blue line corresponds to the sum of the two contributions. (a) $\cos \vartheta$ in the CS frame, (b) φ in the CS frame, (c) $\cos \vartheta$ in the HX frame, (d) φ in the HX frame.

However, the distributions of the standard scores of the azimuthal asymmetry scenario indicate that the error estimation of HESSE cannot be trusted in this case. Keeping in mind the vicinity of the physical boundaries to this scenario, this finding is not very surprising. The log-likelihood function does not show parabolic behavior in the vicinity of the positivity constraints, therefore the estimation of the error matrix by the calculation of the second derivative at the minimum found by MIGRAD can not be reliable.

This study has shown that the fitting framework is able to correctly extract the injected polarization parameters in different polarization scenarios, and successfully differentiates between the prompt and non-prompt decay angular distributions, if sufficient information about the decay length distribution is provided.

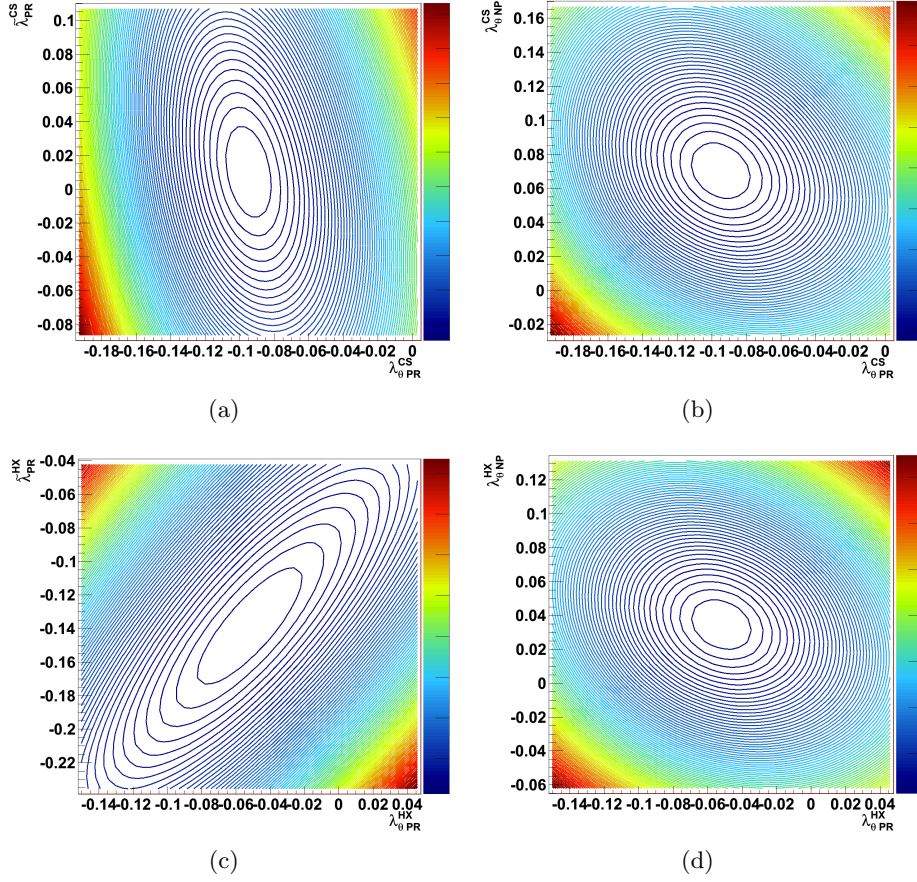


Figure 8.3: Negative-log-likelihood contours in arbitrary units, visualized in the vicinity of the found minimum, from one single fit of the toy-MC study of the unpolarized scenario in the bin $0.9 < |y| < 1.2$, $20 < p_T < 30$ GeV. (a) $\lambda_{\theta}^{CS PR}$ vs. $\tilde{\lambda}_{\theta}^{CS PR}$, (b) $\lambda_{\theta}^{CS PR}$ vs. $\lambda_{\theta}^{CS NP}$, (c) $\lambda_{\theta}^{HX PR}$ vs. $\tilde{\lambda}_{\theta}^{HX PR}$, (d) $\lambda_{\theta}^{HX PR}$ vs. $\lambda_{\theta}^{HX NP}$. The remaining four parameters are set constant to the estimated values at the minimum.

For the unpolarized case and the polar asymmetry scenario, also the uncertainties are correctly described. For large polarization, close to the physical boundaries of the parameters, the error estimation of HESSE is not reliable.

8.2 Monte Carlo Consistency Test

While the toy-MC method assumes a perfect description of acceptance and efficiency, the MC consistency test can detect any inconsistencies of the acceptance and efficiency determination, as well as their treatment in the likelihood. The idea of the MC consistency test is very simple, though it is a very powerful tool.

$ y $	p_T [GeV]	$\mu_{z(\lambda_\vartheta)}$	$\mu_{z(\tilde{\lambda})}$	$\mu_{z(\lambda_{\vartheta\varphi})}$
HX frame				
0.0–0.9	15–20	-0.1199 ± 0.0687	-0.1277 ± 0.0712	0.2433 ± 0.0723
0.0–0.9	20–30	-0.3626 ± 0.0790	-0.3757 ± 0.0756	0.0398 ± 0.0755
0.9–1.2	10–15	0.0417 ± 0.0722	0.0158 ± 0.0715	0.0475 ± 0.0729
0.9–1.2	15–20	-0.0658 ± 0.0683	-0.0851 ± 0.0717	0.0341 ± 0.0663
0.9–1.2	20–30	-0.1324 ± 0.0721	-0.0791 ± 0.0725	-0.0352 ± 0.0713
CS frame				
0.0–0.9	15–20	-0.1472 ± 0.0751	-0.0143 ± 0.0738	0.0634 ± 0.0731
0.0–0.9	20–30	-0.1086 ± 0.0746	0.0821 ± 0.0702	-0.0607 ± 0.0671
0.9–1.2	10–15	-0.0489 ± 0.0736	0.0176 ± 0.0728	-0.0348 ± 0.0722
0.9–1.2	15–20	0.0826 ± 0.0687	-0.1772 ± 0.0676	0.0977 ± 0.0685
0.9–1.2	20–30	0.0005 ± 0.0685	-0.0411 ± 0.0687	0.1000 ± 0.0711

Table 8.2: Mean of the distribution of the standard score $z(\lambda_i)$ for the unpolarized toy-MC study.

$ y $	p_T [GeV]	$\sigma_{z(\lambda_\vartheta)}$	$\sigma_{z(\tilde{\lambda})}$	$\sigma_{z(\lambda_{\vartheta\varphi})}$
HX frame				
0.0–0.9	15–20	0.9465 ± 0.0486	0.9816 ± 0.0504	0.9966 ± 0.0511
0.0–0.9	20–30	1.1170 ± 0.0559	1.0691 ± 0.0535	1.0672 ± 0.0534
0.9–1.2	10–15	1.0211 ± 0.0511	1.0108 ± 0.0505	1.0310 ± 0.0515
0.9–1.2	15–20	0.9662 ± 0.0483	1.0138 ± 0.0507	0.9372 ± 0.0469
0.9–1.2	20–30	1.0142 ± 0.0510	1.0203 ± 0.0513	1.0031 ± 0.0504
CS frame				
0.0–0.9	15–20	1.0355 ± 0.0531	1.0176 ± 0.0522	1.0074 ± 0.0517
0.0–0.9	20–30	1.0548 ± 0.0527	0.9922 ± 0.0496	0.9486 ± 0.0474
0.9–1.2	10–15	1.0405 ± 0.0520	1.0293 ± 0.0515	1.0213 ± 0.0511
0.9–1.2	15–20	0.9720 ± 0.0486	0.9564 ± 0.0478	0.9692 ± 0.0485
0.9–1.2	20–30	0.9662 ± 0.0484	0.9690 ± 0.0486	1.0036 ± 0.0503

Table 8.3: R.m.s. of the distribution of the standard score $z(\lambda_i)$ for the unpolarized toy-MC study.

The Fall10 MC sample, characterized by the generated polarization, is used as input for the polarization fitting framework. The geometrical acceptance, reconstruction and trigger efficiencies are determined according to Sects. 7.2.5 and 7.3. With this input, the polarization parameters can be extracted for each frame and in each kinematic bin, and then compared to the generated polarization of the MC samples.

The prompt Fall10 MC sample is generated unpolarized, while the individual contributions to the non-prompt Fall10 samples ($B^+ \rightarrow J/\psi \rightarrow \mu^+\mu^-$, $B_s \rightarrow J/\psi \rightarrow \mu^+\mu^-$, $B^0 \rightarrow J/\psi \rightarrow \mu^+\mu^-$ and $\Lambda_b \rightarrow J/\psi \rightarrow \mu^+\mu^-$) are polarized as measured by the

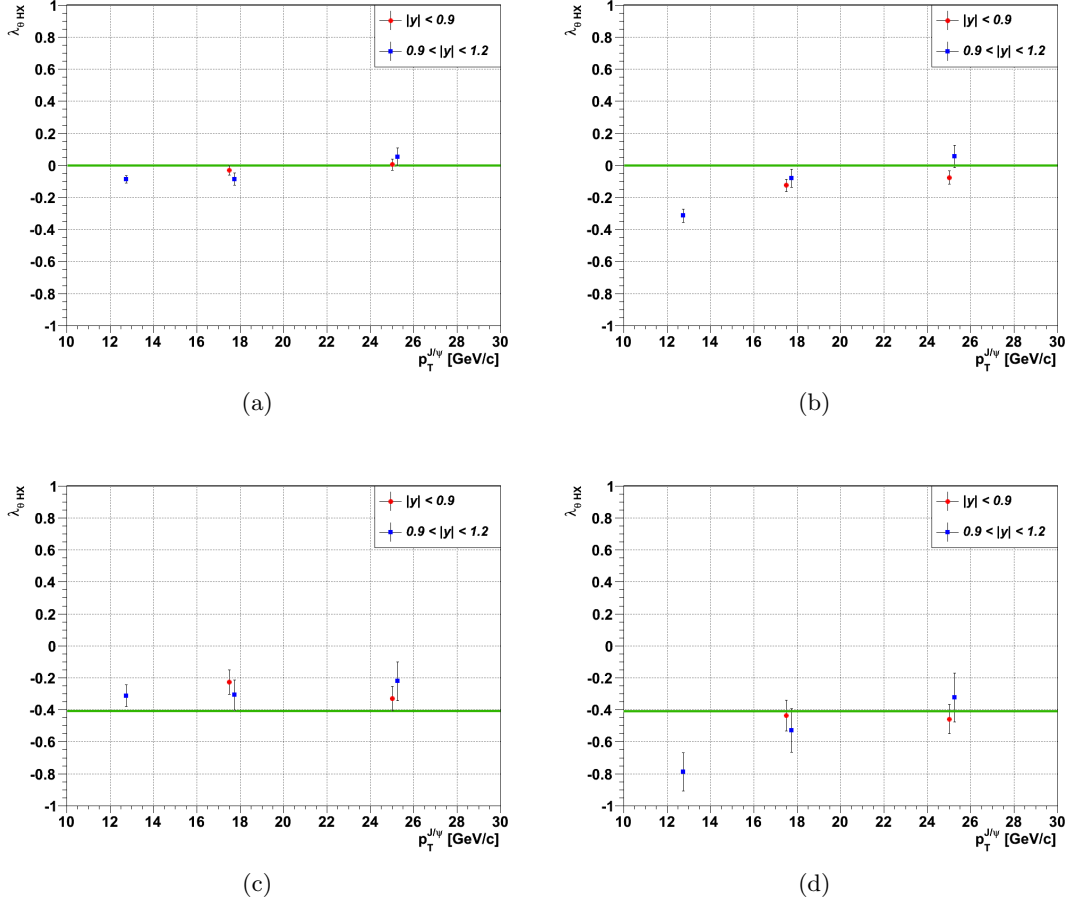


Figure 8.4: Results of the MC consistency tests - λ_g^{HX} vs. p_T for the prompt reconstruction level test (a), the prompt trigger level test (b), the non-prompt reconstruction level test (c) and the non-prompt trigger level test (d). The green lines indicate the generated polarization of the samples.

BaBar experiment at the Stanford Linear Accelerator Center with a polar asymmetry of $\lambda_g^{HX} = -0.41$, induced in the HX frame, without any kinematic dependence [49]. However, due to statistical fluctuations, the average polarization of the low statistics non-prompt sample may differ from the true value.

In the MC consistency tests, the prompt and non-prompt Fall10 MC samples are treated separately, without any background contributions. Therefore, in the MC consistency test of the prompt (non-prompt) sample, the corresponding terms describing the PDF of the background and non-prompt (prompt) contributions in Eq. 7.33 are neglected. The MC consistency test is conducted on two levels, to study the influence

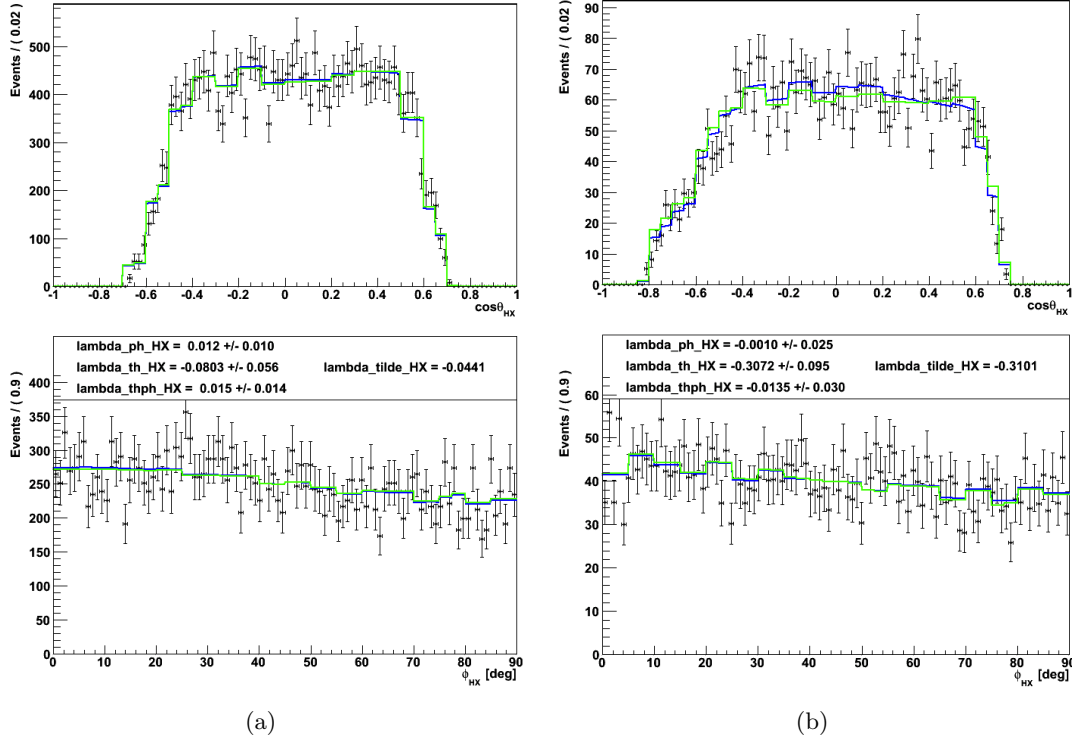


Figure 8.5: Distribution of the (a) prompt and (b) non-prompt Fall10 MC sample in $\cos \vartheta$ and φ in the HX frame together with the fit results of the MC consistency test in the bin $0.9 < |y| < 1.2$, $15 < p_{\text{T}} < 20$ GeV. The green lines represent the unpolarized model, the blue lines correspond to the fit results. (a) shows the prompt trigger level test, (b) shows the non-prompt reconstruction level test.

of the DoubleMu trigger efficiencies:

- *Reconstruction level:* In these tests, the trigger efficiencies are omitted. Therefore, the Fall10 events used in these tests are not required to fire the trigger. The decay angular distribution model contains the reconstruction efficiency maps and the geometrical acceptance maps.
- *Trigger level:* In these tests, the full detector description is used, including the trigger simulation of the Fall10 sample. As the events are required to fulfill the trigger requirements, the number of events in the respective kinematic bins is significantly smaller than in the reconstruction level tests. The model contains the trigger efficiency maps, the reconstruction efficiency maps and the geometrical acceptance maps.

Figure 8.4 shows results of λ_{ϑ}^{HX} vs. p_T for the prompt and non prompt trigger level and reconstruction level tests. Projections on $\cos\vartheta$ and φ of corresponding fits, for the cell $0.9 < |y| < 1.2$, $15 < p_T < 20$ GeV are shown in Fig. 8.5.

All reconstruction level tests show compatible results with the expected polarization, which indicates correct determination and treatment of the geometrical acceptance maps and the reconstruction efficiency maps. With the exception of the lowest p_T bin at forward rapidity ($0.9 < |y| < 1.2$, $10 < p_T < 15$ GeV), the results of all trigger level tests also show compatible results. This indicates correct determination and treatment of the trigger efficiency maps, with exception of the mentioned bin, which indicates problems in the trigger simulation in the respective kinematic region. This specific bin has also been identified as problematic with the test of rotational invariance, previously discussed. This fact shows that the tools developed to check the validity of the framework are very effective.

8.3 Evaluation of Systematic Effects

This section summarizes the tests that were conducted in order to estimate the systematic uncertainties on the polarization parameters, individually for all kinematic bins. As no results have been published so far, this section only serves as an indication of the order of magnitude of the individual sources of systematic effects. Besides the very important check of rotational invariance by comparing the extracted frame-invariant parameters obtained from different reference frames, which can detect unaccounted systematic effects of any unidentified part of the framework, these individual sources can be classified in four categories, which are individually discussed.

Uncertainties due to Fit Method

Toy-MC tests can be used as a very effective tool to estimate systematic errors arising from the fitting procedure itself. Significant deviations of the mean of the extracted likelihood estimates from the injected values of the parameters can be assigned as systematic error. These deviations are found to be very small.

Additionally, comparisons of the results extracted with MCMC methods with results obtained by the maximum likelihood method using MIGRAD/HESSE show that the central values remain unchanged, whereas the error estimates show small changes.

Uncertainties due to Separation of Prompt and Non-Prompt J/ψ 's

Besides the very effective test comparing the b-fraction results with existing measurements, two further tests have been conducted to estimate systematic uncertainties arising from the separation of the prompt and non-prompt J/ψ components. Both tests are conducted by additionally extracting the polarization from data under changed conditions and through the comparison with the baseline results.

The first test assumes that there is no prompt contribution in the non-prompt signal region ($n_{PR}^{(NPS)} = 0$), which neither significantly changes the results nor the error estimates. The second test allows the fractions of non-prompt and background components in the individual regions, obtained from the dimuon mass/decay length fitting step, to float in the polarization fit. The central value remains unchanged, while the error estimate increases by $\sim 10\%$. This can be assigned as systematic error.

Uncertainties due to Acceptance and Efficiency Determination

The MC consistency test allows us to assign a systematic uncertainty on the overall treatment of the acceptance and efficiency. Several further tests have been conducted to study the effects introduced by various sources changing the acceptance and efficiency maps.

As the acceptance and efficiency maps show large statistical fluctuations, the influence of smoothing algorithms was tested. Two smoothing algorithms are employed in different tests, P-spline smoothing and a linear smoothing algorithm, internally used in the RooFit package. Figs. 7.8 and 8.2 show examples of decay angular distribution PDFs (projected on $\cos\vartheta$ and φ) that are based on unsmoothed and smoothed maps, respectively. The unsmoothed maps are used for the generation of the toy-MC pseudo-data sets which are fit by a smoothed model (and vice versa) to study the effect of statistical fluctuations. Furthermore, the extraction of the polarization parameters from data is conducted separately with smoothed and unsmoothed maps. None of these tests have shown significant deviations of the central values or of the error estimates.

As the evaluation of the acceptance and efficiency maps depends on models describing the p_T distribution of the data sample, tests imposing different p_T distributions have been conducted. Different sets of maps are generated, for the prompt and non-prompt components, with three sets of p_T distributions. Figure 8.6 (a) shows the p_T distributions obtained by parametrizing results of the ATLAS experiment, and from simulations of PYTHIA and CASCADE MC event generators. Figure 8.6 (b) shows the difference of the set of distributions obtained from ATLAS results, for the prompt and the non-prompt component [39].

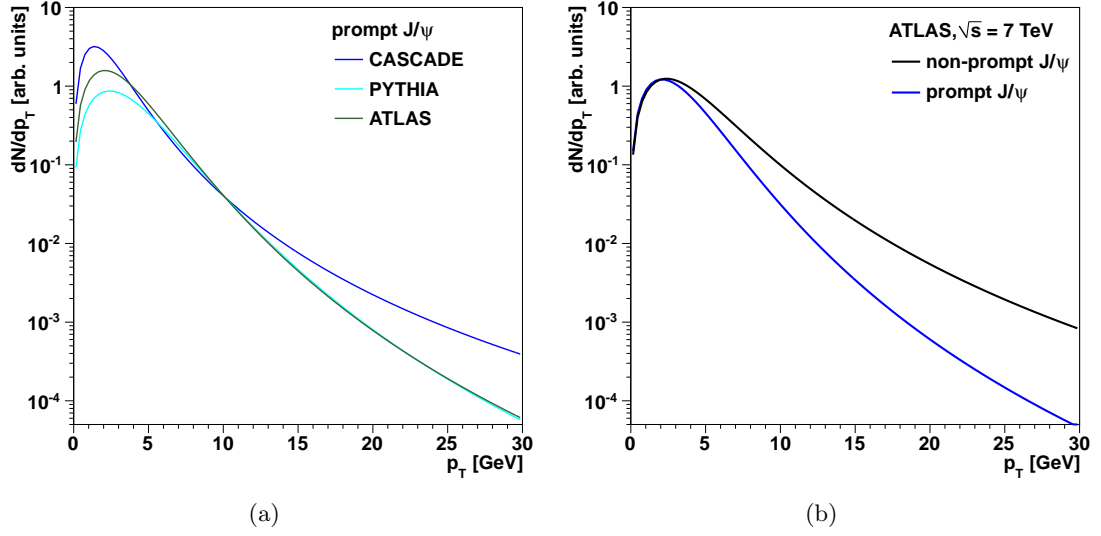


Figure 8.6: (a) p_T distributions obtained by parametrizing ATLAS, PYTHIA and CASCADE distributions of the prompt component. (b) Prompt and non-prompt p_T distributions obtained from ATLAS results [39].

The tests were conducted by generating toy-MC pseudo-data samples based on PYTHIA distributions, fitting with a model based on CASCADE distributions (and vice versa). Furthermore, the extraction of the polarization parameters from real data was conducted additionally under the assumption that the prompt and non-prompt p_T distributions are identical. These tests have shown that the unknown p_T distribution can affect the polar asymmetry parameter λ_θ by a bias of the order of 0.1, in the worst cases.

Uncertainties due to Background Treatment

The background contribution to the data sample is below 5% in all kinematic bins. However, despite the high S/B ratio, an anomalous background polarization could alter the measurement of the signal contributions. Projections of data from the individual SB regions on $\cos\vartheta$ and φ are compared to expectations, corresponding to extreme polarization scenarios. Figure 8.7 shows examples of such comparisons in the LSB region for both frames. This figure clearly shows that this test is much more sensitive in the CS frame than in the HX frame. From these tests one can conclude that the background contribution does not show any anomalous polarization. Hence, the background-related systematic uncertainties are expected to be very small.

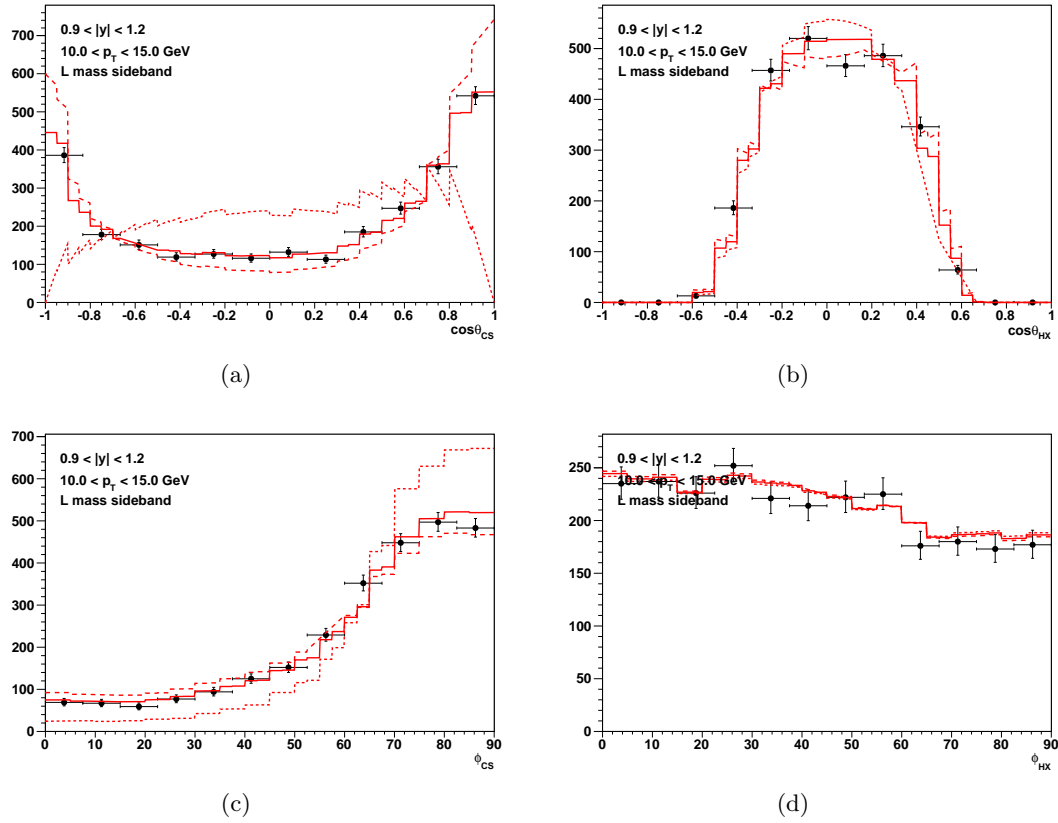


Figure 8.7: Distributions of data in the left mass sideband on the variables (a) $\cos \vartheta$ in the CS frame, (a) $\cos \vartheta$ in the HX frame, (a) φ in the CS frame, (a) φ in the HX frame in the bin $0.9 < |y| < 1.2$, $10 < p_T < 15$ GeV. The lines shown in the $\cos \vartheta$ projections correspond to $\lambda_\theta = +1$ (dashed), 0 (solid) and -1 (dotted) and $\lambda_\varphi = \lambda_{\vartheta\varphi} = 0$. The lines shown in the φ projections correspond to scenarios with $\lambda_\varphi = +0.5$ (dashed), 0 (solid) and -0.5 (dotted) and $\lambda_\theta = \lambda_{\vartheta\varphi} = 0$ [39].

8.4 Summary

A broad range of tools has been developed to confirm the validity of results obtained by the baseline analysis strategy described in Chap. 7. The first step of the fitting procedure, the two-dimensional mass and decay length fit, can be validated by comparison of the by-product result of the b-fraction with existing measurements. The second step, the polarization fit to the decay angular distribution can be validated by the toy-MC framework. The efficiency and acceptance treatment can be validated by MC consistency tests.

Several sources of systematic uncertainties have been studied in detail. Those sources include effects arising from the fitting framework itself, effects due to the separation of

prompt and non-prompt J/ψ components, effects due to the acceptance and efficiency evaluation, as well as effects from the background treatment. Furthermore, the check of rotational invariance with the frame-invariant formalism detects any inconsistencies due to other sources of systematic effects, that are not taken into account in the analysis framework.

Despite the fact that all those checks confirmed the analysis procedure, the baseline framework had to be further developed, which will be motivated and discussed in the following chapter.

Chapter 9

The Optimized Approach

The baseline method described in Chap. 7 had to be further developed in order to solve certain problems that were encountered and to avoid MC dependencies. This chapter describes the optimized method of a measurement of J/ψ polarization properties at CMS, which will be applied to data collected in 2010 and 2011, using a data sample with significantly increased statistics.

9.1 Overview and Motivation

It is a general aim of the CMS collaboration to reduce the dependence of any measurement on MC simulations as much as reasonably possible. Therefore, a data driven method of the evaluation of detector efficiencies has been developed (Sect. 9.2), which is implemented in the optimized framework and constitutes a substantial change with respect to the baseline method.

The so-called *turn on curves* of the efficiencies are very difficult to appropriately describe. This concerns regions of low p_T of the single muons, where the efficiency gradually increases with p_T . This problem can be approached by stricter cuts on the single muons (Sect. 9.3), to avoid the regions in phase space that cause problems.

The approach of geometrical acceptance and efficiency treatment in the baseline method, which is applied in terms of dimuon variables $\cos\vartheta$ and φ , introduces a model dependence, as a certain dimuon p_T and $|y|$ distribution has to be assumed. Furthermore, as the corrections are applied in coarse bins of $\cos\vartheta$ and φ , kinematic smearing effects are introduced. The significance of these effects is difficult to estimate. Therefore, a new approach has been developed. The optimized approach chooses to treat the efficiency correction on a single muon basis, applying weights to the individual events.

These weights are evaluated according to kinematic variables of both single muons. This approach avoids the problems of model dependence and kinematic smearing effects.

A detailed study of the trigger simulation of the DoubleMu trigger showed that the trigger introduces certain correlation effects between the two muons that cannot be described in terms of single muon efficiencies and require corrections that can only be obtained by MC (Sect. 9.2.2). In order to avoid this MC dependence, the low p_T trigger is favored.

These major changes with respect to the baseline method are described in detail in the following sections. Further minor changes are summarized in Sect. 9.5.

9.2 Data Driven Efficiency Determination

This section explains the dimuon efficiency factorization in single muon efficiencies, and how those can be evaluated by data driven methods, focussing on the low p_T trigger.

The efficiency of a dimuon event $\epsilon_{\mu\mu}$ is assumed to be factorizable into the single muon efficiencies. This proposition is further discussed in the section discussing the ρ -factor (see below). As in case of the dimuon efficiencies (Sect. 7.3), the single muon efficiencies can also be further factorized in the *reconstruction efficiency* ϵ_{reco} and the *trigger efficiency* ϵ_{trig} . As the low p_T trigger combines two different types of muons, the trigger efficiencies have to be evaluated individually, for the HLT muon μ^{HLT} and for the tracker muon μ^{TM} (μ^{HLT} and μ^{TM} stand for the identification of the muon as HLT or tracker muon and the muon kinematic variables p_T and $|\eta|$). The reconstruction efficiencies also have to be evaluated separately for μ^{HLT} and μ^{TM} .

The dimuon efficiency then reads

$$\epsilon_{\mu\mu} = \epsilon(\mu^{HLT}) \cdot \epsilon(\mu^{TM}), \quad (9.1)$$

with the single muon efficiencies of the μ^{HLT} and the μ^{TM}

$$\begin{aligned} \epsilon(\mu^{HLT}) &= \epsilon_{reco}(\mu^{HLT}) \cdot \epsilon_{trig}(\mu^{HLT}), \\ \epsilon(\mu^{TM}) &= \epsilon_{reco}(\mu^{TM}) \cdot \epsilon_{trig}(\mu^{TM}). \end{aligned} \quad (9.2)$$

The reconstruction efficiency can be further factorized to

$$\begin{aligned} \epsilon_{reco}(\mu^{HLT}) &= \epsilon_{track} \cdot \epsilon_{MuonID}(\mu^{HLT}) \cdot \epsilon_{MuonQual}(\mu^{HLT}), \\ \epsilon_{reco}(\mu^{TM}) &= \epsilon_{track} \cdot \epsilon_{MuonID}(\mu^{TM}) \cdot \epsilon_{MuonQual}(\mu^{TM}). \end{aligned} \quad (9.3)$$

ϵ_{track} describes the offline tracking efficiency (which is the same for μ^{HLT} and μ^{TM}),

ϵ_{MuonID} the efficiency of muon identification and $\epsilon_{\text{MuonQual}}$ the efficiency due to the muon quality cuts. The trigger efficiency can be factorized in

$$\begin{aligned}\epsilon_{\text{trig}}(\mu^{\text{HLT}}) &= \epsilon_{L1L2}(\mu^{\text{HLT}}) \cdot \epsilon_{L3}(\mu^{\text{HLT}}), \\ \epsilon_{\text{trig}}(\mu^{\text{TM}}) &= \epsilon_{TM1}(\mu^{\text{TM}}) \cdot \epsilon_{TM2}(\mu^{\text{TM}}).\end{aligned}\tag{9.4}$$

ϵ_{L1L2} is the Level 1 and Level 2 trigger efficiency, ϵ_{L3} the Level 3 trigger efficiency. ϵ_{TM1} is the online tracking efficiency and ϵ_{TM2} is the efficiency of a track to be converted into a tracker muon.

One should keep in mind that all mentioned sub-efficiencies are dependent on the single muon p_T and $|\eta|$. The individual efficiencies have therefore to be studied in detail in terms of these kinematical dependencies. Furthermore, the efficiencies depend on the individual run periods, due to different trigger conditions, and on the definition of the fiducial cuts.

In this analysis, μ^{HLT} is defined as the muon with the higher p_T , μ^{TM} being the muon with the lower p_T . After evaluating the individual efficiencies for the specific single muon p_T and $|\eta|$, combining them with Eqs. 9.1, 9.2, 9.3 and 9.4, one obtains the dimuon efficiency of the given event.

The kinematic dependencies of the individual efficiencies are evaluated by the data driven *tag and probe* method, which will now be briefly discussed.

9.2.1 The Tag and Probe Method

Efficiency calculations are only correct, if the objects considered are free from background. With the tag and probe method signal and background event yields can be estimated via a fitting procedure. This data driven method is using dimuon resonances such as the Z, the Υ or the J/ψ , which are reconstructed from a pair of two muon objects to measure any single muon efficiency. One muon is passing a tight identification (tag), the other muon is passing a loose identification (probe). The conditions of the passing probe define the efficiency to be measured [50].

Separate data sets are produced, one with dimuon events combining the tag muons and the passing probe muons, the other one combining the tag muons and the failing probe muons. These datasets are then fit according to a certain model describing signal and background contributions [50].

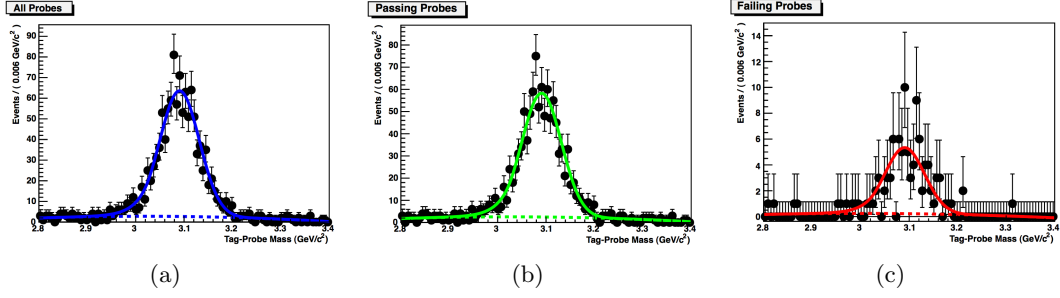


Figure 9.1: Example of a tag and probe fit for the evaluation of the L1/L2 trigger efficiency corresponding to $\epsilon_{L1L2} = 0.92 \pm 0.01$. The dimuon mass distribution of the tag and probe muons is shown for (a) all probes, (b) the passing probes and (c) the failing probes [51].

The efficiency is then defined as

$$\epsilon = \frac{N_{pass}}{N_{pass} + N_{fail}}, \quad (9.5)$$

with the number of estimated signal events in the passing probe data set (N_{pass}) and the number of estimated signal events in the failing probe data set (N_{fail}). Figure 9.1 shows an example of such a fit.

This efficiency evaluation can be conducted as function of any variable and binning, as long as there is enough statistics in the bins to conduct the fit.

9.2.2 The ρ -Factor

It is not *a priori* clear that the factorization approach of Eq. 9.1 is correct. In some trigger configurations (such as the DoubleMu trigger) the factorization of the dimuon efficiency in the product of the single muon efficiencies is not justified, as there are correlations between the two muons that enter in the dimuon efficiency but are not measurable with the tag and probe method, as the tag and probe method can only measure single muon efficiencies.

These correlations can be taken into account by multiplying Eq. 9.1 with a correction factor, the ρ -factor. The dimuon efficiency then reads

$$\epsilon'_{\mu\mu} = \epsilon(\mu^{HLT}) \cdot \epsilon(\mu^{TM}) \cdot \rho(\mu^{HLT}, \mu^{TM}) \quad (9.6)$$

with $\rho(\mu^{HLT}, \mu^{TM})$ depending on the single muon kinematics of both muons, hence being better referred to as ρ -function. The ρ -function can only be evaluated by MC and is

defined by

$$\rho(\mu^{HLT}, \mu^{TM}) = \frac{\epsilon_{\mu\mu}^{MC_{Truth}}}{\epsilon^{MC_{T\&P}}(\mu^{HLT}) \cdot \epsilon^{MC_{T\&P}}(\mu^{TM})}, \quad (9.7)$$

with $\epsilon_{\mu\mu}^{MC_{Truth}}$ the dimuon efficiency evaluated from MC truth according to the method introduced in Sect. 7.3 and $\epsilon^{MC_{T\&P}}(\mu^{HLT}) \cdot \epsilon^{MC_{T\&P}}(\mu^{TM})$ the product of the single muon efficiencies evaluated from MC tag and probe.

In the polarization analysis the absolute value of the dimuon efficiency does not matter at all, as only the modulation of the efficiency with respect to $\cos \vartheta$ and φ enters in the extraction of the polarization parameters. It is of great importance to evaluate the ρ -function for the specific trigger setup. If one finds modulations in the function $\rho(\cos \vartheta, \varphi)$, it has to be taken into account as further correction to the data, and the analysis becomes MC dependent.

As the number of events in the Fall10 MC sample is too low to evaluate the ρ -function in dependence of $\cos \vartheta$ and φ in all kinematic bins individually, it is impossible to directly show that the ρ -function correction can be neglected in the analysis.

However, this can be shown indirectly, by evaluating the ρ -function independently for the dimuon kinematic variables p_T , $|y|$, $\cos \vartheta_{CS}$, φ_{CS} , $\cos \vartheta_{HX}$ and φ_{HX} . If this study shows that the ρ -function is flat in all those variables within errors, it can be neglected and the analysis can be conducted independent of MC simulations.

As was expected due to considerations concerning the trigger logic of the low p_T trigger, preliminary studies of the ρ -factor indicate that the ρ -function is flat in all relevant variables.

9.3 Fiducial Cuts

As discussed above, it is difficult to evaluate the kinematic dependence of the single muon efficiencies at low p_T . It has been considered useful to define stricter cuts, only accepting muons from a region in phase space well understood in terms of efficiencies.

These new fiducial cuts are defined so that the reconstruction efficiency of the Fall10 MC sample of accepted single muons never falls below 50%. These cuts are defined as function of muon p_T and $|\eta|$, individually for HLT muons and tracker muons, and are shown in Fig. 9.2 (a) and Fig. 9.2 (b). For cross checking purposes, a second set of fiducial cuts has been defined, which ensures that the reconstruction efficiency never falls below 80% (Fig. 9.2 (c) and (d)), called *tight cuts* in contrast to the set of *loose cuts* discussed above. Additionally, all single muons with $p_T < 3$ GeV are rejected.

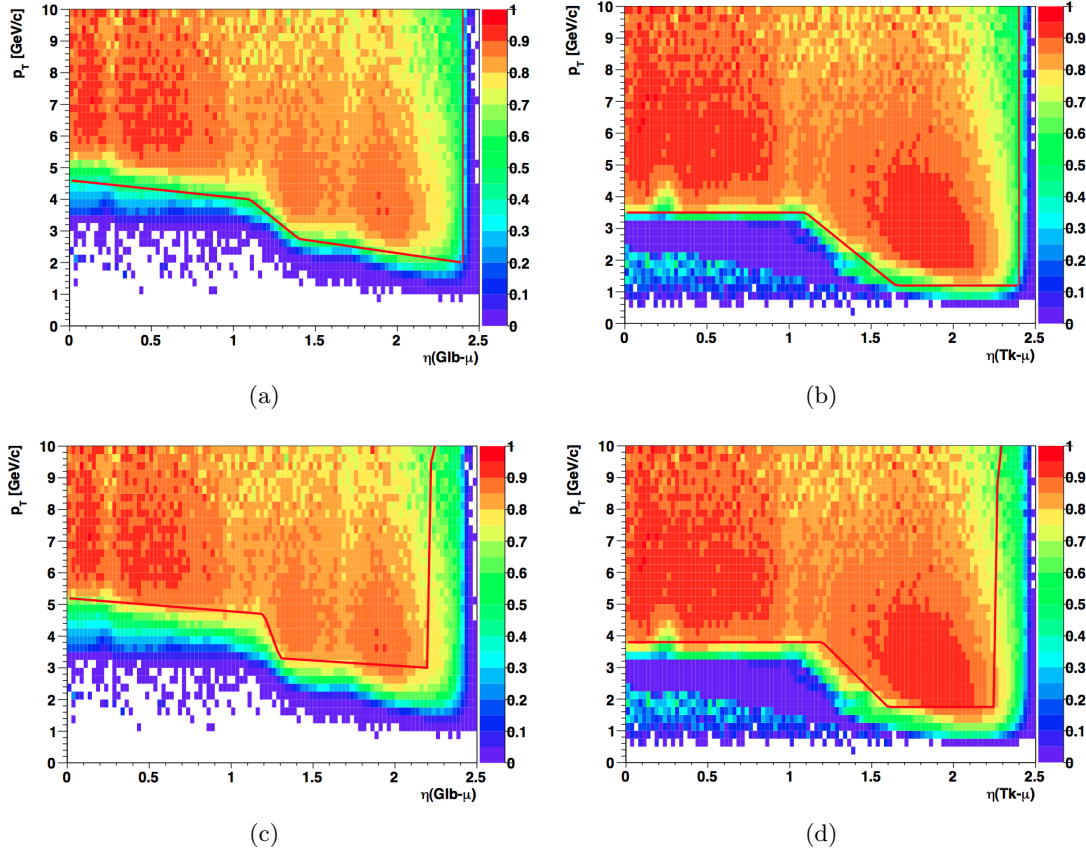


Figure 9.2: Sets of loose fiducial cuts (indicated by the red line) defined for the HLT muon (a) and the tracker muon (b), based on the Fall10 MC reconstruction efficiency. Sets of tight fiducial cuts defined for the HLT muon (c) and the tracker muon (d).

9.4 The Likelihood of the Optimized Method

The dimuon efficiency of a given event is computed as the product of the single muon efficiencies for the given p_T and $|\eta|$ of the two single muons according to Eq. 9.1. The weight

$$w^i = \frac{1}{\epsilon_{\mu\mu}^i} \quad (9.8)$$

is then assigned to each event so that the efficiency correction can be applied on an event-by-event basis, avoiding the kinematic smearing effects and model dependencies present in the baseline method.

The optimized approach combines the two-step fitting procedure previously discussed

to a four-dimensional simultaneous unbinned maximum likelihood fit in two ranges (signal and background region), omitting the distinction between the prompt and non-prompt signal region defined by a cut in the decay length variable $l_{J/\psi}$.

The PDF describing the decay angular distribution $P(\cos \vartheta, \varphi | \mathcal{P}, \mathcal{N})$, part of the four-dimensional PDF

$$\begin{aligned} & F_{4D}(m_{\mu\mu}, l_{J/\psi}, \cos \vartheta, \varphi | \mathcal{M}, \mathcal{L}, \mathcal{P}, \mathcal{N}) \\ &= M(m_{\mu\mu} | \mathcal{M}, \mathcal{N}) \cdot L(l_{J/\psi} | \mathcal{L}, \mathcal{N}) \cdot P(\cos \vartheta, \varphi | \mathcal{P}, \mathcal{N}), \end{aligned} \quad (9.9)$$

now simply reads

$$\begin{aligned} P(\cos \vartheta, \varphi | \mathcal{P}, \mathcal{N}) = & n_{PR} \cdot w_{PR}(\cos \vartheta, \varphi | \vec{\lambda}^{PR}) \\ & + n_{NP} \cdot w_{NP}(\cos \vartheta, \varphi | \vec{\lambda}^{NP}) \\ & + n_{Bkg} \cdot w_{Bkg}(\cos \vartheta, \varphi), \end{aligned} \quad (9.10)$$

with w_{PR} and w_{NP} introduced in Eq. 7.32 and w_{Bkg} introduced in Eq. 7.33. The PDFs describing the mass and decay length distributions remain identical to the baseline approach.

The weights w^i enter as factors in the total log-likelihood function, which can be written as

$$\begin{aligned} \log[L_{4D}(\mathcal{M}, \mathcal{L}, \mathcal{P}, \mathcal{N})] = & \sum_i \log[F_{4D}(m_{\mu\mu}^i, l_{J/\psi}^i, \cos \vartheta^i, \varphi^i | \mathcal{M}, \mathcal{L}, \mathcal{P}, \mathcal{N}) \cdot w^i] \\ & + \sum_j \log[F_{4D}(m_{\mu\mu}^j, l_{J/\psi}^j, \cos \vartheta^j, \varphi^j | \mathcal{M}, \mathcal{L}, \mathcal{P}, \mathcal{N}) \cdot w^j], \end{aligned} \quad (9.11)$$

with i and j the events in the signal region and the background region, respectively. The weights also affect the dimuon mass and decay length distributions. The effect on the returned parameters is estimated to be smaller than 1%, as the efficiency does not show significant dimuon mass or decay length dependencies.

This approach allows one to omit any acceptance corrections, as the acceptance is a pure step-function in terms of single muon variables p_T and $|\eta|$, as a dimuon event is either accepted by the fiducial cuts ($A_{\mu^+} \cdot A_{\mu^-} = 1$) or not ($A_{\mu^+} \cdot A_{\mu^-} = 0$). If the total likelihood is appropriately normalized to the region of accepted phase space, the acceptance can be neglected completely.

9.5 Summary of the Optimized Analysis Strategy

This section summarizes the further developments of the analysis framework and the changes with respect to the baseline method:

- The detector efficiencies of the single muons are evaluated individually by the data driven tag and probe method.
- To ensure that only events in phase space regions which are well under control are accepted, stricter fiducial cuts are defined. Two separate sets of cuts are defined for cross checking purposes.
- The two-step fitting procedure of the baseline method is combined to a one-step four-dimensional simultaneous unbinned maximum likelihood fit.
- The dimuon efficiencies are calculated as the product of the single muon efficiencies and are applied as weights to the individual events, which enter the log-likelihood function as factors.
- Acceptance corrections can be omitted completely in the new approach, if the likelihood is appropriately normalized.
- The measurement strategy is therefore completely MC independent.
- The measurement is model independent and effects of kinematic smearing as in the baseline method can be avoided.
- The folding in φ is no longer necessary due to the single muon efficiency correction approach.
- The low p_T trigger is used, as it is not expected to show modulations of the ρ -function in $\cos\vartheta$ and φ , in contrast to the DoubleMu trigger.
- Additionally to the cuts in the baseline method, cowboy dimuons are rejected due to inefficiencies that are not very well understood.
- The new J/ψ p_T and $|y|$ distributions (due to different fiducial cuts, different trigger settings and the cowboy dimuon cut) require new definitions of the kinematic bins.
- Due to stricter cuts, the total number of events entering the analysis is significantly lower with respect to the baseline method. This will be more than compensated by adding the 2011 data set to the analysis, which already has ~ 74 times the integrated luminosity of the 2010 data set, as of September 22nd 2011.

Chapter 10

Conclusions

10.1 Summary

After decades of research, the significance of the individual conceivable quarkonium production mechanisms is still not properly understood. The state-of-the-art of the theoretical tools to model the elementary mechanisms and contributions to quarkonium production have been summarized. The discussion has shown that existing differential cross section measurements and measurements of the spin alignment of quarkonia cannot be simultaneously described by those models.

The further measurements of the polarization properties of vector quarkonia profit from a recently developed formalism, which describes quarkonium polarization with a new approach, expanding earlier treatments to a two-dimensional problem, allowing to define the polarization state in terms of frame-invariant quantities. Experimental strategies following the propositions of this formalism will lead to results that can be interpreted unambiguously and can provide a large fraction of the information needed for the clarification of quarkonium production.

Published polarization measurements have been analyzed with a one-dimensional approach, leading to ambiguous measurements. This thesis reports possible interpretations of one measurement in particular, in terms of azimuthal asymmetry and frame-invariant quantities, providing predictions for a measurement at the CMS detector. Based on the estimated discrimination power, it will be possible to differentiate between various possible scenarios with a polarization measurement at CMS in certain kinematic regions.

The LHC provides excellent conditions to study quarkonium resonances. Moreover, the design of the CMS detector was specifically focussed on the efficient detection and reconstruction of muons in a broad kinematic range. This makes the CMS detector an ideal tool to study various properties of quarkonia in the dimuon decay channel.

The CMS polarization team has developed a physics analysis framework that is able to extract the polarization properties of the J/ψ , individually for the prompt contributions as well as for the contribution from the decay of b hadrons, differential in p_T and rapidity.

In order to avoid contradictory results as obtained in past measurements, several independent validation tools were developed and applied, to ensure that the results extracted are reliable. The baseline measurement framework discussed in this thesis is completed, and all necessary validation and systematic checks have led to the conclusion that the framework extracts reliable estimates of the polarization properties. Nevertheless, it was decided to prolong the project and not yet submit for publication, in order to be able to include data collected by CMS in 2011 and to further develop the analysis framework to avoid dependencies on Monte Carlo simulations.

This optimized analysis framework is not yet fully applicable, as certain validation tools have yet to be adapted to the requirements of the new approach. The framework will soon be ready to extract the J/ψ polarization properties and confirm the reliability of the results by various self-consistency checks. This will be the first rigorous and unambiguous determination of polar and azimuthal asymmetry parameters as well as frame-invariant parameters of J/ψ events produced in hadronic collisions at a center of mass energy of $\sqrt{s} = 7$ TeV.

10.2 Outlook

The next years of LHC physics will provide excellent conditions to conduct further measurements at the CMS detector, to clarify quarkonium production mechanisms. Many measurements are possible, such as the ψ' , $\Upsilon(nS)$, χ_{cj} and χ_{bj} states. The prospects of measurements in the charmonium and bottomonium systems in the near and medium term future are discussed below.

Charmonium System

Although no results have been published yet, the analysis presented in this thesis is a very important first step in the understanding of the charmonium system. The next step will be the application of the developed framework, conducting the J/ψ polarization measurement based on data collected by CMS in 2010 and 2011. Data collected in 2010 allows one to probe forward rapidity regions up to $|y| = 2.1$, while the data collected in 2011 will cover a kinematic range restricted to the barrel region, but up to much higher p_T . As a very flexible framework has been developed and many experimental challenges

have been solved, future measurements of the polarization properties of other states will be easier to conduct.

As previously discussed, it is very difficult to interpret the results of the prompt J/ψ polarization measurement in terms of properties of the directly produced J/ψ , as the unknown polarization of heavier charmonium states significantly influences the result of the prompt J/ψ measurement. Therefore, the polarization measurement of the ψ' will be approached very soon. The existing framework will have to be adjusted to the ψ' in order to account for the larger background and possibly different models of the decay length distributions due to different kinematics, to separate the feed-down of b hadron decays. As the ψ' does not suffer from feed-down contributions of the χ_c states, a ψ' polarization measurement will provide very useful information for the understanding of the underlying production mechanisms.

The next step will be the study of the decay of the P wave charmonium states via the decay into a J/ψ and a low energy photon $\chi_{cj} \rightarrow J/\psi \gamma \rightarrow \mu^+ \mu^- \gamma$. This will require dedicated reconstruction studies of the photon. After successful identification of the χ_{cj} states, the polarization of the state can be studied.

In parallel, differential cross section measurements and differential cross section ratio measurements will be conducted, for all the mentioned states.

Bottomonium System

The bottomonium system provides very interesting measurements given that, due to the higher mass of the beauty hadrons, the non-relativistic approach can be probed with higher accuracy. As there is no feed-down from b hadron decays in the bottomonium system, the decay length distribution does not have to be taken into account.

Measurements of the excited S wave states, the $\Upsilon(2S)$ and the $\Upsilon(3S)$ can be approached easily with the framework developed for the 1S state. The $\Upsilon(3S)$ is particularly interesting, as it is the heaviest bottomonium particle under the open beauty production threshold, and is therefore exclusively produced directly.

As the feed-down contributions from heavier bottomonium states is expected to be more significant than in the charmonium system, it is even more important to clarify the polarization properties of the χ_b states.

Similarly to the physics program of the charmonium sector, cross section measurements and cross section ratio measurements will be conducted in addition to the measurement of the respective spin alignment properties.

Final Considerations

In parallel to this broad quarkonium physics program of CMS, the other LHC experiments will conduct similar measurements of the charmonium and bottomonium systems. The first year of LHC quarkonium physics has shown that all experiments deliver compatible and complementary results, which has not always been the case in past collider experiments. While ATLAS and CMS can confirm each other as they probe very similar kinematic regions, ALICE and especially LHCb can gain information in complementary kinematic regions, at very forward rapidity.

After all the measurements summarized above will be successfully completed, the understanding of the underlying quarkonium production mechanisms will hopefully be significantly improved. The importance of the color octet contributions, as well as the individual color octet matrix elements, will possibly be properly understood. The quarkonium physics programs at CMS and at the other LHC experiments clearly have the potential to ultimately end the era of experimental and theoretical inconsistencies in quarkonium physics.

Appendix A

Acknowledgements

I want to express my gratitude to Chris Fabjan, who brought me in touch with high energy physics, introduced me to the standard model of particle physics, and gave me the opportunity to work on my diploma thesis in this field in the very interesting time of the LHC startup.

I also wish to thank Jozko Strauss, Wolfgang Adam, Rudolf Frühwirth and Herbert Rohringer for their guidance and many fruitful discussions that often resulted in solving one of the many puzzles on the way.

The whole HEPHY CMS analysis team, Chris Thomay, Wolfgang Kiesenhofer, Marc Dünser, Ilse Krätschmer, Florian Teischinger, Wolfgang Waltenberger, Robert Schöffbeck, Dietrich Liko and Edmund Widl - only to name a few - helped me find my way through the labyrinths of CMSSW, ROOT, RooFit, C++ and python coding.

I want to extend my thanks to my colleagues at CERN, Hermine Wöhri, Carlos Lourenço and Lindsey Gray, and from LIP Lisbon, Pietro Faccioli and João Seixas, with whom I worked together very closely. They gave me advice on a daily basis and managed to help me understand some of the crucial aspects of quarkonium polarization.

On a personal note, I want to thank my family, Katharina Knünz, Rudolf Knünz, Ida Wieser, Regina Knünz and Anna Wieser for their moral and financial support during my years at the university.

Furthermore, I want to extend my thanks to my card game companions, Bärbel Ausserer, Christoph Kutzer and Alex Lins and my (former) flatmates Lukas Weber, Paul Batruel and Markus Schwendinger, who managed to distract me many times after challenging physics adventures and made my time in Vienna a very amusing and pleasant stay.

Last but not least I want to thank the wonderful Regina Geisler for all her moral support, for her endurance, and for making even the most exhausting and frustrating days of physics analysis to days I will remember as beautiful.

Appendix B

Abstract

English Abstract

In march 2010, with the first proton-proton collisions at the LHC (Large Hadron Collider) at CERN (Geneva), a new era in high energy physics has been initiated. Besides searches for physics beyond the standard model, the LHC provides excellent conditions to study vector quarkonium production at the CMS (Compact Muon Solenoid) detector in the dimuon decay channel.

Quarkonia are bound states of a heavy quark (charm, beauty) and it's respective antiquark. The underlying elementary quarkonium production mechanisms are not yet satisfactorily understood, as several models have had no success in describing previous high energy hadronic collision results of differential cross sections and polarization properties of quarkonia simultaneously.

After an introduction to the LHC and the CMS detector, this thesis presents a review of the most favored models describing quarkonium production and a new formalism, describing the polarization properties of vector quarkonia, that was developed in recent years.

Benefitting from the findings of this new formalism, this thesis reports several interpretations of a published ambiguous J/ψ polarization measurement in terms of frame-invariant parameters, which leads to predictions for a polarization measurement at CMS. These predictions allow a CMS measurement to discriminate between these possible polarization scenarios.

This thesis reports the analysis strategy for the first unambiguous determination of the J/ψ polarization properties in proton-proton collisions at a center of mass energy of 7 TeV, measuring differential in transverse momentum and rapidity of the J/ψ , based on a data set collected by CMS. Results are obtained individually for prompt J/ψ contributions and J/ψ 's originating from the decay of b hadrons.

The aim of this measurement is to probe properties of QCD, that are expected to appear in certain kinematic regions of quarkonium production, indicated by the

polarization properties of the J/ψ . A better understanding of quarkonium production can help increasing the knowledge of hadroproduction in general.

Deutscher Abstrakt

Im März 2010 hat mit den ersten Proton-Proton Kollisionen am LHC (Large Hadron Collider) im Forschungszentrum CERN (Genf) eine neue Ära in der Hochenergiephysik begonnen. Neben der Suche nach direkten Hinweisen für eine notwendige Erweiterung des Standardmodells der Teilchenphysik werden Präzisionsmessungen der Parameter des Standardmodells durchgeführt. Der LHC bietet aufgrund der noch nie da gewesenen Schwerpunktsenergie der Kollisionen sowie der hohen Kollisionsrate exzellente Bedingungen, um die Produktion von Vektor Quarkonia, die in zwei Muonen zerfallen, am CMS (Compact Muon Solenoid) Experiment zu messen.

Quarkonia sind gebundene Zustände eines schweren Quarks (charm, beauty) und des zugehörigen Antiquarks. Die elementaren Produktionsmechanismen von Quarkonia können noch nicht zufriedenstellend erklärt werden, da die vorhandenen theoretischen Modelle im Versuch, bisherige Resultate in hadronischen Kollisionen von differentielltem Wirkungsquerschnitt und Polarisationsseigenschaften von Quarkonia gleichzeitig zu beschreiben, keinen Erfolg aufgewiesen haben.

Nach einer Einführung der Eigenschaften des LHC und des CMS Detektors behandelt diese Arbeit die wichtigsten Modelle, welche die Produktion von Quarkonia charakterisieren, und einen neu entwickelten Formalismus zur Beschreibung der Polarisationsseigenschaften von Quarkonia.

Dieser neue Formalismus wird in der vorliegenden Arbeit dazu genutzt, publizierte uneindeutige Resultate einer Polarisationsmessung auf verschiedene Weisen zu interpretieren, was zu Vorhersagen für eine Messung der Polarisationsseigenschaften des J/ψ am CMS führt. Dies ermöglicht eine Unterscheidung dieser Szenarien.

Diese Arbeit beschreibt die Strategie der ersten vollständigen Messung der Polarisation des J/ψ Mesons in Proton-Proton Kollisionen mit einer Schwerpunktsenergie von 7 TeV, differentiell in Rapidität und Transversalimpuls des J/ψ , basierend auf Daten gemessen am CMS Detektor. Für prompt produzierte J/ψ 's und jene, die vom Zerfall von b Hadronen stammen, wird die Polarisation separat aus den Daten extrahiert.

Das Ziel dieser Messung ist die Untersuchung von Eigenschaften der QCD, die in bestimmten kinematischen Regionen der Produktion von Quarkonia durch die Polarisation des J/ψ in Erscheinung treten. Eine bessere Kenntnis der Produktionsmechanismen von Quarkonia führt zu einem besseren Verständnis hadronischer Produktionsmechanismen im Allgemeinen.

Appendix C

Summary of Author's Contributions

The analysis strategy has undergone an evolution of developments and approaches to solve several problems. The learning-curve of the understanding of the experimental extraction of the polarization parameters of vector quarkonia in general has monotonically increased and resulted in the analysis strategy reported in this thesis.

I have been active in this evolution since april 2010, contributing in several parts of this analysis, profiting from the knowledge of and the collaboration with several people mentioned in Appendix A. This section intends to discriminate between the general efforts of the CMS polarization team and my individual contributions. One can differentiate between four phases during the evolution of the analysis. Following, the individual phases are briefly discussed, and my contributions in these phases are summarized.

Phase I: Mass/Lifetime Fitting Framework (Apr. 2010 - Sept. 2010)

The priority in this phase was the development of a simple framework, based on C, for a detailed study of the individual dimuon mass and decay length models.

My contributions in this phase can be summarized as

- Writing the framework
- Study of dimuon mass and various decay length model approaches, implementation into the RooFit package
- Extraction of the p_T dependence of the b-fraction (MC and data), comparison to previously published results
- First implementation of the polarization fit

Phase II: Sophisticated C++ Fitting Framework (Oct. 2010 - Jan. 2011)

The framework was extended to a more sophisticated framework, based on C++. The most significant changes were more flexibility in terms of controlling the individual contributions and a proper implementation of the acceptance and efficiency corrections. The corrections were applied directly to the PDF describing the $\cos\vartheta - \varphi$ distribution, in terms of dimuon variables. The fit was based on several steps. It was MC dependent (determination of FSR parameters, decay length resolution function, non-prompt decay length distribution, acceptance and efficiency determination).

My contributions in this phase can be summarized as

- Implementing plotting scripts
- Programming the toy-MC framework
- Study of convergence criteria of various MINUIT minimizing algorithms with toy-MC
- Study of systematic effects arising from the fitting framework with toy-MC
- Major contributions to the preparation of CMS Analysis Note AN-2011-087

Phase III: The Baseline Method (Feb. 2011 - Jul. 2011)

The C++ framework was completely rewritten in python. The most significant changes were the implementation of a simultaneous unbinned maximum likelihood fit in four ranges in dimuon mass and decay length phase space. The fit was divided in two steps, fixing the normalizations of the individual contributions in a first two-dimensional mass/decay length fit, followed by a two-dimensional polarization fit. The framework was MC dependent (acceptance and efficiency determination)

My contributions in this phase can be summarized as

- Writing basic code for preparation of TTrees (n-tuples of selected data sample)
- Adapting the toy-MC code for the new framework
- Conducting the toy-MC tests
- Writing the code to perform MC consistency tests
- Conducting the MC consistency tests

- Evaluation of systematic error due to unknown p_T distribution, altering the acceptance and efficiency maps
- Contributions to CMS Analysis Note AN-2011-091 and CMS Physics Analysis Summary PAS BPH-10-011
- Study of possible interpretations of CDF J/ψ polarization measurement
- Estimation of the discrimination power of a CMS measurement with toy-MC methods

Phase IV: The Optimized Method (Aug. 2011 - present)

The framework of the optimized method is based on the previous python framework. The most significant changes are the single muon efficiency correction approach and the determination of the efficiencies with the tag and probe method. The lifetime cut used in the previous framework is no longer necessary, nor the acceptance correction. The fit is a four-dimensional one-step fit, and is truly MC independent.

My contributions in this phase can be summarized as

- Rewriting the code for the preparation of TTrees
- Implementing the efficiency correction

Appendix D

Curriculum Vitae

Valentin Knünz
Kürnberggasse 1/5
A-1150 Wien

knuenz@cern.ch
+43 650 7674059
Date of Birth: 24.2.1985

Education

Sept. 1991 - Jun. 1995: Volksschule Altach
Sept. 1995 - Jun. 2003: Bundesrealgymnasium Schoren, Dornbirn
Oct. 2003 - Oct. 2004: Austrian civilian service (Zivildienst)
Oct. 2004 - Nov. 2011: **Technische Physik** (E810), Vienna University of Technology

Experience

Project Work at CERN (Jul. - Aug. 2008):

Study of Longitudinal painting schemes for H^- charge exchange injection into the PS2

Project Work at Atominstitut Vienna (Jun. - Jul. 2009):

Development of a method to measure the characteristic curve of a solar module

Project Work at HEPHY (Apr. - Jun. 2010):

CMS analysis - J/ψ mass and lifetime fits

Research for Diploma Thesis at HEPHY (Jul. 2010 - Sept. 2011):

Measurement of J/ψ Polarization with the CMS Experiment in Proton-Proton Collisions
at $\sqrt{s} = 7$ TeV

Contributions to Publications and Conferences

- sLHC project report, *Longitudinal painting schemes for H^- charge exchange injection into the PS2* (Jul. 2009, internal document)
- Talk at ÖPG, *Measurement of Quarkonium Production at CMS* (Sept. 2010, Salzburg)
- CMS Analysis Note, *Studies of the J/ψ polarization fit with a toy Monte Carlo program* (CMS AN-11-87, Feb. 2011, internal document)
- CMS Analysis Note, *Spin alignment of prompt and non-prompt J/ψ mesons in pp collisions at $\sqrt{s} = 7$ TeV* (CMS AN-11-91, Mar. 2011, internal document)
- Talk at Quarkonium Workshop, *J/ψ polarization scenarios from the Tevatron to the LHC* (Apr. 2011, Vienna)
- Poster at PLHC2011, *Measurement of J/ψ production at CMS* (Jun. 2011, Perugia)
- Physics Analysis Summary, *Polarization of prompt and non-prompt J/ψ mesons in pp collisions at $\sqrt{s} = 7$ TeV* (CMS PAS BPH-10-011, internal document)

Computer Skills

Mac OS, Windows, LaTeX, C++, Python, ROOT

Languages

Fluent in german and english

Appendix E

List of Abbreviations

ADD	Arkani-Hamed, Dimopoulos, Dvali
ALICE	A Large Ion Collider Experiment
AN	Analysis Note
ATLAS	A Toroidal LHC ApparatuS
BNL	Brookhaven National Laboratory
BPH	Beauty Physics
BSM	Beyond the Standard Model
CB	Crystal Ball
CDF	Collider Detector Fermilab
CEM	Color Evaporation Model
CERN	Organisation Européenne pour la Recherche Nucléaire
CMS	Compact Muon Solenoid
CMSSW	CMS Software
COM	Color Octet Model
CS	Collins-Soper
CSC	Cathode Strip Chamber
CSM	Color Singlet Model
DESY	Deutsches Elektronen Synchrotron
DT	Drift Tube
ECAL	Electromagnetic Calorimeter
FSR	Final State Radiation
GIM	Glashow–Iliopoulos–Maiani
GJ	Gottfried-Jackson
GUT	Grand Unified Theory
HCAL	Hadronic Calorimeter
HEPHY	Institute of High Energy Physics/Institut für Hochenergiephysik
HERA-B	Detector at Hadron Elektron Ring Anlage

HLT	High Level Trigger
HX	Helicity
L1	Level 1 Trigger
LEP	Large Electron Positron Collider
LHC	Large Hadron Collider
LHCb	LHC beauty
LO	Leading Order
LSB	Left Sideband
LSP	Lightest Supersymmetric Particle
MC	Monte Carlo
MCMC	Markov Chain Monte Carlo
mSUGRA	Minimal Supergravity Model
NLO	Next-to-Leading Order
NNLO	Next-to-Next-to-Leading Order
NPS	Non-Prompt Signal Region
NRQCD	Non-Relativistic QCD
ÖAW	Austrian Academy of Sciences/Österreichische Akademie der Wissenschaften
ÖPG	Österreichische Physikalische Gesellschaft
OZI	Okubo-Zweig-Iizuka
PAS	Physics Analysis Summary
PAT	Physics Analysis Toolkit
PLHC	Physics at the LHC (Conference)
POG	Physics Object Group
PRS	Prompt Signal Region
PS	Proton Synchrotron
PS2	Proton Synchrotron 2
QCD	Quantum Chromodynamics
QED	Quantum Electrodynamics
QGP	Quark Gluon Plasma
RHIC	Relativistic Heavy Ion Collider
RPC	Resistive Plate Chamber
RSB	Right Sideband
S/B	Signal over Background Ratio
SB	Sideband
SLAC	Stanford Linear Accelerator
sLHC	Super LHC
SM	Standard Model

SPS	Super Proton Synchrotron
SR	Signal Region
SUSY	Supersymmetry
TEC	Tracker Endcap
TIB	Tracker Inner Barrel
TID	Tracker Inner Disc
TOB	Tracker Outer Barrel
YM	Yang Mills

List of Figures

2.1	The CERN accelerator complex [2].	4
2.2	Schematic layout of the LHC [1].	5
2.3	(left) Typical diagrams for the most relevant Higgs boson production mechanisms at leading order: (a) gluon fusion, (b) vector boson fusion, (c) Higgs-strahlung, (d) Higgs bremsstrahlung off top quarks. (right) Higgs production cross sections at the LHC for the various production mechanisms as a function of the Higgs mass [4].	7
2.4	Branching ratios of the dominant decay modes of the SM Higgs particle (a) and total decay width (in GeV) of the SM Higgs boson as a function of its mass (b) [7].	7
3.1	A cut-away view of the CMS detector [3].	13
3.2	Schematic view of CMS, particles passing through subsystems of CMS [8].	14
3.3	Layout of one quarter of the CMS muon system as of 2011 [3].	15
3.4	Layout of the pixel detectors in the CMS tracker [3].	17
3.5	Layout of the inner tracking system [9].	18
3.6	Architecture of the L1 trigger at CMS [9].	19
3.7	Integrated luminosity, delivered by LHC and collected by CMS in 2010 [10] (a) and 2011 [11] (b).	21
4.1	(left) First observation of the J/ψ at BNL in p+Be collisions, measured in the dielectron mass spectrum [12]. (right) e^+e^- collisions at SLAC, cross section versus center of mass energy, with J/ψ going to (a) multi-hadron final states, (b) e^+e^- final states and (c) $\mu^+\mu^-$, $\pi^+\pi^-$ and K^+K^- final states [13].	24
4.2	Unsuppressed decay $\Phi \rightarrow K^+K^-$ (left) and OZI-suppressed $\Phi \rightarrow 3\pi$ decay (right), analogue for the decay $J/\psi \rightarrow 3\pi$ [16].	25
4.3	Charmonium spectrum and decays [14].	27
4.4	Bottomonium spectrum and decays [14].	27

4.5	Leading order diagram for CSM production of a 3S_1 quarkonium (a). Production of a 3S_1 quarkonium due to a fragmentation process (b) [15]. .	33
4.6	CSM LO and COM predictions for the differential cross section $d\sigma/dp_T$ at the Tevatron: Color singlet and color octet contributions to direct quarkonium production in $p\bar{p} \rightarrow Q + X$, compared to CDF results: (a) J/ψ , (b) ψ' , (c) χ_c and (d) $\Upsilon(1S)$ [18].	36
4.7	CSM predictions for differential cross section $d\sigma/dp_T$ for direct J/ψ production [19] (a) and direct $\Upsilon(1S)$ production [20] (b) with NLO and NNLO* contributions, compared to CDF data.	37
4.8	Global fits of NLO COM calculations to J/ψ data. Compared to three sets of results from different rapidity regions: (a) CDF, (b) CMS, (c) LHCb [21].	39
5.1	Leading order diagrams for vector quarkonium production in electron- positron annihilation (a) and for Drell-Yan production in quark-antiquark annihilation (b) [23].	42
5.2	Definition of the polarization frame in the quarkonium rest frame. The quantization axis z is chosen in the production plane, containing the momenta of the colliding beams, according to one of several possible conventions [23].	43
5.3	Definition of three reference frames (HX, GJ, CS) with respect to the momenta of the colliding beams (b1, b2) and the momentum of the quarkonium Q [23].	44
5.4	$J/\psi \rightarrow \ell^+ \ell^-$ decay: notations of axes, angles and angular momentum states [23].	45
5.5	Visualization of the angular decay distribution of transversely polarized (a) and longitudinally polarized J/ψ 's (b) [23].	47
5.6	Visualization of the angular decay distribution of transversely polarized (a) and longitudinally polarized J/ψ 's (b), measured in a frame rotated by 90° with respect to the frame where the polarization is naturally induced [23].	49
5.7	Kinematic dependence of the polarization parameters of J/ψ mesons with full transverse polarization in the CS frame ($\lambda_\psi^{CS} = +1$), as measured in the HX frame. The individual curves represent different rapidity intervals; starting from the solid line: $ y < 0.6$ (CDF), $ y < 0.9$ (ALICE), $ y <$ 1.8 (D0), $ y < 2.5$ (ATLAS and CMS), $2 < y < 5$ (LHCb) [25].	50
5.8	Allowed phase space regions for the polarization parameters due to positivity constraints [23, 26].	51

- 5.9 Effect of the χ_c feed-down contribution on the measurement of J/ψ polarization, when the directly produced J/ψ 's are fully transversely polarized. The observable prompt polarization is represented as a function of the total χ feed-down fraction $R(\chi)$, of the relative contribution of the two χ states and of the χ polarization states, $J_z(\chi_{c1})$ and $J_z(\chi_{c2})$. Red (and blue) curves: J/ψ 's from χ_{c1} dominate over J/ψ 's from χ_{c2} (and vice-versa). Magenta: the two contributions are equal [30]. 54
- 6.1 The J/ψ polarization parameter $\lambda(= \lambda_\vartheta)$ measured by E866 versus p_T and for two x_F ranges: $x_F < 0.45$ (solid circles) and $x_F > 0.45$ (open triangles). Systematic uncertainties are represented by the green band [31]. 58
- 6.2 p_T dependence of the J/ψ polarization parameters measured by HERA-B. CS, GJ and HX results are represented by the black circles, white squares and asterisks, respectively (both channels and both target datasets combined). Statistical and systematic errors are added in quadrature [32]. . . 59
- 6.3 Prompt J/ψ polarization measurements obtained by CDF in the years 2000 [33] (a) and 2007 [34] (b), and corresponding model calculations [33]. 60
- 6.4 Comparison of the prompt J/ψ polarization measurement of CDF (2007) to recent CSM NLO and NNLO* calculations [36, 19]. 61
- 6.5 The possible values of λ_ϑ^{CS} (green area) corresponding to the CDF measurement in the HX frame (blue points) [23]. 62
- 6.6 Kinematic dependence of $\lambda_\vartheta^{HX}, \lambda_\varphi^{HX}, \lambda_{\vartheta\varphi}^{HX}$ and $\tilde{\lambda}$ for the three scenarios discussed in the text, in the kinematic region of the CDF measurement ($|y| < 0.6$). 63
- 6.7 The E866 and HERA-B measurements in the CS frame and the CDF measurement in the HX frame, as a function of p_T (a). Reinterpretation of the measurements according to scenario 2 (b): the CDF measurement is translated to the CS frame and the three measurements are re-expressed as a function of p . A best-fit curve interpolates the data [37]. 64
- 6.8 Kinematic dependence of the prompt J/ψ polarization parameters $\lambda_\vartheta^{HX}, \lambda_\varphi^{HX}, \lambda_{\vartheta\varphi}^{HX}$ and $\tilde{\lambda}$ in the three scenarios discussed in the text, in the kinematic region accessible by the LHCb experiment ($3 < y < 3.5$). 66
- 6.9 Kinematic dependence of the prompt J/ψ polarization parameters $\lambda_\vartheta^{HX}, \lambda_\varphi^{HX}, \lambda_{\vartheta\varphi}^{HX}$ and $\tilde{\lambda}$ in the three scenarios discussed in the text, in a kinematic region accessible by the CMS experiment ($0.9 < |y| < 1.2$). Red markers indicate a possible CMS measurement with 40 pb^{-1} (arbitrary ordinate) and the respective statistical uncertainties, estimated with toy-MC experiments. . 67

- 6.10 Predictions for the three scenarios (colored markers) in the two-dimensional parameter spaces λ_φ^{HX} vs. $\lambda_{\vartheta\varphi}^{HX}$ ((a) (b)) and λ_φ^{HX} vs. $\tilde{\lambda}$ ((c) (d)) in the bins $10 < p_T < 15$ GeV ((a) (c)) and $20 < p_T < 30$ GeV ((b) (d)) and the expected statistical precisions of corresponding CMS measurements. The error ellipses (indicating the 1σ and 2σ contours) are arbitrarily placed on top of the predictions for scenario 2. 69
- 7.1 Event population of generated and reconstructed single muons (Fall10 MC sample) decaying from J/ψ 's. (a) p_T vs. η , (b) p vs. η of the tracker muon [39]. 78
- 7.2 Geometrical acceptance maps at midrapidity ($|y| < 0.9$) in the CS frame for (a) $8 < p_T < 10$ GeV, (b) $20 < p_T < 30$ GeV and in the HX frame for (c) $8 < p_T < 10$ GeV, (d) $20 < p_T < 30$ GeV. The values of the acceptance is indicated by the color code, changing linearly from 0% (violet) to 100% (red) [39]. 79
- 7.3 Reconstruction efficiency maps in the CS frame (a) and in the HX frame (b), trigger efficiency maps for the DoubleMu trigger in the CS frame (c) and in the HX frame (d). All maps for midrapidity ($|y| < 0.9$) in the cell $15 < p_T < 20$ GeV. The values of the efficiencies are indicated by the color code, changing linearly from 0% (violet) to 100% (red) [39]. 82
- 7.4 Example of a maximum likelihood estimation of an exponential decay PDF $E(t|\tau)$, based on a sample of 2 measurements $t_1 = 3$, $t_2 = 5$. The maximum likelihood estimator results in $\hat{\tau} = 4$ with an error estimate of $\sigma_{\hat{\tau}} \sim 2.83$. (a) shows the resulting PDF, (b) shows the likelihood function and the NLL function (scaled by factor 10^{-3}). 85
- 7.5 Examples of the distribution of data in the dimuon mass variable $m_{\mu\mu}$ together with the fit results, visualizing the individual components, in the bins $|y| < 0.9$, $20 < p_T < 30$ GeV (a) and $0.9 < |y| < 1.2$, $10 < p_T < 15$ GeV (b) [39]. 88
- 7.6 Examples of the distribution of data in the decay length variable $l_{J/\psi}$ together with the fit results, in the mass signal region ((a) (b)) and in the mass sidebands ((c) (d)) in the bins $|y| < 0.9$, $20 < p_T < 30$ GeV ((a) (c)) and $0.9 < |y| < 1.2$, $10 < p_T < 15$ GeV ((b) (d)) [39]. 90

- 7.7 (a) B-fraction measurement, as a by-product of the polarization measurement, compared to results of the b-fraction measurement of CDF [39]. (b) ATLAS measurement of the b-fraction at midrapidity, compared to CMS (differential cross section analysis) and CDF results [46]. The yellow band represents the spin alignment envelope, the systematic error arising from the unknown polarization of prompt and non-prompt J/ψ 's. 92
- 7.8 Examples of the distribution of data in $\cos\vartheta$ and φ together with the fit results in the CS frame ((a) (b)), and in the HX frame ((c) (d)), in the prompt J/ψ enriched (cut on $l_{J/\psi} < 0.1$ mm) mass signal region, showing the individual components (violet dashed: background, red dashed: non-prompt, blue dashed: prompt, blue solid: composite PDF) in the bin $|y| < 0.9$, $20 < p_T < 30$ GeV [39]. 94
- 7.9 Schematic visualization of the four regions defined for the two-dimensional mass/decay length fit [39]. 95
- 7.10 MC estimated value of $l_{J/\psi}^{99}$ vs. p_T for three rapidity regions (green: $|y| < 0.9$, blue: $0.9 < |y| < 1.2$, red: $1.2 < |y| < 1.6$). 96
- 7.11 Estimated fractions of prompt, non-prompt and background components in the non-prompt signal region with $l_{J/\psi} > 0.1$ mm (a) and in the prompt signal region with $l_{J/\psi} < 0.1$ mm (b) in the bin $0.9 < |y| < 1.2$ vs. p_T . The total number of events in the respective region is shown on the top [39]. 97
- 8.1 Toy-MC study of λ_{ϑ}^{HX} in the polar asymmetry scenario in bin $0.9 < |y| < 1.2$, $20 < p_T < 30$ GeV. Parameter distributions: (a) $\lambda_{\vartheta}^{HX^{PR}}$, (b) $\lambda_{\vartheta}^{HX^{NP}}$. Distribution of the standard scores: (c) $z(\lambda_{\vartheta}^{HX^{PR}})$, (d) $z(\lambda_{\vartheta}^{HX^{NP}})$. All distributions are compared to the expected mean (red line). The ordinate represents the number of toys returning values in the respective bins. . . . 101
- 8.2 Examples of the distribution of unpolarized pseudo-data in $\cos\vartheta$ and φ in the prompt signal region in the bin $0.9 < |y| < 1.2$, $20 < p_T < 30$ GeV. The dotted red and the dotted blue lines correspond to the fitted contributions from non-prompt and prompt J/ψ 's, respectively. The solid blue line corresponds to the sum of the two contributions. (a) $\cos\vartheta$ in the CS frame, (b) φ in the CS frame, (c) $\cos\vartheta$ in the HX frame, (d) φ in the HX frame. 103

- 8.3 Negative-log-likelihood contours in arbitrary units, visualized in the vicinity of the found minimum, from one single fit of the toy-MC study of the unpolarized scenario in the bin $0.9 < |y| < 1.2$, $20 < p_T < 30$ GeV. (a) $\lambda_\vartheta^{CS^{PR}}$ vs. $\tilde{\lambda}^{CS^{PR}}$, (b) $\lambda_\vartheta^{CS^{PR}}$ vs. $\lambda_\vartheta^{CS^{NP}}$, (c) $\lambda_\vartheta^{HX^{PR}}$ vs. $\tilde{\lambda}^{HX^{PR}}$, (d) $\lambda_\vartheta^{HX^{PR}}$ vs. $\lambda_\vartheta^{HX^{NP}}$. The remaining four parameters are set constant to the estimated values at the minimum. 104
- 8.4 Results of the MC consistency tests - λ_ϑ^{HX} vs. p_T for the prompt reconstruction level test (a), the prompt trigger level test (b), the non-prompt reconstruction level test (c) and the non-prompt trigger level test (d). The green lines indicate the generated polarization of the samples. . . 106
- 8.5 Distribution of the (a) prompt and (b) non-prompt Fall10 MC sample in $\cos\vartheta$ and φ in the HX frame together with the fit results of the MC consistency test in the bin $0.9 < |y| < 1.2$, $15 < p_T < 20$ GeV. The green lines represent the unpolarized model, the blue lines correspond to the fit results. (a) shows the prompt trigger level test, (b) shows the non-prompt reconstruction level test. 107
- 8.6 (a) p_T distributions obtained by parametrizing ATLAS, PYTHIA and CASCADE distributions of the prompt component. (b) Prompt and non-prompt p_T distributions obtained from ATLAS results [39]. 110
- 8.7 Distributions of data in the left mass sideband on the variables (a) $\cos\vartheta$ in the CS frame, (a) $\cos\vartheta$ in the HX frame, (a) φ in the CS frame, (a) φ in the HX frame in the bin $0.9 < |y| < 1.2$, $10 < p_T < 15$ GeV. The lines shown in the $\cos\vartheta$ projections correspond to $\lambda_\vartheta = +1$ (dashed), 0 (solid) and -1 (dotted) and $\lambda_\varphi = \lambda_{\vartheta\varphi} = 0$. The lines shown in the φ projections correspond to scenarios with $\lambda_\varphi = +0.5$ (dashed), 0 (solid) and -0.5 (dotted) and $\lambda_\vartheta = \lambda_{\vartheta\varphi} = 0$ [39]. 111
- 9.1 Example of a tag and probe fit for the evaluation of the L1/L2 trigger efficiency corresponding to $\epsilon_{L1L2} = 0.92 \pm 0.01$. The dimuon mass distribution of the tag and probe muons is shown for (a) all probes, (b) the passing probes and (c) the failing probes [51]. 116
- 9.2 Sets of loose fiducial cuts (indicated by the red line) defined for the HLT muon (a) and the tracker muon (b), based on the Fall10 MC reconstruction efficiency. Sets of tight fiducial cuts defined for the HLT muon (c) and the tracker muon (d). 118

List of Tables

3.1	Main parameters of the CMS solenoid [3].	14
4.1	Properties of the quarkonium meson family [14].	26
6.1	Statistical uncertainties, $\sigma(\lambda_i)$, of the polarization parameters λ_i in the HX frame, estimated in toy-MC experiments (unpolarized scenario). . . .	68
7.1	Run periods, corresponding low p_T trigger paths, and the collected integrated luminosity [39].	76
7.2	Single muon quality cuts used in the J/ψ polarization analysis [39].	77
7.3	Approximate J/ψ event yields in the considered kinematic cells in thousands of events, triggered by the DoubleMu trigger and surviving all cuts [39].	80
7.4	Background fraction (in %) under the J/ψ peak, in a mass window of $\pm 2\sigma_m$ about the pole mass. Estimated from the DoubleMu trigger sample in the considered kinematic cells [39].	89
8.1	Polarization scenarios tested with the toy-MC method.	102
8.2	Mean of the distribution of the standard score $z(\lambda_i)$ for the unpolarized toy-MC study.	105
8.3	R.m.s. of the distribution of the standard score $z(\lambda_i)$ for the unpolarized toy-MC study.	105

Bibliography

- [1] L. Evans and P. Bryant. LHC Machine. *J. Instrum.*, 3:S08001, 2008.
- [2] LHC the guide. *CERN Brochure*, 2009.
- [3] The CMS Collaboration. *CMS Physics Technical Design Report Volume I: Detector Performance and Software*. CERN, 2006.
- [4] The CMS Collaboration. CMS Physics Technical Design Report, Volume II: Physics Performance. *J. Phys. G: Nucl. Part. Phys.*, 34:995–1579, 2007.
- [5] The CDF and D0 Collaborations. Combined CDF and D0 Upper Limits on Standard Model Higgs Boson Production with up to 8.2 fb^{-1} of Data. *FERMILAB-CONF-11-044-E CDF Note 10441 D0 Note 6184*, 2011.
- [6] The CMS Collaboration. Search for standard model Higgs boson in pp collisions at $\sqrt{s} = 7 \text{ TeV}$ and integrated luminosity up to 1.7 fb^{-1} . *CMS PAS HIG-11-022*, 2011.
- [7] M. Spira, P. M. Zerwas. Electroweak Symmetry Breaking and Higgs Physics. *Lect. Notes Phys.*, 512:161–225, 1998.
- [8] <http://cms.web.cern.ch/cms/Detector/FullDetector/index.html>. (July 20, 2011).
- [9] The CMS Collaboration. The CMS experiment at the LHC. *J. Instrum.*, 3:S08004, 2008.
- [10] <https://twiki.cern.ch/twiki/bin/view/CMSPublic/LumiPublicResults2010>. (September 22, 2011).
- [11] <https://twiki.cern.ch/twiki/bin/view/CMSPublic/LumiPublicResults>. (September 22, 2011).
- [12] J. J. Aubert et al. Experimental Observation of a Heavy Particle *J. Phys. Rev. Lett.*, 33:1404, 1974.

- [13] J. -E. Augustin et al. Discovery of a Narrow Resonance in e^+e^- Annihilation. *Phys. Rev. Lett.*, 33:1406, 1974.
- [14] K. Nakamura et al. (Particle Data Group). *J. Phys. G*, 37:075021, 2010.
- [15] Darren David Price. *Studies of quarkonium production and polarisation with early data at ATLAS*. PhD thesis, Lancaster University, 2008.
- [16] David J. Griffiths. *Introduction to elementary particles*. 1987.
- [17] N. Brambilla et al. (QWG Collaboration). Heavy Quarkonium Physics. *CERN Yellow Report 2005-005*, *arXiv:0412158[hep-ph]*.
- [18] Michael Krämer. Quarkonium Production at High-Energy Colliders. *Prog. Part. Nucl. Phys.*, 47:141–201, 2001.
- [19] J.P. Lansberg. J/ψ production at $\sqrt{s} = 1.96$ and 7 TeV: Color-Singlet Model, NNLO* and polarisation. *arXiv:1107.0292v1[hep-ph]*, 2011.
- [20] P. Artoisenet, J. Campbell, J.P. Lansberg, F. Maltoni, F. Tramontano. Upsilon production at the Tevatron and the LHC. *Phys. Rev. Lett.*, 101:152001, 2008.
- [21] Mathias Butenschoen, Bernd A. Kniehl. World data of J/ψ production consolidate NRQCD factorization at NLO. *arXiv:1105.0820v1[hep-ph]*, 2011.
- [22] Z. Conesa del Valle et al. Quarkonium production in high energy proton-proton and proton-nucleus collisions. *Nuclear Physics B (Proceedings Supplements)*, 214:3–36, 2011.
- [23] P. Faccioli, C. Lourenço, J. Seixas, H. Wöhri. Towards the experimental clarification of quarkonium polarization. *Eur. Phys. J. C*, 69:657, 2010.
- [24] E. Braaten, T.C. Yuan. Gluon Fragmentation into Heavy Quarkonium. *Phys. Rev. Lett.*, 71:1673, 1993.
- [25] N. Brambilla et al. (QWG Collaboration). Heavy quarkonium: progress, puzzles, and opportunities. *Eur. Phys. J C*, 71:1534, 2011.
- [26] P. Faccioli, C. Lourenço, J. Seixas, H. Wöhri. Model-independent constraints on the shape parameters of dilepton angular distributions. *Phys. Rev. D*, 83:056008, 2011.
- [27] P. Faccioli, C. Lourenço, J. Seixas. Rotation-invariant relations in vector meson decays into fermion pairs. *arXiv:1005.2601v1[hep-ph]*, 2010.

- [28] P. Faccioli, C. Lourenço, J. Seixas, H. Wöhri. Study of ψ' and χ_c decays as feed-down sources of J/ψ hadro-production. *JHEP*, 0810:004, 2008.
- [29] P. Faccioli, C. Lourenço, J. Seixas, H. Wöhri. Determination of χ_c and χ_b polarizations from dilepton angular distributions in radiative decays. *Phys. Rev. D*, 83:096001, 2011.
- [30] P. Faccioli. Feed-down decays and quarkonium polarization. *Workshop Quarkonium production: Probing QCD at the LHC, Vienna*, 2011.
- [31] FNAL E866/NuSea Collaboration. J/ψ Polarization in 800-GeV p-Cu Interactions. *Phys. Rev. Lett.*, 91:211801, 2003.
- [32] The HERA-B Collaboration. Angular distributions of leptons from J/ψ 's produced in 920 GeV fixed-target proton-nucleus collisions. *Eur. Phys. J. C*, 60:517–524, 2009.
- [33] The CDF Collaboration. Measurement of J/ψ and $\psi(2S)$ polarization in $p\bar{p}$ collisions at $\sqrt{s} = 1.8$ TeV. *Phys. Rev. Lett.*, 85:2886–2891, 2000.
- [34] The CDF Collaboration. Polarizations of J/ψ and $\psi(2S)$ Mesons Produced in $p\bar{p}$ Collisions at $\sqrt{s} = 1.96$ TeV. *Phys. Rev. Lett.*, 99:132001, 2007.
- [35] S. P. Baranov. Highlights from the k_T -factorization approach on the quarkonium production puzzles. *Phys. Rev. D*, 66:114003, 2002.
- [36] Private Communication from Jean-Philippe Lansberg.
- [37] P. Faccioli, C. Lourenço, J. Seixas, H. Wöhri. J/ψ polarization from fixed-target to collider energies. *Phys. Rev. Lett.*, 102:151802, 2009.
- [38] <https://twiki.cern.ch/twiki/bin/view/CMSPublic/WorkBookMuonAnalysis>. (July 22, 2011).
- [39] C. Lourenço et al. Spin alignment of prompt and non-prompt J/ψ mesons in pp collisions at $\sqrt{s} = 7$ TeV. *CMS AN-11-091 (Internal Note, Unpublished)*, 2011.
- [40] <https://espace.cern.ch/cms-quarkonia/onia-polarization/default.aspx>. (August 6, 2011).
- [41] <https://twiki.cern.ch/twiki/bin/view/CMSPublic/SWGuidePAT>. (July 23, 2011).
- [42] R. Frühwirth. University Lecture: Statistik. 2010.

- [43] F. James and M. Winkler. *MINUIT User's Guide*. CERN, Geneva, 2004.
<http://seal.web.cern.ch/seal/documents/minuit/mnusersguide.pdf>.
- [44] W. Verkerke and D. Kirkby. *RooFit Users Manual v2.07*, 2006.
http://roofit.sourceforge.net/docs/RooFit_Users_Manual_2.07-29.pdf.
- [45] The CMS Collaboration. Prompt and non-prompt J/ψ production in pp collisions at $\sqrt{s} = 7$ TeV. *Eur. Phys. J. C*, 71:1575, 2011.
- [46] The ATLAS Collaboration. Measurement of the differential cross-sections of inclusive, prompt and non-prompt J/ψ production in proton-proton collisions at $\sqrt{s} = 7$ TeV. *Nucl. Phys. B*, 850:387–444, 2011.
- [47] The CDF Collaboration. Measurement of the J/ψ Meson and b-Hadron Production Cross Sections in $p\bar{p}$ Collisions at $\sqrt{s} = 1960$ GeV. *Phys. Rev. D*, 71:032001, 2005.
- [48] Private Communication from Rudolf Frühwirth.
- [49] Private Communication from Roberto Covarelli.
- [50] <https://twiki.cern.ch/twiki/bin/viewauth/CMS/TagAndProbe>. (July 23, 2011).
- [51] Private Communication from Ilse Krätschmer.